# Exploration of the Equilibrium Operating Space for NSTX-Upgrade

S.P. Gerhardt, R. Andre, and J.E. Menard
*Princeton Plasma Physics Laboratory, Princeton, NJ 08543*

This paper explores a range of high-performance equilibrium scenarios available in the NSTX-Upgrade device [J.E. Menard, submitted for publication to Nuclear Fusion]. NSTX-Upgrade is a substantial upgrade to the existing NSTX device [M. Ono, et al., Nuclear Fusion **40**, 557 (2000)], with a significantly higher toroidal field and solenoid capabilities, and three additional neutral beam sources with significantly larger injection tangency radii. Equilibria are computed with free-boundary TRANSP, allowing a self consistent calculation of the non-inductive current drive sources, the plasma equilibrium, and poloidal field coil current, using the realistic device geometry. The thermal profiles are taken from a variety of existing NSTX discharges, and different assumptions for the thermal confinement scalings are utilized. The no-wall and ideal-wall n=1 stability limits are then computed with the DCON code. The central safety factor is quite sensitive to many parameters: it generally increases with large outer plasma-wall gaps and higher density, but can have either trend with the confinement enhancement factor. In scenarios with strong central beam current drive, the inclusion of non-classical fast ion diffusion raises $q_{min}$, decreases the pressure peaking, and generally improves the global stability, at the expense of a reduction in non-inductive fraction; cases with less beam current drive are largely insensitive to additional fast ion diffusion. The non-inductive current level is quite sensitive to the underlying confinement and profile assumptions. For instance, for $B_T$=1.0 T and $P_{inj}$=12.6 MW, the non-inductive current level varies from 875 kA with ITER-98 thermal confinement scaling and narrow thermal profiles to 1325 kA for an ST specific scaling expression and broad profiles. This sensitivity should facilitate the determination of the correct scaling of transport with current and field to use for future fully non-inductive ST devices. Scenarios are presented which can be sustained for 8-10 seconds, or ~$20\tau_{CR}$, at $\beta_N$=3.8-4.5, facilitating, for instance, the study of disruption avoidance for very long pulse. Scenarios have been documented which can operate with $\beta_T$~25% and equilibrated $q_{min}$>1. The value of $q_{min}$ can be controlled at either fixed non-inductive fraction of 100% or fixed plasma current, by varying which beam sources are used, opening the possibility for feedback $q_{min}$ control. In terms of quantities like collisionality, neutron emission, non-inductive fraction, or stored energy, these scenarios represent a significant performance extension compared to NSTX and other present spherical torii.

PACS: 52.55.Fa, 52.55.Wq

Keywords: Spherical Torus, NSTX, NSTX-Upgrade

E-mail contact of corresponding author: sgerhard@pppl.gov
Address: Princeton Plasma Physics Lab
PO Box 451
Princeton, NJ 08543

# Exploration of the Equilibrium Operating Space for NSTX-Upgrade

S.P. Gerhardt, R. Andre, and J.E. Menard
*Princeton Plasma Physics Laboratory, Princeton, NJ 08543*

Sections



34 Figures
6 Tables in body of text + 5 in appendix
134 References

PACS: 52.55.Fa, 52.55.Wq

Keywords: Spherical Torus, NSTX, NSTX-Upgrade

E-mail contact of corresponding author: sgerhard@pppl.gov
Address: Princeton Plasma Physics Lab
PO Box 451
Princeton, NJ 08543

## 1: Introduction and motivation

The spherical torus [Peng 1986] is a leading candidate for the plasma core of facilities designed to study plasma material interactions [Goldston 2008], nuclear component testing [Abdou 1996, Peng 2005, Wilson 2004b, Voss 2008, Peng 2008, Peng 2009, Stambaugh 2010], or to generate fusion power [Stambaugh 1997, Akers 2000, Najmabadi 2003, Wilson 2004a, Menard 2011]. This interest is driven by the compact nature of the ST device and associated excellent utilization of the toroidal field, the natural elongation of the plasma cross-section [Roberto 1992], the high neutron wall loading, the significantly higher $\beta$ values [Miller 1997, Menard 1997], and potential ease of maintenance [Goldston 2008, Peng 2005, Peng 2008].

However, in order to connect the database of results from present 1-MA class STs, such as NSTX [Ono 2000] or MAST [Sykes 2001], to the scenario requirements for machine targeting those next step missions, better physics understanding is required in many areas. Among the most critical of these issues are the scaling of the electron transport with field and current [Kaye 2006, Kaye 2007a, Kaye 2007b, Valovic 2009], the physics of fast-particles in the lower field of the ST [Gorelenkov 2004, Fredrickson 2004, Fredrickson 2006a, Fredrickson 2006b, Podesta 2009, Fredrickson 2009] and the ability to non-inductively sustain the high-beta ST configuration (see Refs. [Menard 2006, Gates 2006a, Menard 2007, Gates 2007, Gates 2009, Menard 2010, Gerhardt 2011, Gerhardt 2010] for progress towards this goal in NSTX).

The NSTX-Upgrade facility [Menard 2012] has been designed to address these and other critical issues. There are two primary components to this upgrade of the existing NSTX device. The first is a complete replacement of the “center stack”, which contains the inner-leg of the TF coils, the OH solenoid, and some divertor coils. This allows an increase of the toroidal field capability from 0.55 T to 1.0 T, with significantly longer pulse capability. The available solenoid flux is increased by a factor of 2.8. The second upgrade is the addition of a second neutral beam injector with more tangential injection. This provides more auxiliary heating power, and equally importantly, additional neutral beam current drive.

Of course, the scenarios cannot for NSTX-Upgrade cannot be fully defined in advance, because the physics knowledge required to define those scenarios is incomplete; this uncertainty is among the primary motivations of the Upgrade project. The present study will scan important quantities which have some uncertainty (global confinement, anomalous fast ion diffusivity, profile shapes), in order to quantify the effects of various assumptions. This will in turn identify scenarios where small variations in these qualities will have a large impact, and thus facilitate important physics studies.

The organization of the remainder of this paper is as follows. Section 2 provides a brief summary of the facility modifications associated with the NSTX-Upgrade project. Section 3 describes the numerical tools used in this study. Section 4 illustrates a comparison of the free-boundary equilibrium solver in TRANSP to actual NSTX data.

Section 5 describes the effect of some important parameters on the performance of NSTX-Upgrade plasma; variations in the outer plasma-wall gap, global thermal confinement, plasma density, anomalous fast ion diffusivity, and ion thermal diffusivity & Zeff (both at fixed global confinement) are all considered. Section 6 describes five different scenario optimizations:

- Section 6.1 studies 100% non-inductive scenarios optimized at high-injected power and high plasma current.
- Section 6.2 addresses partial inductive configurations with high current, field, and heating power.
- Section 6.3 describes lower power scenarios at somewhat reduced toroidal field strength ($B_T$=0.75 T) and plasma current, which are in principal sustainable for 8-10 seconds.
- Section 6.4 addresses configurations designed to maximize the *sustainable* toroidal $\beta$.
- Section 6.5 describes the ability to control the current profile using various combinations of four of the available heating neutral beam sources.

Section 7 provides a comparison between the parameters already achieved in NSTX and the projected parameters of NSTX-Upgrade. A summary and discussion is provided in Sect. 8.

## 2: The NSTX-Upgrade Facility

As noted above, NSTX-U represents a major expansion of the physics capacities of the facility. An comprehensive overview of the NSTX-Upgrade physics motivation and engineering design is given in Ref. [Menard 2012]. This section describes briefly those upgrades relevant to the present study.

The first major component of the upgrade is a new center column with upgraded TF and OH coils. The TF upgrade is reflected in two figures of merit. First, the maximum field that can be created at the plasma mid-radius is increased from 0.55 T to 1.0 T. Second, the $\int I_{TF}^2 dt$ limit, which is indicative of coil heating limits, is increased by a factor of 20 (from $6\times10^9$ $A^2s$ to $1.2\times10^{11}$ $A^2s$). Hence, both higher fields and longer pulses will be available. The OH coil also has significant new capability, with the $\int I_{TF}^2 dt$ limits increased by a factor of 3.5 (from $2.5\times10^8$ $A^2s$ to $8.5\times10^8$ $A^2s$), and the flux available for driving inductive current increased from 0.75 Wb to 2.1 Wb.

These enhanced capabilities come from both improved design and a larger radius for the center column. In particular, the inboard PFC boundary is increased from R=18.5 cm in NSTX to R=31.5 cm in NSTX-Upgrade. As a consequence, typical aspect ratios for NSTX-Upgrade scenarios are 1.65<A<1.8, compared to 1.35<A<1.6 for NSTX. Structural improvements required for safe operations at these higher fields and currents are described in Ref. [Menard 2012].

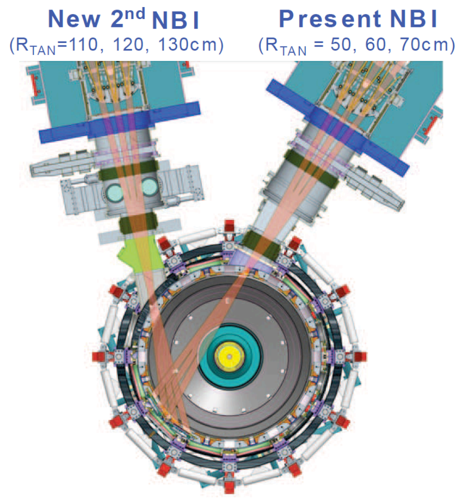


*Fig. 1: Illustration of the present neutral beam injector utilized in NSTX, and the 2nd neutral beam injector that is a primary component of the NSTX-Upgrade project.*

As illustrated in Fig. 1, the second major component of the Upgrade is the addition of a second neutral beamline, complementing the existing NSTX heating systems [Stevenson 2002] with three additional beam sources. As will be discussed in great detail throughout this paper, this upgrade is not only designed to increase the available heating power. These new beamline is steered to have a significantly larger beam tangency radius, which improves the current drive efficiency and provides the option for off-axis NBCD [Gerhardt 2011, Menard 2012].

The NSTX neutral beams are a reuse of the system originally designed and implemented on TFTR [Grisham 1987, Grisham 1994, Grisham 1995]. Each beamline has three sources assembled horizontally in a fan array, with the crossing-point of the three beams at approximately the point where they enter the vessel. Both the new and old beamlines inject horizontally at the vessel midplane. The original NSTX beamline has tangency radii of $R_{tan}$=50,60, and 70 cm; the new beamline has tangency radii of 110, 120 & 130 cm. As described in Ref. [Menard 2012], the outermost beam, with $R_{tan}$=130 cm, provides substantial off-axis current drive.

An important determinant of the scenario parameters are the power and pulse duration achievable for a given neutral beam acceleration voltage. These are given in figure 2. A higher beam voltage will clearly provide more power and provide better beam penetration to the plasma core. However, the allowable pulse duration, limited by heating on the primary energy ion dump, decreases rapidly as the voltage is increased. The scenarios in this paper will most commonly utilize 90 kV sources, which produce 2.1 MW for up to 3 seconds; this duration allows the current profile to fully equilibrate. Lower beam voltages (80 kV and 65 kV) will be used for scenarios where longer pulse is desired, and higher beam voltages will be used for scenarios that desire additional power and current drive, at the expense of pulse length.

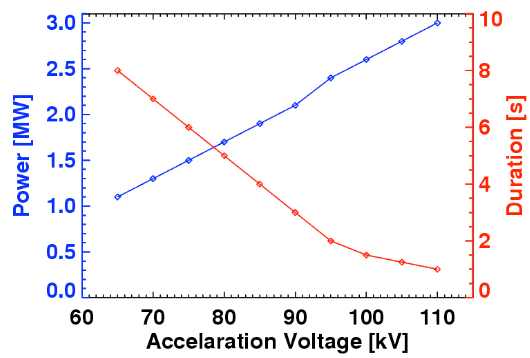


*Fig. 2: Power and allowable pulse duration for the NSTX neutral beam sources, as a function of the acceleration voltage.*

## 3: Computation techniques.

### *3.1 Free-Boundary TRANSP Simulations*

The primary computation tool utilized in this study is the recently available free-boundary capability in the TRANSP code [Hawryluk 1980]. The inputs to these simulations are time histories of the requested plasma boundary shapes and plasma current level, kinetic profiles mapped to the minor radius (square-root of toroidal flux), and the power, voltage, and geometry of the neutral beam injection.

These inputs are used to compute the bootstrap current [Bickerton 1971, Galeev 1971, Zarnstorff 1984, Peeters 2000] using the Sauter model [Sauter 1999]. The neutral beam current drive [Ohkawa 1970, Fisch 1987, Lin-Liu 1997] is computed by the NUBEAM code [Pankin 2004]; 8000 particles were typically used in these simulations. The beam-current shielding factor derived by Lin-Liu & Hinton [Lin-Liu 1997] is used. The plasma current is fixed to match the requested level. The poloidal-field diffusion equation [Zarnstorff 1990] is solved to relax the current profile; we allow this calculation to run for at least four seconds with no other changes to the equilibrium, so that the fully relaxed state can be studied. It is possible that the total of the non-inductive currents are greater than the total requested current, and these cases will be indicated as non-inductive fractions greater than 100%. These cases will have negative inductive currents and negative surface voltages, so that the total current level is matched to the request. Note that there is no effort to model the ramp-up in this case, and the equilibria presented here represent "snap-shots" of the fully relaxed state.

The free-boundary capability utilized in this study comes from the recent inclusion of the ISOLVER equilibrium code within TRANSP. The desired plasma boundaries in this study were generated with the stand-alone free-boundary equilibrium ISOLVER code, utilizing the coil set of NSTX-Upgrade. These plasma boundaries were then given to TRANSP as the "target" boundaries for the free-boundary simulations. The code then computes the coil currents that give the best match in a least squares sense between the computed boundary and X-point locations and the target, given the current and pressure profiles. There are no vessel eddy currents in the calculation.

### *3.2 Confinement and profile assumptions.*

A first principle integrated simulation of these scenarios would involve a validated model for the ion and electron thermal transport in both the plasma core and edge pedestal. With regard to ions, there is significant evidence that neoclassical theory describes the heat transport reasonably well [Kaye 2007a, Kaye 2007b]. Models for the electron transport are not as well established.

For the plasma core, the dependence of the core $\chi_e$ on the plasma current profile would be a key component of such a model [Luce 2011, Ferron 2011]. Models such as GLF23 [Waltz 1997] or, more recently, TGLF [Kinsey 2008] have been used for this purpose in modeling the core electron transport at conventional aspect ratio [Murakami 2005, Voitsekovich 2009, Kinsey 2011]. The electron temperature gradient (ETG) [Smith 2009a, Smith 2009b, Ren 2011] and/or microtearing modes [Wong 2007, Wong 2008, Guttenfelder 2011] that have been suggested as the source of electron transport in the ST are in principle included in the transport model formulation noted above. However, these models have not been successfully validated against ST profiles. Furthermore, it has also been suggested that fast-particle driven MHD instabilities could contribute to the observed electron transport [Stutman 2009]. This transport mechanism would not be included in turbulence-based reduced transport models noted above.

It would also be desirable to have a first-principle model for the height of the H-mode pedestal, which sets the boundary condition for the core physics modeling. At conventional aspect ratio, models such as EPED1 [Snyder 2009] are being developed to predict the pedestal height. This model utilizes a combination of peeling-ballooning stability and transport driven by kinetic ballooning modes to determine the pedestal structure. However, the applicability of this model to the ST is not yet established. There is evidence that peeling-ballooning physics plays an important role in determining the edge stability [Maingi 2009, Sontag 2010, Boyle 2011, Diallo 2011], but the kinetic ballooning model for transport has not be verified. Further, the detailed experiment/theory comparisons of pedestal structure have not been completed as at conventional aspect ratio. Hence, for the reasons stated in this and the previous paragraph, first principle calculations of the electron temperature profile shape and magnitude are not at the moment possible.

A similar situation exists with respect to the density profile. In this case, neither the external fuelling and impurity sources such as gas puffing, nor the particle and impurity transport, are sufficiently well understood and quantified for inclusion in these integrated models.

For these reasons we have decided to use experimental profiles for the electron temperature and density shapes in these simulations, while simulating the ion thermal transport using neoclassical theory. In particular, the experimental electron density profile is scaled to achieve a desired Greenwald fraction $f_{GW} = \dfrac{\overline{n}_e}{I_P/\pi a^2}$ [Greenwald 2002]. The ion thermal transport is predicted by the Chang-Hinton formulation [Chang 1982]. The electron temperature profile shape is taken from experimental data, and scaled such that a given global confinement is achieved. The ion density is calculated assuming a flat $Z_{eff}$ profile, with Carbon being the only impurity (the baseline plasma facing (PFC) component material for NSTX-U is graphite). The value of $Z_{eff}$ is 2 unless stated otherwise.

Two different assumptions for the global confinement are utilized in this modeling. The first is the standard $H_{98}$ scaling expression [ITER 1998], given by

$$\tau_{98} \propto I_P^{0.93} B_T^{0.15} \overline{n}_e^{0.41} P_{Loss}^{-0.69} R_0^{1.97} \varepsilon^{0.58} \kappa^{0.78}. \tag{1a}$$

The second scaling assumption is a spherical torus expression [Kaye 2006], given by

$$\tau_{ST} \propto I_P^{0.57} B_T^{1.08} \overline{n}_e^{0.44} P_{Loss}^{-0.73} \tag{1b}$$

The primary difference between these expressions is the scaling with toroidal field and plasma current, and this will have implications for the scenarios described below. For instance, the optimization to highest non-inductive fraction utilizes the highest toroidal field possible at less than maximum plasma current; in these cases, the ST scaling law predicts a more favorable result. On the other hand, the optimization to high toroidal $\beta$ utilizes higher plasma current but lower toroidal field strength; the ITER-98 scaling law is more favorable in this case.

Secondly, the simulations have been run with different $n_e$ and $T_e$ profile shapes, from 5 different discharges taken in NSTX. Many cases utilize the profiles from the high aspect ratio discharge 142301 [Gerhard 2011b]; these profiles generally produce the best performance. Also tested are profiles from a very high $\beta_P$ discharge (133964) and a high $\beta_T$ discharge 135129 [Gerhardt 2011b]. These three discharges were made with active lithium conditioning of the plasma facing components [Kugel 2008, Bell 2010]. Hence, we also consider a very long pulse (116313) [Menard 2006, Menard 2007] and a high-current (121123) discharge made before the advent of lithium conditioning. These comparisons will be made in Sections 6.1 and 6.4. Overall, more that 9000 separate fully-relaxed equilibria were generated over the course of these studies.

### *3.3: Global stability calculations.*

We have evaluated some of these NSTX-U scenarios for their global ideal n=1 stability, both with and without an ideally conducting wall. In these cases, the equilibria generated by TRANSP are given to the fixed-boundary equilibrium code CHEASE [Lutgens 1996], which refines the equilibrium in preparation for the stability calculation. The inverse-equilibria generated by CHEASE is then given to the DCON code [Glasser 1997]. DCON computes a stability metric $\delta W$ for external modes that is positive for a stable configuration and negative for unstable configurations; the magnitude of the parameter can be taken as an indicator of proximity to the stability boundary. The calculation of $\delta W$ can be done without a nearby conducting wall, or with an ideally conducting wall at the approximate location of the stabilizing passive plates. DCON also provides a binary answer regarding the stability of internal modes.

## 4: Comparison of the free boundary solver results to experimental equilibrium.

Before considering simulations of NSTX-Upgrade, it is useful to test the free-boundary solver against actual NSTX equilibria. This exercise has been completed for a variety of NSTX discharges. The results of such a test are presented in this section.

In these studies, the time evolution of the plasma boundary, q-profile, thermal profiles, and neutral beam heating sources are provided as input to the code. The equilibrium solver in TRANSP then uses the given q-profile, pressure profile computed as the summed experimental thermal pressure and computed fast ion pressure, and target plasma boundary shape as inputs. The outputs of such an equilibrium calculation are the computed plasma boundary that best matches the target boundary and X-point locations in a least-squares sense, and the coil currents determined by the code. The plasma boundary and coil currents so computed by TRANSP can then be compared to the reconstructed experimental plasma boundary (the target boundary) and the actual coil currents. Note that the coil currents are determined at each time step independent of previous time step, resulting in some jitter in the computed currents that is not present in a real coil with finite inductance.

An example of this calculation can be seen in Figs. 3 & 4, showing the boundary shape comparison and coil current evolution for a high-elongation and triangularity discharge. This discharge was chosen because it is similar to the high-elongation and triangularity discharges utilized for NSTX-Upgrade simulations in the following sections, though of course at lower aspect ratio.

Fig. 3 shows the plasma boundary at three difference times during the discharge. The black curves show the experimental equilibrium as reconstructed by the LRDFIT reconstruction code [Menard 2006]. These particular calculations are constrained by magnetic field and flux measurements at the vessel wall and a requirement that the magnetic surfaces are an isotherm (based on midplane Thomson scattering data on both sides of the magnetic axis). The reconstruction is NOT constrained to match any measurement or estimate of the pressure profile. The boundary of this reconstructed equilibrium is input to TRANSP, which the free-boundary equilibrium code tries to match.

This equilibrium computed by ISOLVER within TRANSP is shown in red in Fig. 3. The three times correspond to a) the inner-wall limited phase just before the plasma is diverted, b) just before the end of the current ramp, and c) well into the flat-top. An excellent match to the plasma boundary is generally achieved. The internal surfaces, on the other hand, do not always agree as well. This is due to mismatches in the pressure profile between those in LRDFIT and TRANSP. The problem is especially severe in frame b), where 4 MW of heating power into a lower density plasma results in a very peaked pressure profile in TRANSP; the reconstruction do not have such a peaked profile, and have a smaller shift of the inner surfaces.

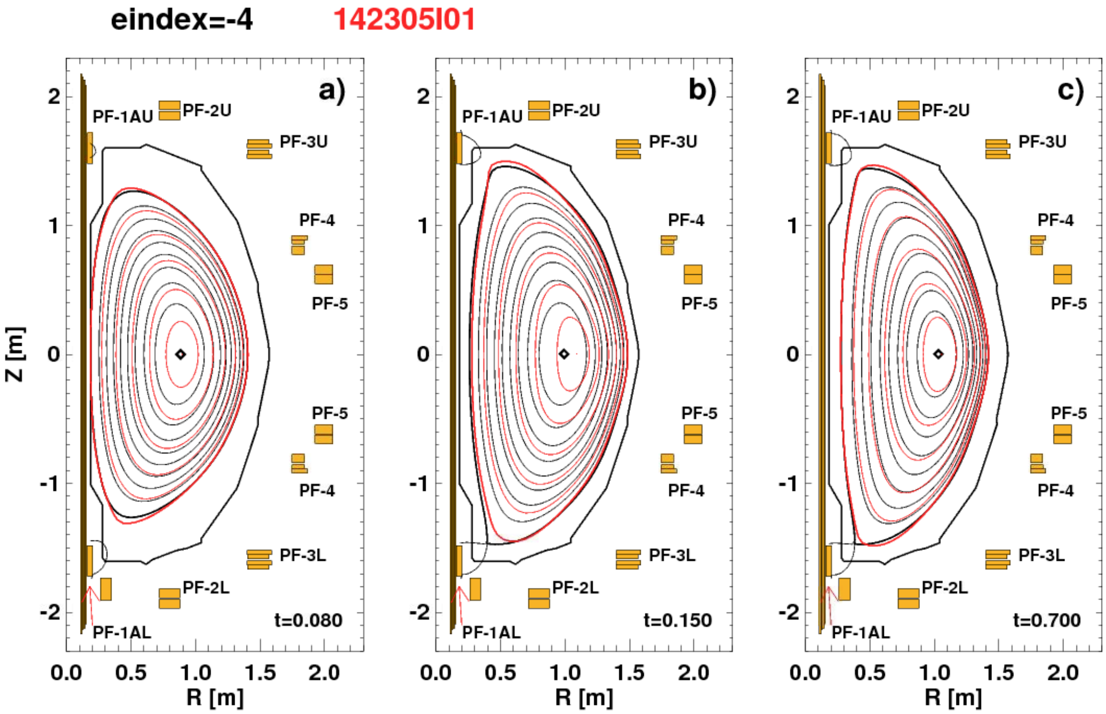


*Fig. 3: Comparison of the input and calculated equilibria using free-boundary TRANS.P*

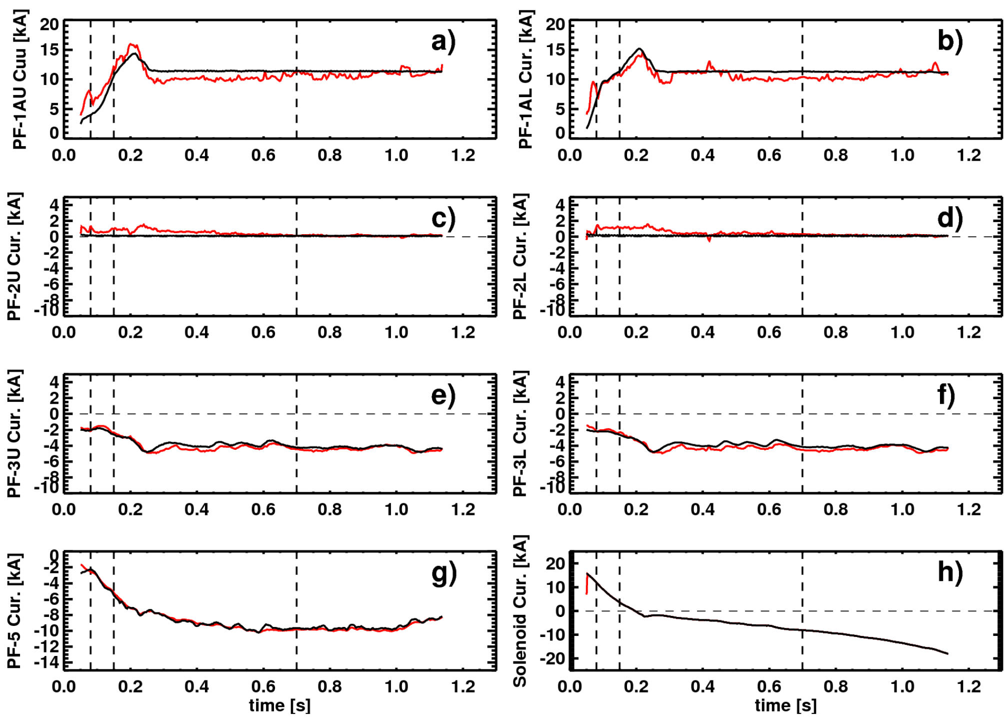


*Fig. 4: Comparison of the actual and computed coil currents. The locations of the various coils are indicated in Fig. 3, and the dashed vertical lines correspond to the times in Fig. 3. See text for additional details.*

The experimental and computed coil currents are indicated in Fig. 4, with the vertical dashed lines corresponding to the times in Fig. 3. Frames a) and b) show the currents in the two active divertor coils (PF-1AU & -1AL). Frames c) and d) show the currents in divertor coils that were not used in this discharge. Reasonable agreement is found for all four divertor coils; in particular the code does not attempt to put a significant level of current in the coils that were not energized. The PF-3 coils in frames e) and f) control the plasma vertical position, while the PF-5 coil in frame g) provides the main vertical field [Wesson] and controls the plasma midplane radius. These coils also show good agreement between the actual currents and those computed by TRANSP. Finally, because the solenoid is not well coupled to the plasma shape, the solenoid current in the TRANSP runs was forced to match to measured current evolution.

Note additionally that the TRANSP calculations do not have any vessel eddy currents. The actual experiments and reconstructions, however, have substantial vessel currents [Gates 2004], especially during the current ramp. These vessel currents are thus reflected in the coil currents computed by TRANSP, though this does not result in large discrepancies.

## 5: Parametric Considerations for Scenario Optimization

A large number of parameters influence the relaxed equilibrium state of the plasmas. In this section, we explore a number of these dependencies. In particular, the roles of the outer gap, plasma density and thermal confinement level, anomalous fast ion diffusion, ion thermal transport level, $Z_{eff}$, and profile shapes in determining the non-inductive current drive sources are addressed. These scans will lay the foundation for the scenario optimizations discussed in Sect. 6.

| Scenario | $I_P$ [MA] | $B_T$ [T] | $P_{inj}$ [MW] | $f_{GW}$ | A | Symbol/linestyle in Figs. 11, 14, and 15. |
|---|---|---|---|---|---|---|
| S1 | 1 | 1 | 12.6 (Six 90 kV Beams) | 0.72 | 1.73 (except for 5.6, when A=1.75 | Diamond/solid |
| S2 | 1.6 | 1 | 10.2 (80 kV Beams) | 0.86 | 1.75 | Squares/dotted |
| S3 | 1.2 | 0.55 | 8.4 (four 90 kV Beams | 0.72 | 1.81 | Triangle/dashed |

Table #1: Scenarios utilized in the sensitivity studies of sections 5.2-5.6. All cases in Section 5 have $H_{98y,2}$=1.0 unless otherwise stated.

The sensitivity studies in this section will be shown in the context of three different scenario targets, listed in Table #1, and denoted as S1-S3. These three discharge targets are broadly representative of the cases discussed in Section 6. The first (S1) is a $B_T$=1.0 T, $I_P$=1.0 MA, $P_{inj}=12.6$ MW scenario with A=1.73 (except in 5.6, where it is studied at A=1.75), designed to operate near 100% non-inductive current drive. The second (S2) is a $B_T$=1.0 T, $I_P$=1.6 MA, $P_{inj}=10.2$ MW scenario with A=1.75, designed to be sustained for ~5 seconds at high current. The third (S3) is a $B_T$=0.55 T, $I_P$=1.2 MA,

$P_{inj}$=8.4 MW designed to sustain high toroidal β of ~25% for ~3 seconds. All of these studies use the electron temperature and density profiles from high aspect ratio discharge 142301, except in Sect. 5.6, where the sensitivity of these results to the thermal profiles is discussed.

### *5.1 Role of the outer gap*

The plasma shape is a key parameter in determining the ability of a tokamak to achieve large bootstrap currents and sustain high-β [Lazarus 1991, Gryaznevich 1998, Gates 2003, Gates 2006, Gates 2007, Gerhardt 2011b]; NSTX-Upgrade is no exception to this rule. In general, it is desirable to keep the inner- plasma-wall gap as small as reasonably possible in order to maintain low aspect ratio; this results in the best utilization of the toroidal field. The elongation is optimized by making the plasma tall, consistent with maintaining gaps at the top and bottom. The plasma triangularity is maintained at a high level, also to improve utilization of the toroidal field [Gates 2003].

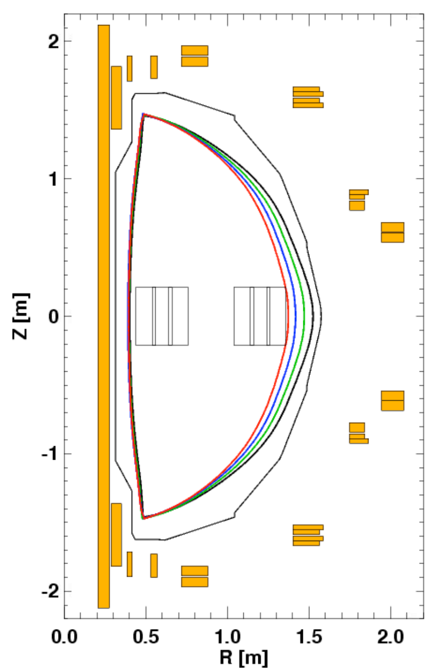


*Fig. 5: High-triangularity, double-null, target shapes used in the outer gap scan. CHECK THE BEAM FOOTPRINTS.*

This leaves the outer midplane plasma-wall gap, referred to from here on as the "outer gap", as the remaining low-order parameter for optimization (we note that the plasma "squareness" [Turnbull 1999] can also be optimized to improve performance [Holcomb 2009]). A smaller value of outer-gap results in a plasma that fully fills the vessel. It also brings the plasma close to the stabilizing plates. A large value of outer gap increases the elongation and causes the $R_{tan}$=120 and 130 cm sources to drive current farther off the magnetic axis.

A series of target plasma boundary shapes were created in order to understand this optimization. These shapes, shown in Fig. 5, have identical X-point and inner-midplane radii, and identical X-point height. The outer-gap was scanned from 5 cm to 20 cm, in 5 cm increments. The increase in the outer gap from 5 to 20 cm increase the elongation from 2.55 to 2.95, and the aspect ratio from 1.71 to 1.81.

An example configurations utilizing these boundary shapes, shown in Fig. 6, has $I_P$=1 MA & $B_T$=1T, with each of the 6 NB sources injecting 2.1 MW of power for a total of 12.6 MW injected. These scenarios have $H_{98}$=1 and Greenwald fractions $f_{GW}$=0.72, and are optimized to have a very large non-inductive fraction. The colors in the figure are a match to the requested boundary shapes in Fig. 5. The electron temperature is largely the same for these discharges, but the density increases for large outer gap (small minor radius) since $f_{GW} \propto \bar{n}_e a^2$. Also note that the 10 cm outer gap case is the S1 scenario of Table 1.

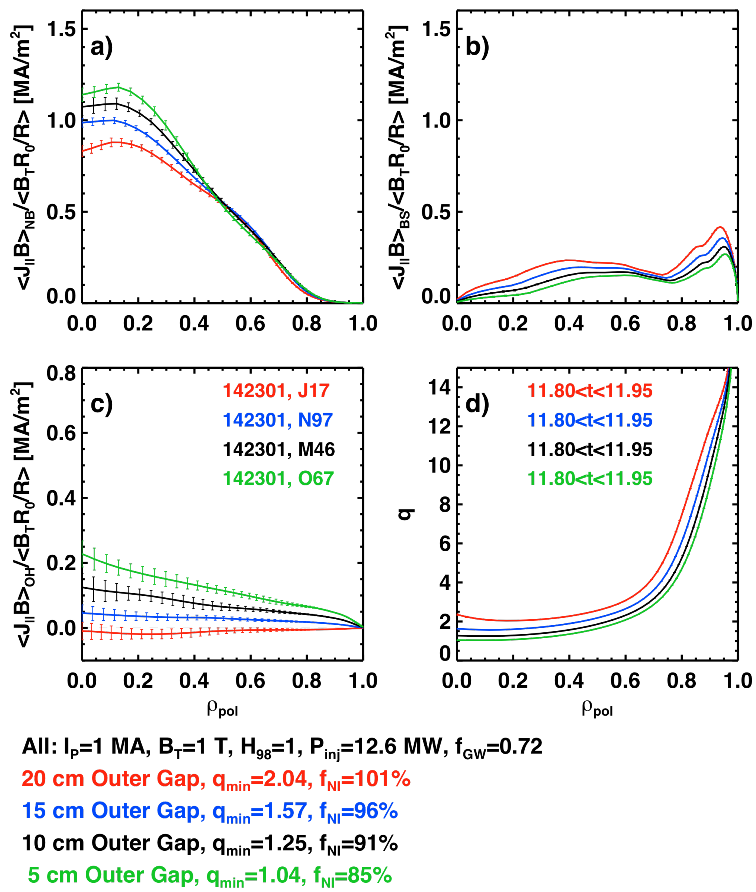


*Fig. 6: Variation of the current profile with outer gap for a 12.6 MW near non-inductive configuration. These scenarios have $f_{GW}$=0.72 and $H_{98}$=1, and the S1 scenario of table #1 is indicated in black.*

Considering the current profile constituents, we see that the neutral beam driven current becomes progressively less peaked as the outer gap becomes larger. This is due to both the more tangential aiming of the outermost beams with the larger gap and the increased central density in this fixed $f_{GW}$ example. The bootstrap current increases significantly for the larger gap, as the elongation is increased. The net result of these trends with increasing outer gap is to significantly reduce the residual Ohmic current and significantly increase the central safety factor.

A similar set of trends is visible in Fig. 7, which studies a configuration optimized for high toroidal $\beta$. This is accomplished by operating at $I_P$=1200 kA and $B_T$=0.55 T. Four neutral beam sources with acceleration voltage of 90 kV are utilized, with $R_{tan}$=[50,60,120,130] cm. The 20 cm outer gap point is the scenario S3 from table #1. The omission of the centrally directed beams with $R_{tan}$=70 and 110 cm is critical in avoiding excessive NBCD on axis, which can drive down $q_0$ (the optimization of the source mix will be discussed in greater detail in later sections).

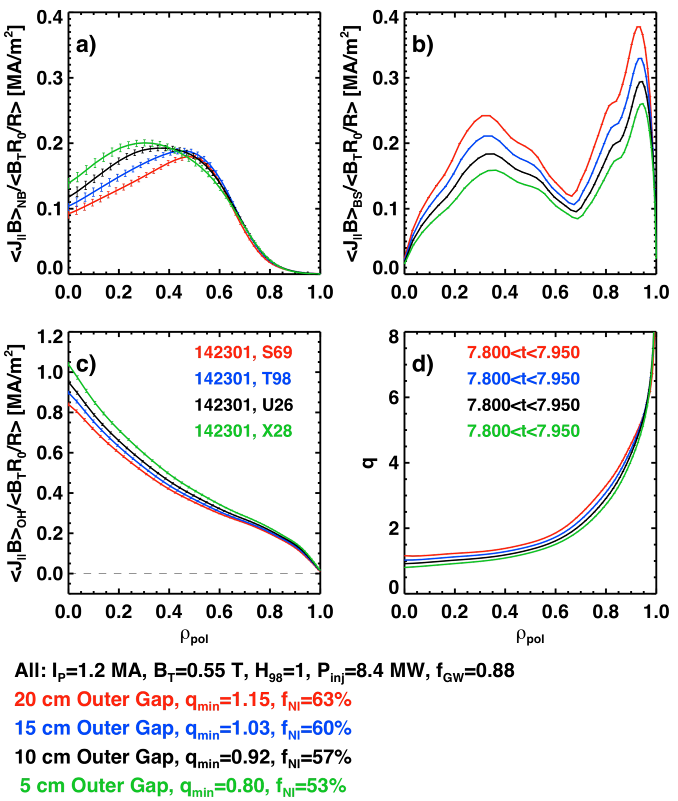


*Fig. 7: Variation in current profile results with outer gap for a $P_{inj}$=8.4 MW, $B_T$=0.55 T scenario designed to increase the sustainable $\beta_T$. These scenarios have $f_{GW}$=0.88 and $H_{98}$=1, and the S3 scenario of table #1 is indicate in red.*

The effect of outer gap in these scenarios is quite similar to that in Fig. 6, despite the different configurations. The NBCD profile is hollow in this case, with the peak in the driven current moving to successively larger radius as the outer gap is made larger, while the magnitude of the central current drive is reduced. Simultaneously, the bootstrap current increases as the outer gap is made larger and the elongation is increased. The inductive current on axis is thus reduced. The net effect is again to raise the central safety factor.

This dependence of $q_{min}$ on the outer gap (for all other parameters fixed) is illustrated more clearly in Fig. 8a. For the 1.0 MA & 1.0 T scan in red (see Fig. 6), the central safety factor drops from ~3 to 1.3 as the outer gap goes from 20 to 5 cm. The change in safety factor is less numerically dramatic, but perhaps more significant, in the $B_T$=0.55 T case, where $q_{min}$ >1 is only maintained for the largest outer gap. The maintenance of $q_{min}$>1 is critical for the ST, so as to avoid the onset of non-resonant m/n=1/1 kink modes, often coupled to 2/1 islands [Menard 2005, Menard 2006, Gerhardt 2009, Gerhardt 2011, Gerhardt 2012, Breslau 2011, Chapman 2010].

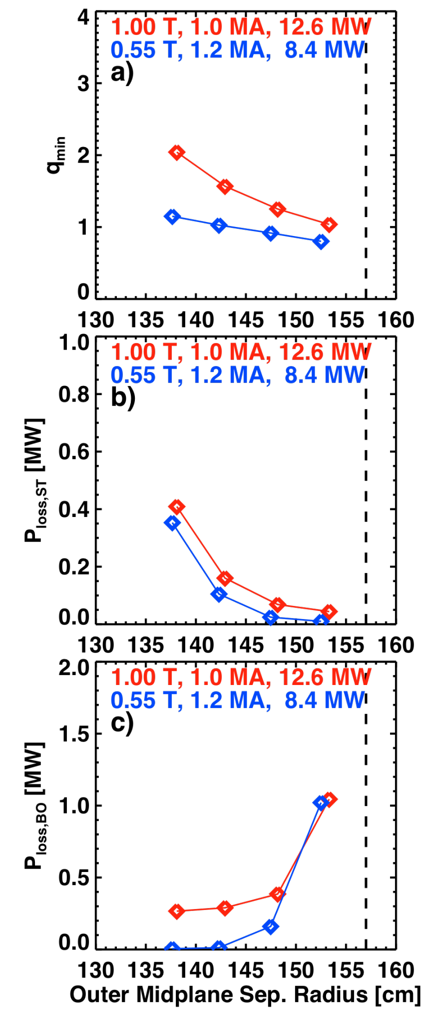


*Fig. 8: Variation of the a) central safety factor, b) the shine-through power, and c) the bad-orbit loss powers, as a function of the outer midplane separatrix radius, for the scans in Figs. 6 and 7. The radius of the outboard limiter is shown as a vertical dashed line.*

Fig 8 b) and c) show the shine through and bad orbit loss powers for the two configurations. The shine-through power is small for the 5 and 10 outer gaps, but becomes more significant for the 20 cm case. The bad orbit loss, on the other hand, is most significant for the small outer gap case, as the beams become more perpendicular. Overall these studies indicate that the optimal outer gap is likely in the 10-15 cm range for most scenarios, with the 20 cm case having utility when further raising the minimum safety factor is a requirement.

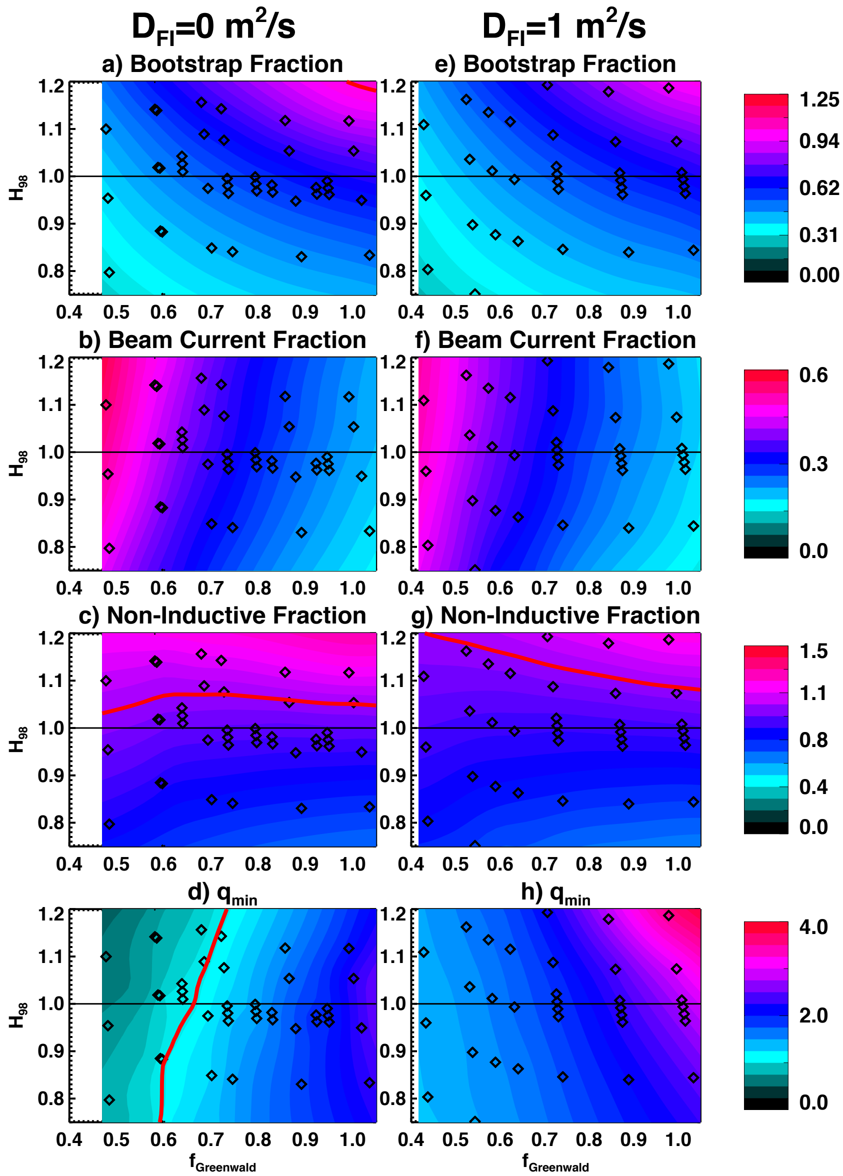


*Fig. 9: Comparison of the nearly 100% non-inductive S1 scenario without (left) and with (right) anomalous fast ion diffusion. The rows show the bootstrap fraction, NB current fraction, the total non-inductive fraction, and the central safety factor.*

## *5.2 Importance of the plasma density and confinement level*

A second set of key variables impacting the scenario are the plasma density and confinement level. This is can be seen in clearly in the left column of Fig. 9, where contours of the bootstrap faction, neutral beam current drive faction, total non-inductive fraction, and $q_{min}$ are plotted as a function of the Greenwald fraction and H-mode confinement multiplier $H_{98}$. The actual data points used in the calculation are shown as solid points, and the contours are an interpolation based on these points. This figure is for the S1 scenario with $B_T$=1.0T, $I_P$=1.0 MA, $P_{NB}$=2.1 MW from each of 6 NB sources each at 90 kV for $P_{inj}$=12.6 MW, and plasma boundary request with a 10 cm outer gap (A=1.73 and $\kappa$=2.7, corresponding to the green boundary in Fig. 5).

Contours of the bootstrap current fraction are shown in frame a). In 0-D analysis, the bootstrap fraction scales as $\sqrt{\varepsilon}\beta_P$, and so scales with the stored energy. Using the formulas in eqn. 1), we can write this dependence as roughly $Hn^{0.4}$ for either scaling expression. Thus, the bootstrap fraction increases with both variables in this figure, though more strongly with H. From Figs. 6 and 7, it is clear that increasing the bootstrap current will increase the amount of off-axis current, thus assisting in maintaining elevated $q_{min}$.

The beam current drive fraction is shown frame b). The beam current drive scales as $\frac{T_e^{3/2}}{n_e}P$, where the leading ratio is a surrogate for the slowing down time. Using $W=nT$, $W = HP\tau_{scaling}$ and $\tau_{scaling} \propto \sqrt{n_e}$ for either scaling law, we can calculate that to lowest order, $f_{NBCD} \propto f_{GW}^{-2}H^{3/2}$ (CHECK THIS!!!). Hence, we see an inverse dependence of the bean current drive fraction on the density, and a positive dependence on the confinement multiplier.

The net non-inductive fraction is shown in frame 9c. This is the sum of the beam driven currents, bootstrap current, and the Pfirsch-Schlueter and diamagenetic currents [Kessel 1994]. Interestingly, the total non-inductive current is roughly independent of the density for the range of densities and confinement considered here. For instance, increasing the density will decrease the neutral beam current drive, but increase the bootstrap current. This approximate independence of the non-inductive fraction from the density was noted before, for instance, in Ref. [Voitsekhovitch 2009].

The central safety factor, shown in Fig. 9d), is, however, not independent of the plasma density. Rather, reducing the density at fixed H tends to rapidly lower the central safety factor, as the central neutral beam current drive drives down $q_{min}$. As noted above, maintaining $q_{min}$>1 is critical for the avoidance of n=1 kink and coupled core/kink tearing modes, as documented in Refs [Menard 2005, Menard 2006, Gerhardt 2009, Gerhardt 2011, Gerhardt 2012, Breslau 2011, Chapman 2010]. Hence, this trend in $q_{min}$ provides a low-density limit for scenarios with fully relaxed current profiles.

### *5.3 Impact of anomalous fast ion diffusivity*

Because the neutral beams provide a substantial fraction of the current drive, it is worth considering what the effect of non-classical fast ion diffusion [Gunter 2007, Heidbrink 2009a, Heidbrink 2009b, Zhang 2008, Hauff 2009] would be on these scenarios. We have generally found that in the absence of low-frequency MHD activity, the beam current drive appears to be classical [Menard 2006, Gerhardt 2011]. However, Ref. [Gerhardt 2011a] shows that even in these MHD quiescent cases, fast ion diffusivities of up to ~1 $m^2$/s cannot be excluded.

Reference also shows a [Gerhardt 2011a] also analyses discharge with rapid Toroidal Alfven Eigenmode (TAE) avalanches [Fredrickson 2006, Podesta 2009, Fredrickson 2009]. The avalanches are modeled with bursts of fast ion diffusivity, with peak values of ~50 $m^2$/s, but durations of only typically 0.5-1.0 ms. This allows a match to both the typical neutron emission evolution over the avalanche and the average profile of neutral beam driven current drive. As part of the present study, that discharge was analyzed to determine single spatially and temporally constant diffusion coefficient that would match the average neutron emission and current profile. It turns out that $D_{FI}$=4 $m^2$/s can achieve this match, and this value will be used below as what might be typical of a discharge with these modes.

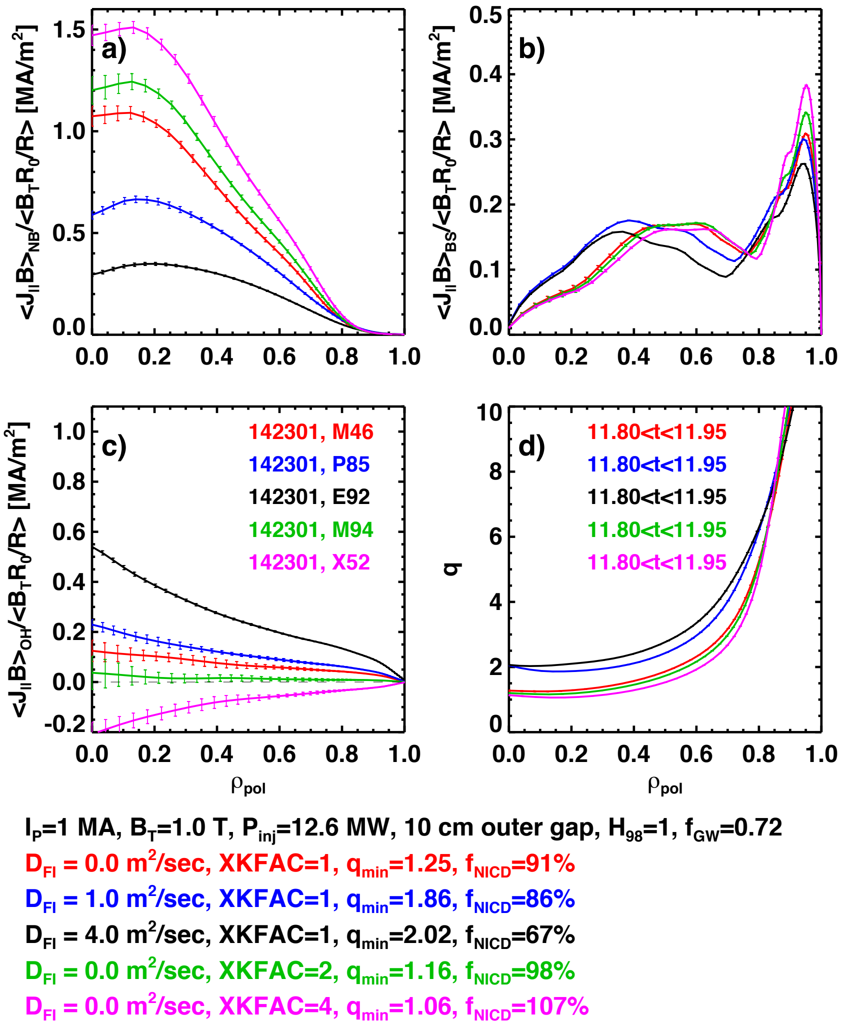


*Fig. 10: Profile comparison for the S1 scenario with $B_T$=1.0 T, $I_P$=1 MA, $H_{98y,2}$=1, with a 10 cm outer gap. The injected power is from six sources operating at 90 kV, for a total power of 12.6 MW, and the Greenwald fraction is $f_{GW}$=0.72. The different curves correspond to various levels of spatially uniform fast ion diffusivity $D_{FI}$ or multiplier XKFAC on the ion thermal diffusivity.*

To begin these studies, we have made calculations with a spatially uniform "anomalous" fast ion diffusivity $D_{FI}$=1m$^2$/s for the S1 scenario with $B_T$=1 T, $I_P$=1 MA, $P_{inj}$=12.6 MW. The results of this calculation are shown in the right hand column of Fig. 9; all other parameters are the same as in the left column. The bootstrap fraction in frames a) and e) is essentially the same. The beam current drive is reduced a meaningful amount on the low-density left-hand side of the plot, but less on the high-density right-hand side. Overall, the total non-inductive fraction for $H_{98}$=1 is decreased by 5 to 10% with $D_{FI}$=1 m$^2$/s, depending on the density. More significant, however, is the increase in the central safety factor when the fast ion-diffusivity is invoked. Over the range of densities and confinement considered in frame 9h), $q_{min}$ is maintained greater than 1 for $D_{FI}$=1 m$^2$/s, compared to a significant region with $q_{min}$<1 in frame 10c).

The reasons for this elevated central safety factor are shown more clearly in Fig. 10, where profiles for $H_{98}$=1, $f_{GW}$=0.72 scenarios are shown with various levels of fast ion diffusivity. We see that for $D_{FI}$=0 (the case in red), there is a highly peaked beam current drive profile. The central beam-driven current density is approximately 10 times larger than the Ohmic current in this case, and has a significantly more narrow profile. Increasing $D_{FI}$ to values of 1.0 and then 4.0 m$^2$/s results in a significant reduction of the central beam drive current, with the central parallel current density reduced by more than a factor of 2. There is some increase in the core bootstrap current as the central safety factor is increased [Ferron 2010], and some reduction of the edge bootstrap current. However, most of the lost NBCD is replaced with Ohmic current. The bet effect is to raise the central safety factor.

Figure 11 shows select parameters as a function of this spatially and temporally uniform fast ion diffusion coefficient. The grey region on the left indicates the range of $D_{FI}$ that is consistent with MHD quiescent discharges [Gerhardt 2011b], while the grey region on the right represents the TAE avalanche case. The S1 scenario ($I_P$=1.0 MA, $B_T$=1.0 T, $P_{inj}$=12.6 MW) considered so far in this section is indicated by solid lines and diamond symbols. Fig. 11a illustrates that the total non-inductive fraction drops from ~91% to 65%. The majority of this loss is due to the reduced beam current drive, although there is also some loss of bootstrap current.

Frame 11b) shows some additional equilibrium parameters plotted against this same fast ion diffusion coefficient. We define the pressure peaking factor $F_P$ as the central total pressure normalized to the volume average total pressure. The pressure peaking factor decreases substantially as the centrally peaked fast ion pressure is reduced; the central safety factor increases rapidly over the same range of $D_{FI}$. The internal inductance decreases slightly over the scan, as the centrally peaked beam current is replaced by the broader inductive current.

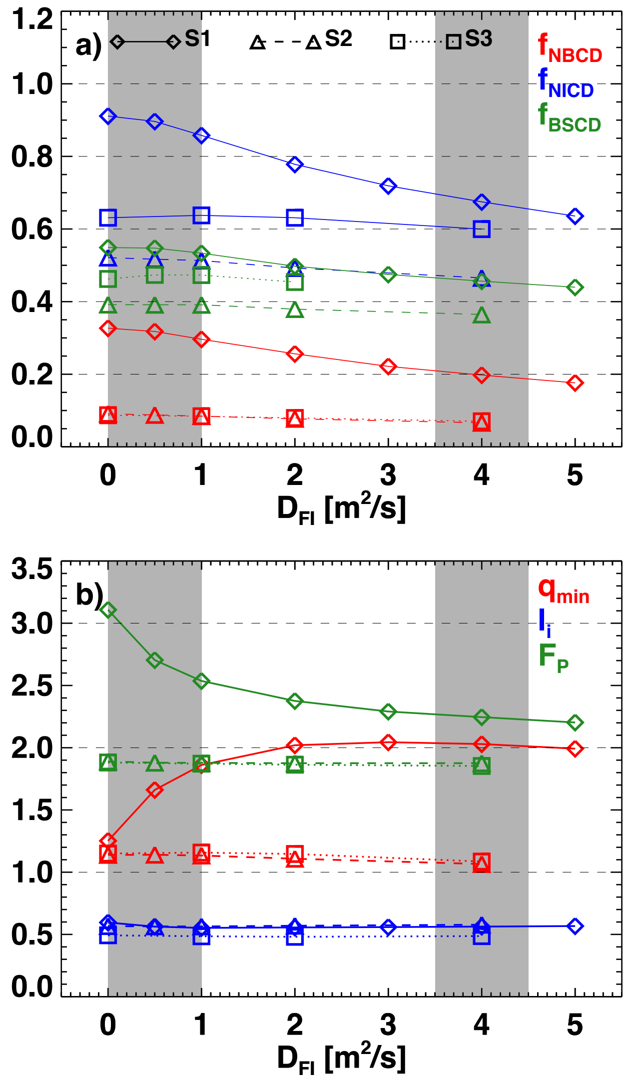


*Fig. 11: Various parameters as a function of the spatially and temporally constant fast ion diffusion coefficient. The diamonds are for the S1 scenario with $B_T$=1T, $I_P$=1 MA and $f_{GW}$=0.72 , the triangles for the S2 scenario with 1.2 MA, 0.55 T and $f_{GW}$=0.86, and the squares for the S2 scenario with 1.6 MA, 1.0 T, and $f_{GW}$=0.72 . See text for additional details.*

The profile changes that result from even the rather small value of $D_{FI}$=1 m$^2$/s are generally beneficial to the ideal n=1 stability of the configuration, as shown in Fig. 12. The left column of plots shows the parameters for $D_{FI}$=0, while the right columns is for $D_{FI}$=1 m$^2$/s. The top row shows the value of $\beta_N$, while the second row shows the pressure peaking factor, both as a function of confinement multiplier and Greenwald fraction. It is clear that the normalized $\beta$ is similar between the two cases, but that the total pressure peaking is significantly reduced at lower density when $D_{FI}\neq0$ . This reduction in pressure peaking is well known to have beneficial effects on the global ideal stability [Howl 1992, Strait 1994, Lazarus 1996, Sabbagh 1996, Sabbagh 2002, Menard 2003, Sabbagh 2004, Ferron 2005, Sips 2005, Luce 2011]

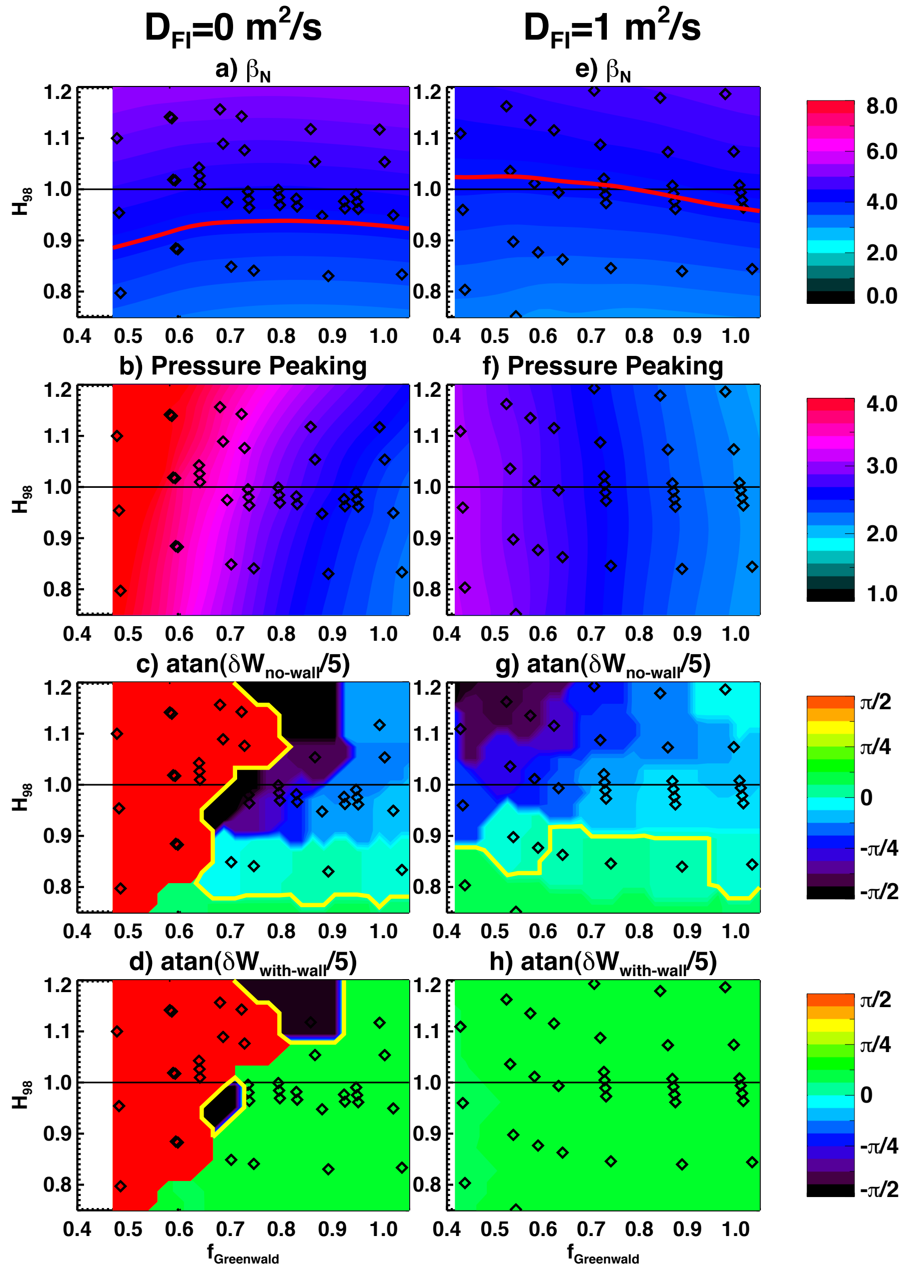


*Fig. 12: Stability related parameters as a function of the confinement multiplier and Greenwald fraction. Shown are a) and e): $\beta_N$, b) and f): the pressure peaking factor, c) and g) the no-wall n=1 stability parameter, and d) and i) the with-wall n=1 stability parameter. The dark red colors for the $\delta W$ plots correspond to internal modes becoming unstable. The red lines in frames a) and e) correspond to the $\beta_N$ =4 contour.*

The effects of these profile modifications on the global stability is shown in the bottom two rows of the figure. These frames show contours of a stability parameter atan($\delta W$/5), where $\delta W$ is computed with DCON as described in Sect. 3c. The *atan* here is used to bound data, as the quantity $\delta W$ can become very negative for strongly unstable configurations, causing a contour plot of $\delta W$ itself to be difficult to interpret; the use of the *atan* compresses the data, while maintaining the rule that $\delta W >0$ is indicative of stability. DCON also predicts when purely internal modes are unstable, and these cases are shown in bright red in the figures.

Frame 12c) shows contours of the stability parameter for the case with $D_{FI}$ = 0 m$^2$/s. The left side of the frame is dominated by internal instabilities due to the central safety factor becoming too low. The right side of the plot is found to be unstable to external modes for $H_{98}>0.7$. The inclusion of a superconducting wall changes the results as shown in frame 11d). The internal modes at lower density are not modified by the addition of the wall. A stability window does open at higher density, though it appears to be somewhat limited by the large pressure peaking factor.

Frame 12g) shows the no-wall stability for the case with $D_{FI}$=1 m$^2$/s. The increased central safety factor leads to an immediate improvement of the global stability, with the internal modes totally eliminated over this range of densities and confinement. However, confinement multipliers greater than $H_{98}$~0.9 lead to unstable external modes in the absence of a conducting wall. As shown in frame 12h), these external modes can be eliminated by the conducting wall, and robust n=1 ideal stability is predicted over this operating range.

Of course, when the value of $\beta_N$ exceeds to the no-wall limit, but is less than the with-wall limit, then the configuration is in the wall-stabilized regime [Strait 1995, Menard 2004] where the resistive wall mode [Bondeson 1994] can be a performance limiting instability. Indeed, NSTX has observed and documented many features of the RWM stability in a spherical torus [Sabbagh 2004, Sontag 2005, Reimerdes 2006, Sabbagh 2006a, Sabbagh 2006b, Sontag 2007, Sabbagh 2010a, Sabbagh 2010b, Menard 2010]. Calculations of the resistive wall mode stability is not within the scope of the paper. However, we note that when sustaining the rotation with error-field correction [Gerhardt 2010, Menard 2010] and avoiding the RWM with fast n=1 feedback [Sabbagh 2006a, Sabbagh 2010a, Sabbagh 2010b], reliable operation in the wall-stabilized regime has been achieved.

The effect of additional fast ion diffusivity on the S3 scenario is shown in Fig. 13; recall that S3 is the $B_T$=0.55 T, $I_P$=1.2 MA, $P_{inj}$=8.4 MW scenario designed to study fully relaxed high toroidal β scenarios. The case with $D_{FI}$=0 m$^2$/s has a hollow beam drive current profile, with the peak at p~0.5 and the magnitude of the central value approximately ½ that of the peak (this case was also shown in Fig. 7). Going to $D_{FI}$=1 m$^2$/s actually raises the central current drive, while decreasing the midradius peak. $D_{FI}$=4 m$^2$/s results in a significant drop in the core NB current drive, but a noticeable increase in the outer ½ of the plasma. Overall the minimum safety factor drops at $D_{FI}$ is increased, but only from 1.14 to 1.08, with a slightly non-monotonic behavior near $D_{FI}$=1 m$^2$/s.

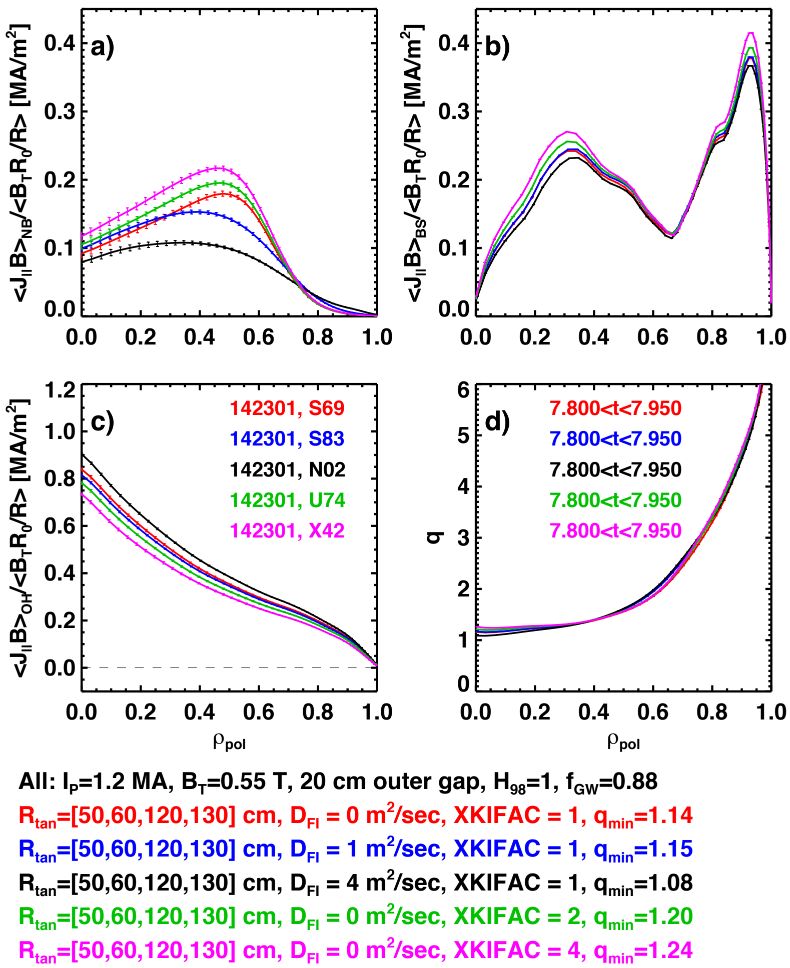


*Fig. 13: Example profiles for the S3 scenario with $B_T$=0.55 T, $I_P$=1200 kA. designed for maximizing the sustained $\beta_T$ with 4 sources and 8.4 MW of input power. The difference cases correspond to different assumptions on the fast ion diffusivity and ion thermal transport.*

These trends are illustrated with the triangles and dashed lines in Fig. 11. Frame a) shows that the non-inductive current drive components are largely independent of $D_{FI}$ in this scenario. Furthermore, frame b) shows that the variations in pressure peaking, $q_{min}$, and $l_{ie}$ are quite small.

Frame 11 also shows, with squares and dotted lines, the impact of fast ion diffusivity on the partial inductive, long pulse S2 scenario, with $I_P$=1600 kA, $B_T$=1.0 T, and six sources injecting with an acceleration voltage of 80 kV. This scenario is ~55% non-inductive at $D_{FI}$=0, mostly from the bootstrap current. Hence, the current-drive components in this type of scenario are largely independent of the chosen $D_{FI}$. Similarly, the global parameters $l_{id}$ and $F_P$, as well as the minimum safety factor, are largely independent of the fast ion diffusivity at the levels studied.

It should be noted that fast-particle MHD, and the associated loss of fast particles, can be quite deleterious to scenarios even if they do not significantly impact the current drive. For instance, fishbone modes have been observed to trigger NTMs (Gude 1999, Gerhardt 2009) and RWMs (Okabayashi 2011), the latter presumably due to the loss of fast particle stabilization (Berkery 2010a, Berkery 2010b, Berkery 2011a, Berkery 2011b, Reimerdes 2011). Hence, it is likely necessary to develop operating regimes that are free of fishbones and TAE avalanches.

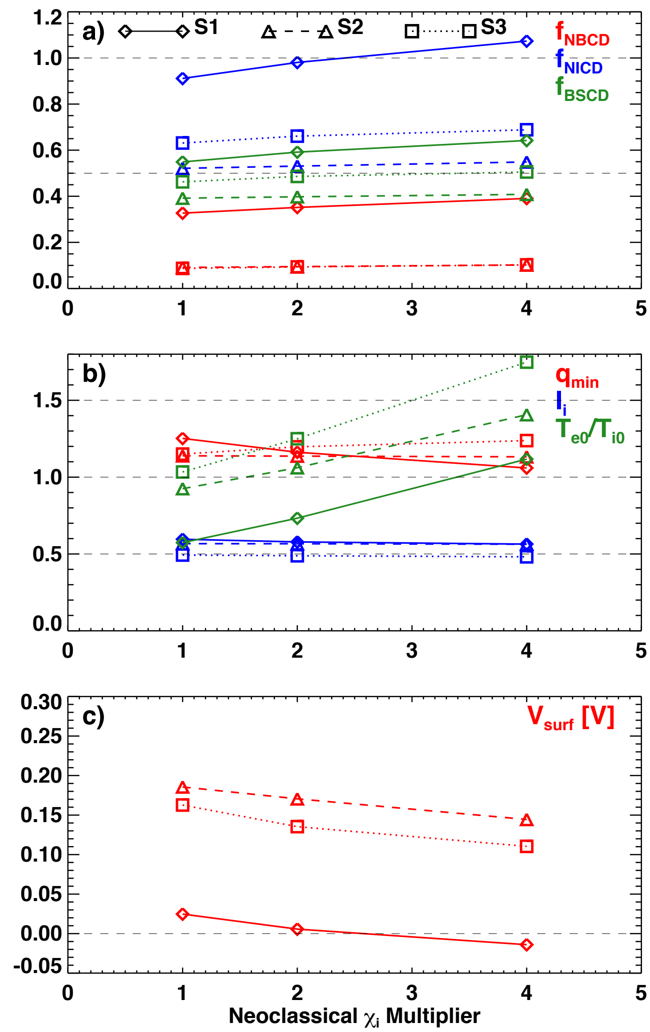


*Fig. 14: Variation of selected quantities as a function of the multiplier on the ion neoclassical thermal diffusion coefficient, for fixed overall confinement. The symbols and linetypes correspond to the same discharge scenarios as in Fig. 11 and are explained in detail in Table 1. See text for additional details.*

### *5.4 Impact of variations in the ion thermal transport.*

As noted above, the ion thermal diffusivity in these simulations is determined by the Chang-Hinton model, with the experimental electron temperature profile scaled from experimental profiles to achieve a given confinement level. Under these rules it is interesting to consider how the results change when the ion thermal diffusivity is increased.

An example calculation is shown in Fig. 10, where the thermal ion diffusivity in increased by a factors of 2 and 4; these are denoted by XKFAC=2 & XKFAC=4 in the legend, and should be compared to the XKFAC=1 curve in red. We see that increasing this multiplier results in an increase in the centrally peaked NB current drive profile. The fundamental reason for this is that fixing the overall confinement to match a scaling expectation will result in a fixed stored energy. If the ion transport is increased and the ion temperature decreases, the electron temperature must increase to compensate. This higher $T_e$ then increases the NB current drive efficiency. The increased NB currents result in a decrease in the inductive current component, so that fully non-inductive or overdriven scenarios occur at high values of this ion confinement multiplier. However, this increased central NB current also drives down the central safety factor, with the XKFAC=4 case perilously close to $q_{min}$=1.

Similar trends with XKFAC are observed in Fig. 13, for the high $\beta_T$ S3 scenario. The beam current drive increases significantly at XKFAC is increases, leading to a significant drop in the inductive currents. However, given the hollow NB current profile, these trends result in the central safety factor increasing. This will tend to improve the global stability of the configuration.

Selected parameters are shown directly as a function of this multiplier in Fig. 14. The symbols and linestyles are the same as in Fig. 11 and are described in Table #1. The near non-inductive S1 scenario with 1 MA, 1T, $P_{inj}$=12.6 MW case is illustrated by solid lines and diamonds. As noted above, this case has a non-inductive fraction of 91% with ion neoclassical thermal transport. Artificially increasing the ion thermal transport by a factor of ~2.3 at fixed $H_{98y,2}$=1 yields fully non-inductive operation, as evidenced by the non-inductive fraction plot in frame a) and the surface voltage in frame c). Increasing the neoclassical ion transport by a full factor of 4 results in significant non-inductive overdrive. The ratio $T_e/T_i$ goes from essentially unity with neoclassical ion transport, to ~1.75 at the highest neoclassical multipliers considered.

The behavior of the partial inductive S2 & S3 scenarios is also illustrated in Fig. 14, and shows similar trends. The non-inductive fraction increases with the transport multiplier, mainly due to increases in the bootstrap current (the NBCD is small in these cases). The ratio $T_e/T_i$ increases by the same factor of ~1.5-1.8, and the surface voltage drops.

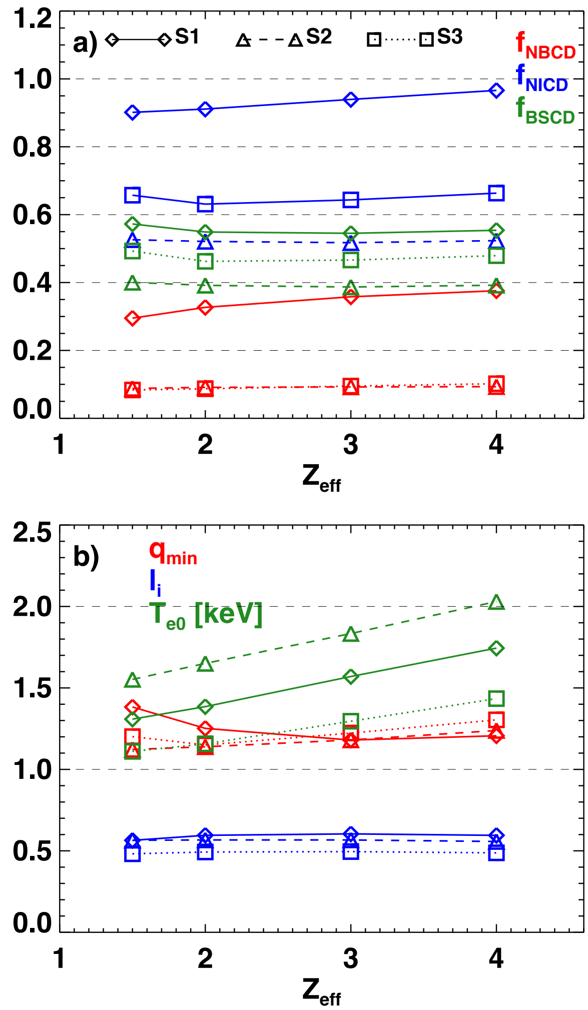


*Fig. 15: Variation of selected quantities as a function of $Z_{eff}$. The symbols and linetypes correspond to the same discharge scenarios as in Fig. 11 and are explained in detail in Table 1. See text for additional details.*

### 5.5 Sensitivity to variations in $Z_{eff}$

The next variation to be considered is that of $Z_{eff}=(n_D Z_D^2+n_C Z_C^2)/n_e$, where the subscript D and C refer to deuterium and carbon (the latter assumed to be the only impurity present due to the graphite plasma facing components in NSTX). The value of $Z_{eff}$ can change the scenario, for instance, through collisionality effects on the bootstrap current and neoclassical resistivity [Sauter 1999] or the neutral beam current shielding factor [Fisch 1987, Lin-Liu 1997]. However, the assumption utilized here of following a given global confinement expression will somewhat modify the expectations from current drive theory alone. In particular, increasing $Z_{eff}$ at fixed temperatures result in a decrease of the stored energy, as the deuterons are diluted. Hence, the plasma temperatures must increase with $Z_{eff}$ if the global confinement is to be maintained. We emphasize that this is not a physics result, but rather the unavoidable consequence of using a 0D scaling assumption to set the temperature profile instead of a complete transport model.

With this caveat, the trends with $Z_{eff}$ for the S1-S3 scenarios are shown in Fig. 15. The non-inductive current drive tends to be constant or increase slightly is $Z_{eff}$ is increased. The beam driven currents provide the slight increase in the S1 scenario, with the bootstrap currents largely constant. The central electron temperature is shown in frame b), and shows a significant increase in order to maintain constant global confinement. The central safety factor shows a slight increase with $Z_{eff}$, except for the S1 scenario, where is decreases and then flattens. The internal inductance is largely unchanged. For these reasons, we infer that the scenarios are largely insensitive to variations in $Z_{eff}$ around the $Z_{eff}$=2 operating point assumed in this paper, *provided the global confinement is not degraded with changes in $Z_{eff}$.*

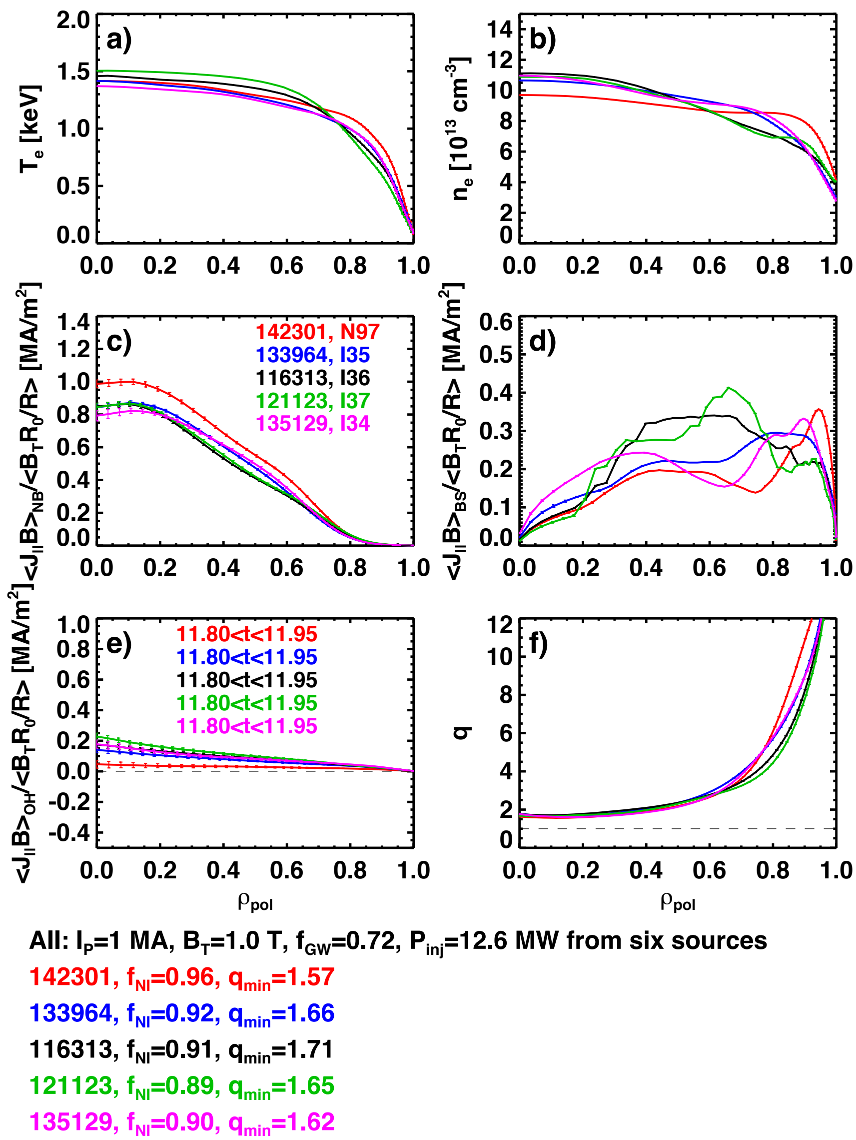


*Fig. 16: Examples of how various thermal density and temperature profile shapes impact the current profile and non-inductive current level for the near non-inductive S1 scenario.*

### *5.6 Impact of variations in the thermal profile shape*

The final study to be completed here is with regard to the impact of various profile shape assumptions on these scenarios. We begin this study in Fig. 16 with the S1 scenario, which had with $I_P$=1 MA, $B_T$=1.0 T, and all six available sources injecting at 90 kV, for a total input power of 12.6 MW. However, this figure is for slightly higher elongation (2.8 instead of 2.7), and aspect ratio (1.75 instead of 1.73). As noted in Section 5.1, this change will tend to increase the non-inductive fraction. The confinement level is specified by $H_{98}$=1 for all cases, and the Greenwald fraction is ~0.71

With regard to non-inductive fraction, we observe that the best profiles are those from discharge 142301 in red, with a non-inductive fraction of 96%. This case has comparatively broad density and temperature profiles, and will be referred to below in this context. Note that these profiles were taken from a high aspect ratio discharge designed to prototype NSTX-Upgrade operation [Gerhardt 2011b]. The profiles from discharge 121123 are least favorable, in the sense of having the lower non-inductive fraction for the given confinement multiplier. Furthermore, the rather peaked temperature profile results in the relaxed Ohmic current density profile becoming more peaked than other cases, which tends to drive down the central safety factor. This set of profiles will be referred to as "peaked" in the discussion below.

We repeat this exercise in Fig. 17, for the high $\beta_T$ S3 scenario at $I_P$=1.2 MA and $B_T$=0.55 T, and $P_{inj}$=8.4 MW from the $R_{tan}$=[50,60,120,130] cm sources. The primary optimization in this high-current scenario is to increase the minimum safety factor. As with the near non-inductive cases described in Fig. 16, the profiles from discharge 142301 result in the largest value of $q_{min}$. Furthermore, the profiles from 121123 result in the lowest value of $q_{min}$, due to the peaking of the profiles.

Finally, we have studied the effect of these various profile shapes on the partial inductive S2 scenario. The non-inductive fraction and central safety factor using the 142301 profiles are 52% and 1.13, respectively. These numbers are reduced to 45% and $q_{min}$=0.7 for the 121123 profiles. The other profile shapes lead to intermediate values of these parameters.

Given these results, we will use the profiles shapes from discharges 142301 & 121123 to provide bounds on the performance in Sections 6 & 7 below.

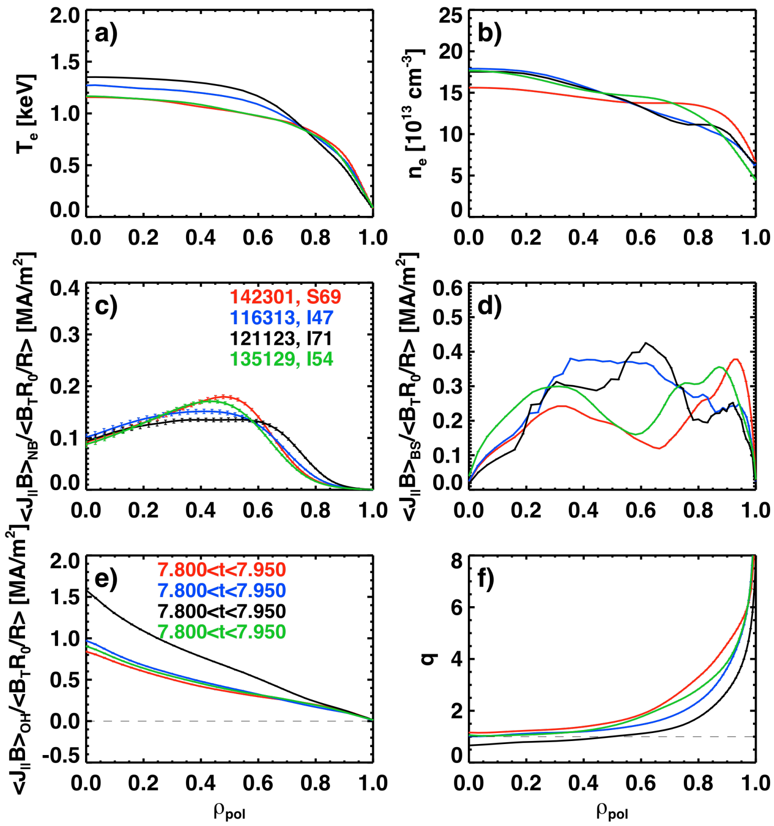


**All: $I_P$=1200 kA, $B_T$=0.55 T, 90 kV, $R_{tan}$=[50,60,120,130], $f_{GW}$=0.89, $H_{98}$=1**

**142301, $f_{NI}$=0.63, $q_{min}$=1.15**

**116313, $f_{NI}$=0.65, $q_{min}$=1.01**

**121123, $f_{NI}$=0.56, $q_{min}$=0.66**

**135129, $f_{NI}$=0.64, $q_{min}$=1.03**

*Fig 17: Effect of the various profile assumptions on the high-$\beta_T$ scenario S3.*

### *5.7 Summary of parametric dependencies for scenario design*

The results of these studies indicate the general trends that will be exploited below. In general, the desirable scenarios will have large outer gaps in order to maintain an elevated central safety factor. We will use 15 cm outer gaps for most of the studies described below. The exception will be the high $\beta_T$ optimization at $B_T$=0.55 T, where a 20 cm outer gap will be used.

The scenarios will also generally optimize to higher Greenwald fractions. Below, we will generally focus on cases with $0.7<f_{ew}<0.75$, though we will also consider some cases with higher values. These latter will be important when trying to keep the central safety factor elevated at very high plasma currents, as the high densities favor the bootstrap current, which goes to zero on the magnetic axis.

With regard to anomalous fast ion diffusion, some scenarios are considerably more sensitive than others. The near non-inductive scenario with highly peaked fast ion current (S1) appears to be quite sensitive to the imposed $D_{FI}$, with $D_{FI}$=1 $m^2$/s having a major impact on the equilibrium and stability. The partial inductive scenarios (S1 & S2), however, have a broader fast ion current profile and a smaller fraction of the total current driven by those ions. These scenarios are not significantly affected by this level of fast ion diffusivity.

The effects of scanning the ion transport level and $Z_{eff}$ with fixed global confinement were studied in section 5.4. Increasing the ion thermal transport, or equivalently, the ratio $T_e/T_i$, was found to be beneficial for the configurations: the required inductive voltage dropped and the non-inductive fraction increased. The configurations were largely insensitive to changes in $Z_{eff}$, provided that the global transport is fixed. All simulations below will utilize $Z_{eff}$=2, and ion thermal transport given by neoclassical theory without additional multiplier.

Finally, the profiles from the discharges 142301 and 121123 were picked as bounding the performance for all other parameters fixed. These tend to differ in their non-inductive current fraction of ~10%, but to have larger variations in the central safety factor. These two sets of profiles will be used in the studies in the following two sections.

## 6: Scenario optimizations for different physics studies.

As noted in the introduction, this section addresses a number of important scenarios for NSTX-Upgrade that support the physics program.

### *6.1 High-current 100 % non-inductive scenarios at $B_T$=1.0 T and 0.75 T*

A major goal of the NSTX-U project is to demonstrate stationary 100% non-inductive operation, using pressure and neutral beam driven currents to sustain the configuration. In this section we explore 100% non-inductive current capability at $B_T$=1.0 & 0.75 T, using various levels of acceleration voltages for the beam sources.

Fig. 18 presents calculations of fully non-inductive operating points, in a format that will be common for the remainder of this paper. The content of the individual frames is the same as Figs. 16 & 17. Each color represents a given configuration, where configuration refers to the boundary shape, heating power, toroidal field, and Greenwald fraction. The solid line corresponds to $H_{ST}$=1 and the dashed line indicates the result with $H_{98y,2}$=1. The data in this figure have $B_T$=1T, and utilize the 15 cm outer gap shape. Note that the Ohmic current profiles in frame e) are all perfectly flat and equal to zero, verifying that these scenarios would not require any inductive current (though we note that having the solenoid continue to help regulate the plasma current level against confinement transients could be advantageous for the stability of the configuration, as discussed in Ref. [Politzer 2005]).

The red curves correspond to the non-inductive level for each of six sources injecting 1.7 MW at 80 kV, using the broader profiles from discharge 142301. As indicated by the caption beneath the frames, confinement giving $H_{98}$=1 yields a non-inductive current level of ~870 kA, with a central electron temperature of ~1.3 keV. Assuming confinement equivalent to $H_{ST}$=1.0 for these broad profiles yields electron temperatures of ~1.9 keV and non-inductive current levels of 1225 kA. The strong difference between these scaling expressions is due to the different $B_T$ exponents: 0.15 for the ITER-98 scaling expression vs. 1.08 for the ST scaling. The more peaked thermal profiles (blue curves) yield somewhat lower non-inductive current levels of 750 and 1200 kA for the ITER-98 and ST scaling laws.

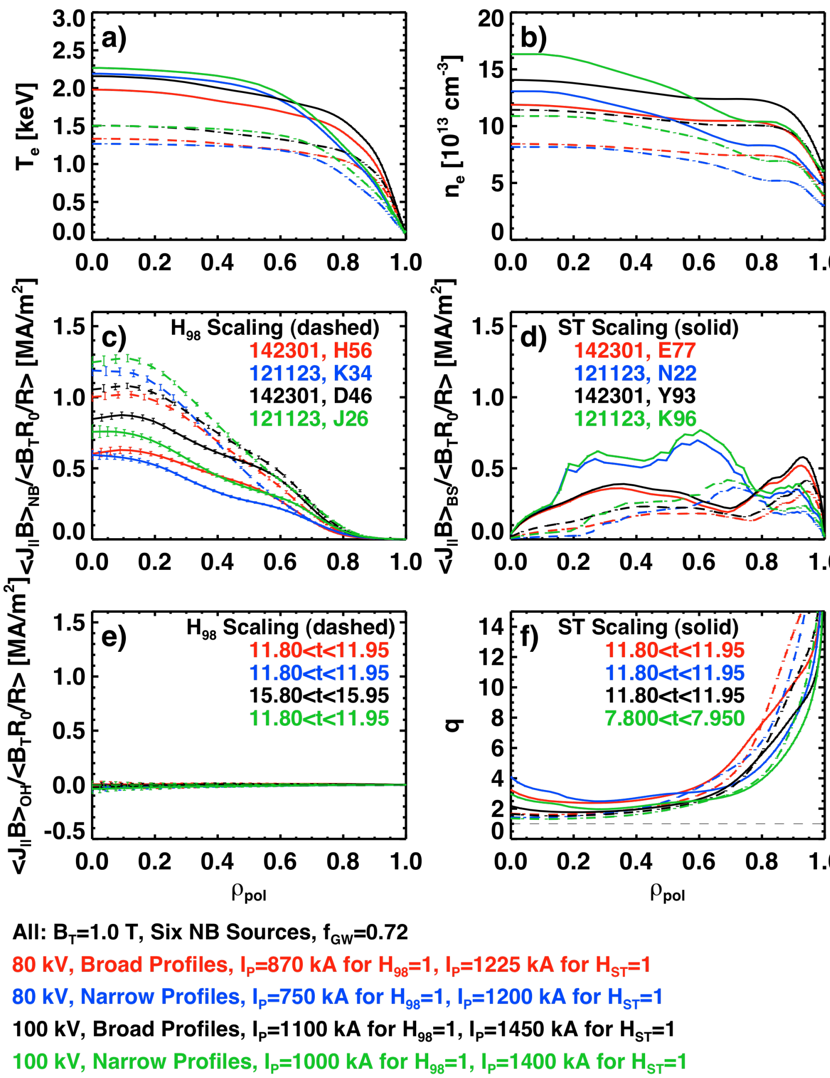


*Fig. 18: Example 100% non-inductive scenarios under different confinement and profile assumptions. Shown in this and similar figures are profiles of a) the electron temperature, b) the electron density, c) the beam-drive current, d) the bootstrap current, e) the Ohmic current, and f) the safety factor. The solid curves show the expectations assuming $H_{ST}$=1 governs the confinement; the dashed curves are for $H_{98}$=1. See caption and text for further details of the different scenarios.*

Also shown in the figure are calculations for cases with each of the neutral beams injecting at 100 kV, for a total power of 15.6 MW. The neutral beams are capable of operating up to 1.5 seconds in this configuration. For the broad profiles, the current levels range between 1100 and 1450 kA, with temperatures ranging from 1.5 kV to 2.2 keV, depending on the thermal confinement scaling. The more narrow profiles here reduce the non-inductive level by 50-100 kA, but raise the central electron temperature to 2.3 keV in the case with the ST confinement scaling.

We also note here that some of these scenarios tend to have a rather elevated minimum safety factor, and sometimes significant reversed magnetic shear. Reversed shear in NSTX has, in some instances, triggered the formation of internal transport barriers [Stutman 2006, Levinton 2007, Yuh 2008]. It is for these cases that the assumed profile shapes may be most marginal, as they came from scenarios with normal shear and minimum safety factors in the range of 1.1-1.3.

We have done a similar optimization for 100% non-inductive scenarios with four beam sources at $B_T$=0.75 T. In these cases, the $R_{tan}$=[50,60,120,130] sources are used for the optimization (the choice of these beam sources will be discussed in greater detail in Sects 6.4 and 6.5). As shown in Table 1, for the acceleration voltages of 80 kV at this toroidal field, the non-inductive current levels are found to be in the range of 600-800 kA, depending on the profile and confinement assumptions. For 90 kV acceleration voltages, the range is 675-865 kA.

| Voltage [kV] | Profiles | Scaling | $B_T$ [T] | $I_p$ [kA] | $f_{BS}$ | $q_{min}$ | $q_{95}$ | $\nu^*_{e,\rho=0.5}$ | $\tau_{CR}$ [s] | $\beta_N$ | $\beta_P$ | $W_{tot}$ [kJ] | $W_{fast}/W_{tot}$ |
|---|---|---|---|---|---|---|---|---|---|---|---|---|---|
| 80 | Broad | H98=1 | 1 | 870 | 0.67 | 1.60 | 18.69 | 0.14 | 0.41 | 4.04 | 2.39 | 457 | 0.26 |
| 80 | Broad | HST=1 | 1 | 1225 | 0.74 | 2.37 | 13.37 | 0.07 | 0.72 | 4.92 | 2.09 | 792 | 0.14 |
| 80 | Narrow | H98=1 | 1 | 750 | 0.63 | 1.41 | 20.90 | 0.11 | 0.33 | 4.26 | 2.87 | 415 | 0.34 |
| 80 | Narrow | HST=1 | 1 | 1200 | 0.74 | 2.48 | 12.81 | 0.04 | 0.72 | 5.26 | 2.24 | 828 | 0.16 |
| 90 | Broad | $H_{98}$=1 | 1 | 975 | 0.62 | 1.50 | 16.21 | 0.11 | 0.45 | 4.34 | 2.28 | 550 | 0.26 |
| 90 | Broad | $H_{ST}$=1 | 1 | 1325 | 0.72 | 2.03 | 12.28 | 0.06 | 0.78 | 5.32 | 2.09 | 925 | 0.15 |
| 90 | Narrow | $H_{98}$=1 | 1 | 875 | 0.60 | 1.39 | 17.10 | 0.08 | 0.38 | 4.58 | 2.64 | 520 | 0.32 |
| 90 | Narrow | $H_{ST}$=1 | 1 | 1300 | 0.70 | 2.10 | 11.58 | 0.03 | 0.75 | 5.57 | 2.19 | 948 | 0.17 |
| 100 | Broad | $H_{98}$=1 | 1 | 1100 | 0.64 | 1.52 | 14.42 | 0.10 | 0.49 | 4.81 | 2.24 | 689 | 0.23 |
| 100 | Broad | $H_{ST}$=1 | 1 | 1450 | 0.68 | 1.76 | 11.06 | 0.05 | 0.83 | 5.73 | 2.05 | 1089 | 0.16 |
| 100 | Narrow | $H_{98}$=1 | 1 | 1000 | 0.55 | 1.31 | 14.53 | 0.07 | 0.42 | 4.87 | 2.46 | 632 | 0.31 |
| 100 | Narrow | $H_{ST}$=1 | 1 | 1400 | 0.67 | 1.82 | 10.66 | 0.03 | 0.79 | 5.97 | 2.17 | 1093 | 0.18 |
| 80 | Broad | H98=1 | 0.75 | 635 | 0.71 | 0.98 | 19.79 | 0.23 | 0.29 | 4.34 | 2.63 | 266 | 0.32 |
| 80 | Broad | HST=1 | 0.75 | 800 | 0.73 | 1.53 | 15.49 | 0.13 | 0.41 | 4.78 | 2.32 | 374 | 0.23 |
| 80 | Narrow | H98=1 | 0.75 | 600 | 0.70 | 0.81 | 20.97 | 0.13 | 0.26 | 4.92 | 3.12 | 286 | 0.40 |
| 80 | Narrow | HST=1 | 0.75 | 770 | 0.71 | 1.72 | 15.57 | 0.07 | 0.39 | 5.25 | 2.61 | 396 | 0.27 |
| 90 | Broad | $H_{98}$=1 | 0.75 | 725 | 0.65 | 1.10 | 16.74 | 0.16 | 0.32 | 4.68 | 2.48 | 328 | 0.31 |
| 90 | Broad | $H_{ST}$=1 | 0.75 | 865 | 0.69 | 1.36 | 14.16 | 0.11 | 0.43 | 5.16 | 2.31 | 435 | 0.24 |
| 90 | Narrow | $H_{98}$=1 | 0.75 | 675 | 0.64 | 0.90 | 17.57 | 0.11 | 0.29 | 5.21 | 2.93 | 342 | 0.37 |
| 90 | Narrow | $H_{ST}$=1 | 0.75 | 850 | 0.65 | 1.60 | 13.47 | 0.06 | 0.40 | 5.50 | 2.46 | 458 | 0.27 |

*Table 2: Parameters if selected fully non-inductive scenarios for NSTX-Upgrade. The $B_T$=1.0 T scenarios have six neutral beam sources, while the $B_T$=0.75 T scenarios have 4 sources.*

Additional features of these 100% non-inductive scenarios at $B_T$=1.0 and 0.75 T are given in table #2. The $B_T$=1.0 T cases all have $q_{min}$>1; however, some of the $B_T$=0.75 T scenarios can drop to $q_{min}$<1 for unfavorable profiles and the $H_{98}$ scaling assumptions.

Note that, as indicated by Fig. 9, the safety factor can be increased by slightly increasing the density.

The current redistribution times in these 100 % non-inductive scenarios vary from 0.25 to 0.83 seconds, depending on the field, heating power, confinement, and profiles. For the 100 kV acceleration cases with 1.5 sec heating pulse durations, the pulses are only 2-3 $\tau_{CR}$ long, and fully equilibrated profiles will likely not be achieved. On the other hand, for the 80 kV acceleration voltages, the pulse lengths are 7-15 $\tau_{CR}$ for $B_T$=1.0 T, and 12-19 $\tau_{CR}$ for $B_T$=0.75 T. Hence, these should allow the study of fully equilibrated 100% non-inductive scenarios.

We note that these scenarios all have pressure-drive currents dominant compared to neutral beam driven currents. This is largely a function of the desire to avoid NBCD overdrive on the magnetic axis driving down $q_{min}$. As a consequence, the values of $\beta_N$ and $\beta_P$ are comparatively high. However, as will be shown in Sect. 7, these $\beta_N$ values are not larger than presently achieved in NSTX. Furthermore, scenarios with $\beta_P$=2 have recently be sustained for long periods in NSTX [Gerhardt 2011b].

Note that additional 100% non-inductive scenarios will be illustrated in Sect. 6.5, in the context of modifying the current profile with various different combinations of neutral beams.

### *6.2 High-current partial inductive scenarios at $B_T$=1.0T and 0.75.*

While a steady-state plasma must be fully non-inductive, there are many physics studies facilitated by increasing the plasma current beyond the non-inductive level. These could include, for instance, studies of the collisionality dependence of core transport [Kaye 2007b, Guttenfelder 2011], or the current scaling of the divertor heat flux width [Gray 2010]. The centrally peaked relaxed inductive current tends to reduce $q_{min}$. Hence, it is instructive to consider what are the maximum current levels that can be sustained with $q_{min}$>1, as a function of beam voltage, toroidal field, and density. This is the purpose of the present section.

A solution to this optimization, for $B_T$=1.0 T, six neutral beam sources, a 15 cm outer gap, and Greenwald fraction 0.7<$f_{GW}$<0.75, is shown in Fig. 19 and table 3. For 80 kV acceleration voltage, the maximum sustainable current is between 1250 kA and 1800 kA; the larger number corresponds to the broader profiles and $H_{ST}$ thermal scaling, while the smaller number corresponds to the peaked profiles and $H_{98}$ thermal scaling. Central electron temperatures are between 1.7 and 2.3 keV. As indicted in Fig. 2, the neutral beams can provide heating for up to 5 seconds in this configuration.

The parameters are of these scenarios are significantly increased when the acceleration voltage is increased to 100 kV (black and green traces in Fig. 19). The projected currents increase to 1450-1975 kA, with peak electron temperatures of >2.5 keV for the ST confinement scaling and more peaked profiles.

Some additional parameters of these and related scenarios are given in Table 2. As with the fully non-inductive scenarios, the pulse durations for the 1.0 T, 100 kV cases are between 1.5 and 3 $\tau_{CR}$ in duration. This may be advantageous, as it will facilitate even higher current operation if the current profile cannot fully relax before the end of the beam pulse. The 80 kV cases have pulse durations of 6-12 $\tau_{CR}$ for $B_T$=1.0 T, and 11-14 $\tau_{CR}$ for $B_T$=0.75 T, and the requirement for scenarios with fully evolved $q_{min}$>1 is likely more strict.

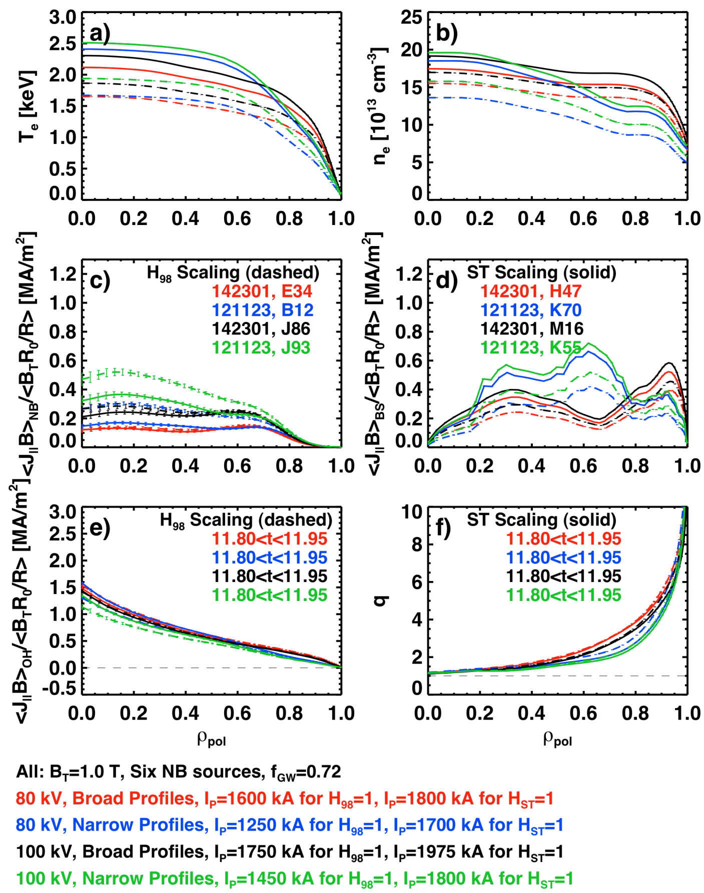


*Fig 19. Examples of the maximum sustainable current for various profile and confinement assumptions. Optimizations are shown for 80 kV and 100 kV acceleration voltages, with 6 neutral beam sources in each case.*

The bottom of table #2 also shows the results with 80 kV beams but a Greenwald fraction of 1.0. This increases the central safety factor for fixed $I_P$, or allows operation at higher current for fixed $q_{min}$. These cases allow 5 second operation at $I_P$=2 MA and $B_T$=1.0 T for favorable confinement and profiles. The fast ion pressure is at most 10% of the total pressure in these cases, compared to values of $W_{fast}/W_{tot}$ of ~20% in the $f_{GW}$=0.74 cases. Note that these very high density scenarios may be favorable for divertor power handling, though it remains unclear if there will be any degradation of confinement at the higher densities.

| Voltage [kV] | Profiles | Scaling | $B_T$ [T] | $I_p$ [kA] | $f_{GW}$ | $f_{BS}$ | $q_{95}$ | $\nu^*_{e,\rho=0.5}$ | $\tau_{CR}$ [s] | $\beta_N$ | $\beta_P$ | $W_{tot}$ [kJ] | $W_{fast}/W_{tot}$ |
|---|---|---|---|---|---|---|---|---|---|---|---|---|---|
| 80 | Broad | H98=1 | 1 | 1600.4 | 0.74 | 0.39 | 8.43 | 0.08 | 0.55 | 3.82 | 1.22 | 796 | 0.09 |
| 80 | Broad | HST=1 | 1 | 1800 | 0.73 | 0.47 | 7.82 | 0.06 | 0.79 | 4.76 | 1.36 | 1118 | 0.07 |
| 80 | Narrow | H98=1 | 1 | 1250 | 0.73 | 0.40 | 8.88 | 0.06 | 0.44 | 3.82 | 1.41 | 598 | 0.17 |
| 80 | Narrow | HST=1 | 1 | 1700.2 | 0.74 | 0.49 | 7.92 | 0.03 | 0.80 | 4.93 | 1.51 | 1092 | 0.08 |
| 90 | Broad | $H_{98}$=1 | 1 | 1700 | 0.74 | 0.40 | 7.89 | 0.07 | 0.62 | 4.25 | 1.26 | 937 | 0.10 |
| 90 | Broad | $H_{ST}$=1 | 1 | 1900 | 0.73 | 0.47 | 7.43 | 0.05 | 0.85 | 5.11 | 1.38 | 1267 | 0.08 |
| 90 | Narrow | $H_{98}$=1 | 1 | 1350 | 0.73 | 0.42 | 8.48 | 0.05 | 0.50 | 4.26 | 1.48 | 723 | 0.17 |
| 90 | Narrow | $H_{ST}$=1 | 1 | 1750.3 | 0.74 | 0.50 | 7.71 | 0.03 | 0.83 | 5.22 | 1.55 | 1190 | 0.10 |
| 100 | Broad | $H_{98}$=1 | 1 | 1750 | 0.74 | 0.42 | 7.92 | 0.06 | 0.66 | 4.58 | 1.34 | 1044 | 0.12 |
| 100 | Broad | $H_{ST}$=1 | 1 | 1975 | 0.73 | 0.48 | 7.19 | 0.05 | 0.90 | 5.45 | 1.42 | 1406 | 0.09 |
| 100 | Narrow | $H_{98}$=1 | 1 | 1450 | 0.73 | 0.43 | 8.12 | 0.04 | 0.56 | 4.71 | 1.54 | 865 | 0.18 |
| 100 | Narrow | $H_{ST}$=1 | 1 | 1800 | 0.74 | 0.50 | 7.52 | 0.03 | 0.86 | 5.55 | 1.60 | 1304 | 0.12 |
| 80 | Broad | $H_{98}$=1 | 0.75 | 1250 | 0.74 | 0.39 | 8.02 | 0.09 | 0.39 | 4.10 | 1.24 | 498 | 0.11 |
| 80 | Broad | $H_{ST}$=1 | 0.75 | 1300 | 0.74 | 0.40 | 7.84 | 0.08 | 0.43 | 4.32 | 1.27 | 547 | 0.10 |
| 80 | Narrow | $H_{98}$=1 | 0.75 | 1025 | 0.73 | 0.39 | 8.22 | 0.06 | 0.34 | 4.21 | 1.44 | 406 | 0.19 |
| 80 | Narrow | $H_{ST}$=1 | 0.75 | 1125 | 0.73 | 0.44 | 8.07 | 0.05 | 0.43 | 4.70 | 1.52 | 505 | 0.15 |
| 90 | Broad | $H_{98}$=1 | 0.75 | 1300 | 0.74 | 0.40 | 7.95 | 0.08 | 0.43 | 4.46 | 1.32 | 566 | 0.12 |
| 90 | Broad | $H_{ST}$=1 | 0.75 | 1350 | 0.74 | 0.42 | 7.70 | 0.07 | 0.47 | 4.69 | 1.33 | 619 | 0.11 |
| 90 | Narrow | $H_{98}$=1 | 0.75 | 1125 | 0.75 | 0.42 | 8.97 | 0.05 | 0.38 | 4.55 | 1.59 | 500 | 0.18 |
| 90 | Narrow | $H_{ST}$=1 | 0.75 | 1250 | 0.75 | 0.44 | 8.07 | 0.04 | 0.46 | 4.91 | 1.54 | 600 | 0.15 |
| 80 | Broad | $H_{98}$=1 | 1 | 1850 | 1.05 | 0.41 | 7.29 | 0.16 | 0.46 | 4.49 | 1.23 | 1079 | 0.03 |
| 80 | Broad | $H_{ST}$=1 | 1 | 2000 | 1.03 | 0.49 | 7.12 | 0.12 | 0.61 | 5.41 | 1.39 | 1417 | 0.03 |
| 80 | Narrow | $H_{98}$=1 | 1 | 1450 | 1.03 | 0.42 | 7.62 | 0.10 | 0.39 | 4.17 | 1.32 | 757 | 0.07 |
| 80 | Narrow | $H_{ST}$=1 | 1 | 1900 | 1.04 | 0.49 | 6.66 | 0.06 | 0.63 | 5.49 | 1.44 | 1344 | 0.04 |
| 80 | Broad | $H_{98}$=1 | 0.75 | 1425 | 1.05 | 0.41 | 7.19 | 0.20 | 0.32 | 4.67 | 1.26 | 650 | 0.04 |
| 80 | Broad | $H_{ST}$=1 | 0.75 | 1425 | 1.05 | 0.43 | 7.32 | 0.19 | 0.33 | 4.84 | 1.31 | 675 | 0.04 |
| 80 | Narrow | $H_{98}$=1 | 0.75 | 1150 | 1.04 | 0.43 | 7.71 | 0.11 | 0.29 | 4.60 | 1.44 | 504 | 0.09 |
| 80 | Narrow | $H_{ST}$=1 | 0.75 | 1250 | 1.04 | 0.46 | 7.37 | 0.09 | 0.34 | 5.01 | 1.47 | 602 | 0.07 |

*Table #3: Parameters if selected fully non-inductive scenarios for NSTX-Upgrade. The $B_T$=1.0 T scenarios have six neutral beam sources, while the $B_T$=0.75 T scenarios have 4 sources.*

### *6.3 Partially Inductive Sustained Long Pulse at $B_T$=0.75 T and Reduced Current.*

Many studies will be interested in testing the behavior of the longest possible discharges, even if this requires a reduction in the plasma current. These include, for instance, particle retention studies or the study of RWM control and high-β disruption avoidance for the longest possible duration. In this section, we present scenarios that may allow a single discharge to be sustained for 8-10 seconds. The toroidal field strength for these cases is $B_T$=0.75 T, such that the heating limit of the TF coil is not exceeded for pulses of the target duration.

We will study two different beam configurations to facilitate this very long pulse goal. The first utilizes at 80 kV for each source, modulated so that only three are on at any given time. With a five second duration for any single source and a duty cycle of 50%, we can sustain the configuration for a full 10 seconds. A second configuration uses all 6 sources configured for 65 kV operation, allowing an 8 second heating pulse.

The current and heating limit of the Ohmic solenoid coil play a key role in determining this optimization. In order to assess this, we have estimated the solenoid current evolution as follows. The ramp-up times, ramp-up flux, and ramp-down times, all as a function of flat-top plasma current, are given in table 1 of Ref. [Menard 2012]. The flat-top surface voltage, and hence rate of solenoid current change, is taken from the TRANSP simulations. A voltage of -0.5 V is assumed for the ramp-down. These parameters are sufficient to form a simple solenoid current waveform. The resulting solenoid current evolution can be compared to the maximum allowed current, and the $\int I_{OH}^2 dt$ can be compared to the limit on that quantity set by coil heating.

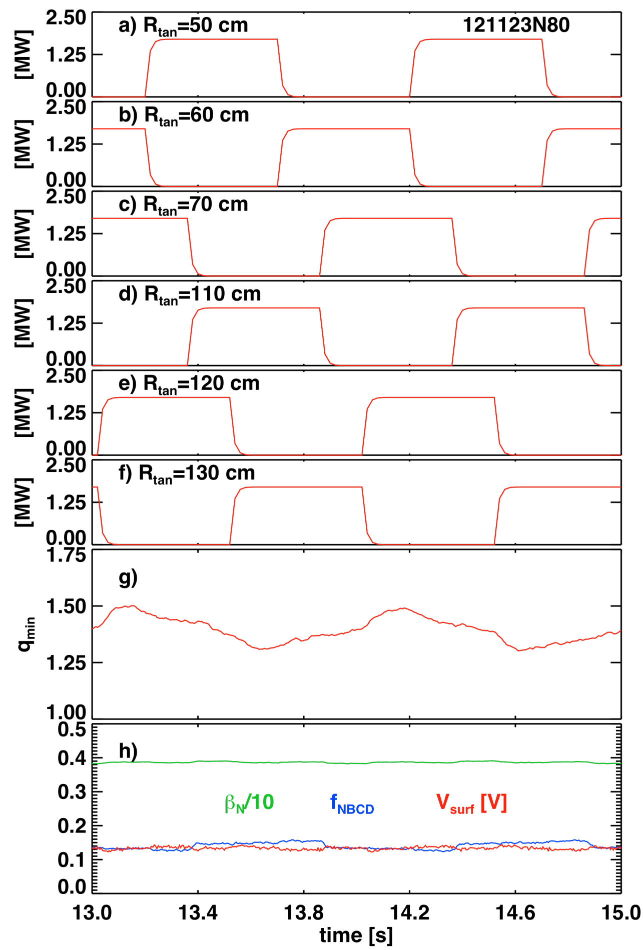


Fig. 20: Effect of neutral beam modulations on the fully evolved scenario. Shown are the neutral beam powers in frames a)-f), the minimum safety factor ($q_{min}$) in frame g), and the normalized beta ($\beta_N$), beam current drive fraction ($f_{NBCD}$) and surface voltage ($V_{surf}$) in frame h).

As noted above, one long-pulse scenario uses 80 kV acceleration voltages with a 50% duty cycle, for a total duration of the heating pulse of 10 seconds. We also wish to reduce the total number of modulations to 20 [Gerhardt 2012b]. The key question to answer is whether this modulation will produce unacceptable modulations in the central safety factor and other parameters. An example calculation is shown in Fig. 20. Frames a)-f) show the neutral beam power. Each source if modulated with 0.5 seconds on followed by 0.5 seconds off, staggered such that the total input power is constant at 5.1 MW. The evolution of the central safety factor is illustrated in frame g), and shows a modulation of about 0.15 units. The normalized $\beta_N$ is nearly constant, reflecting that modulations in the total pressure due to the different beam geometries is quite small. The modulations in the surface voltage are also quite negligible. The beam current drive fraction does show some modulation, mainly due to the oscillation between the $R_{tan}$=70 cm and $R_{tan}$=110 beams, which have significantly different current drive efficiencies [Menard 2012].

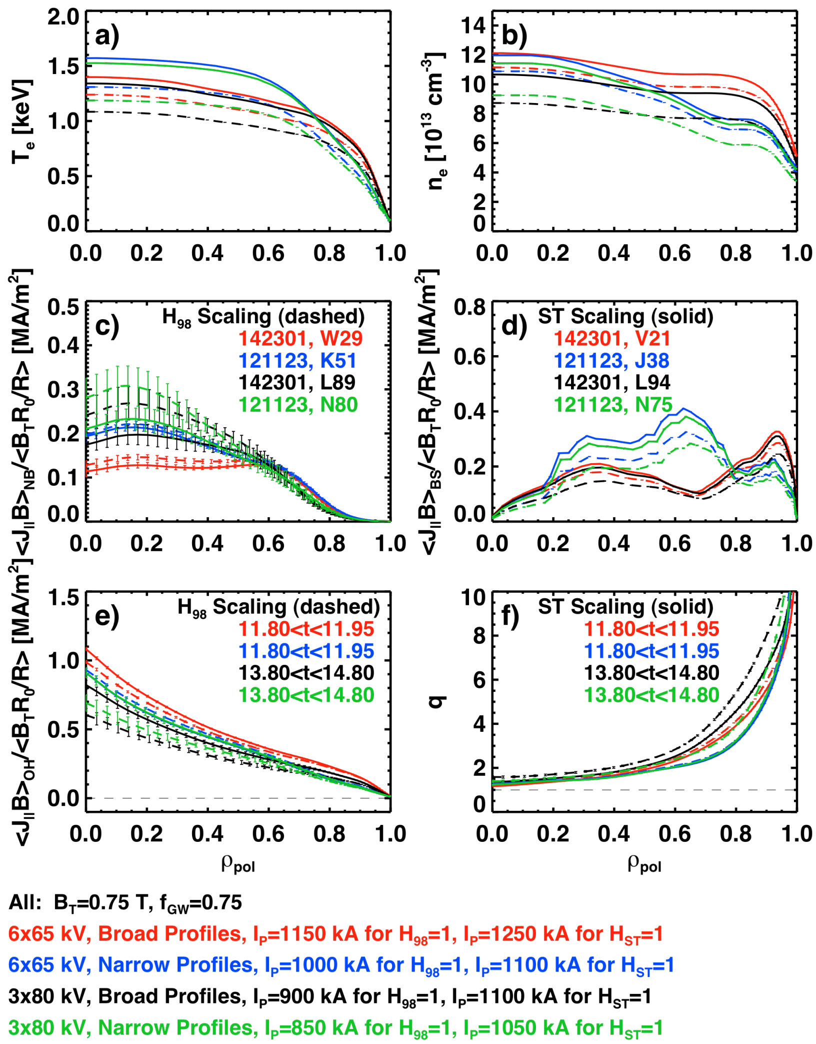


*Fig 21: Example profiles for configurations optimized for very long pulse. The plasma current level varies among the different configurations, which all have 0.7<$f_{GW}$<0.75.*

With this background, the profiles which provide 8-10 second operation are shown in Fig. 21, and the model solenoid current waveforms are shown in Fig. 22. The color scheme and linetypes are the same in the two figures. Again, the different profile and confinement assumptions are tested; these result in various levels of plasma current pending the assumptions.

For the modulated 80 kV scenarios in green and blue with 5.1 MW of injected power, the level of plasma current varies between 850 kA and 1100 kA. As before, the highest allowed level is for the broad thermal profiles and ST scaling, and the lowest level is for the more peaked thermal profiles and $H_{98}$ scaling. These cases generally have somewhat elevated $q_{min}$. This is because the $\int I_{OH}^2 dt$ limit on the solenoid generally constrains the maximum plasma current for scenarios designed for sustainment up to 10 seconds. This is most easily seen in the green and black curves of Fig 22b, where there is a rapid increase in $\int I_{OH}^2 dt$ toward the end of the pulse. The plasma current can generally be increased by 50-100 kA while maintaining $1.1<q_{min}<1.2$, but the solenoid coil heating limit is invariably exceeded before the full 10 second heating phase.

For the 65 kV acceleration voltage scenarios in red and blue (corresponding the broad and peaked thermal profile), the total input power is 6.6 MW, sustainable for up to 8 seconds. This results in sustainable current levels between $I_P$=1000 kA for narrow profiles and $H_{98}$=1 and $I_P$ =1250 A for broader profiles and $H_{ST}$=1. The Ohmic heating of the solenoid coil is not generally a constraint in these cases. Rather, the maximum current is set by the requirement to operate with $q_{min}$>1.

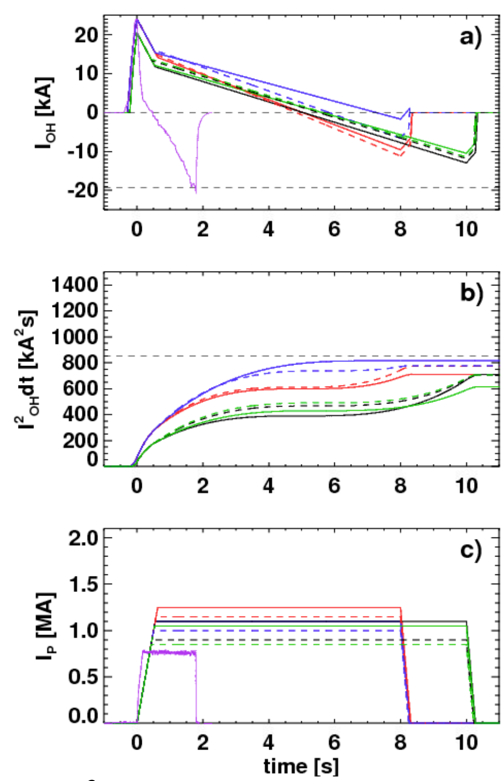


*Fig 22: a) Model solenoid current, b) $\int I_{OH}^2 dt$, and c) plasma current evolution for the scenarios in Fig. 21. Also shown in frame a) and c) are the solenoid and plasma currents for NSTX discharge 129125.*

Fig. 22 also shows the solenoid and plasma current traces for discharge 129125 [Menard 2010, Gerhardt 2011b]. This $I_P$=750 kA discharge has the longest $I_P$ flat-top duration ever achieved in NSTX. The performance of the projected NSTX-Upgrade very long pulse plasmas is 10-60% better in terms of plasma current level, and 4.5-5.5 times better in terms of pulse duration.

We also note that these simulations were done assuming that the ion thermal transport remained at the neoclassical level. The discussions in Sect. 5.4 demonstrate that at long as the overall confinement level is maintained, increasing the ion thermal transport can be beneficial. If this were to occur for the scenarios listed here, it would reduce the required induction, potentially allowing higher currents for these pulse durations.

Additional parameters for these scenarios are given in Table 3. The key observation is that the pulse lengths are between 18 and 34 $\tau_{CR}$ in duration, all with $\beta_N$ above the no-wall limit.

| Beam Config. | Profiles | Scaling | $I_p$ [kA] | $f_{NICD}$ | $f_{BS}$ | $\tau_{CR}$ [s] | $\beta_N$ | $\beta_P$ | $q_{min}$ | $q_{95}$ | $V_{surf}$ [V] | $W_{tot}$ [kJ] |
|---|---|---|---|---|---|---|---|---|---|---|---|---|
| Six 65 kV | Broad | H98=1 | 1150 | 0.54 | 0.40 | 0.36 | 3.91 | 1.31 | 1.25 | 8.97 | 0.18 | 439 |
| Six 65 kV | Broad | HST=1 | 1250 | 0.56 | 0.42 | 0.43 | 4.29 | 1.32 | 1.16 | 8.31 | 0.16 | 524 |
| Six 65 kV | Narrow | H98=1 | 1000 | 0.60 | 0.42 | 0.33 | 4.05 | 1.59 | 1.24 | 10.08 | 0.15 | 396 |
| Six 65 kV | Narrow | HST=1 | 1100 | 0.66 | 0.48 | 0.43 | 4.63 | 1.64 | 1.27 | 9.23 | 0.12 | 498 |
| 3 Staggered 80 kV | Broad | $H_{98}$=1 | 900 | 0.61 | 0.45 | 0.30 | 3.61 | 1.54 | 1.58 | 11.70 | 0.13 | 317 |
| 3 Staggered 80 kV | Broad | $H_{ST}$=1 | 1100 | 0.60 | 0.46 | 0.41 | 4.13 | 1.44 | 1.37 | 9.57 | 0.13 | 444 |
| 3 Staggered 80 kV | Narrow | $H_{98}$=1 | 850 | 0.63 | 0.44 | 0.29 | 3.87 | 1.77 | 1.39 | 11.93 | 0.13 | 321 |
| 3 Staggered 80 kV | Narrow | $H_{ST}$=1 | 1050 | 0.64 | 0.47 | 0.41 | 4.41 | 1.64 | 1.23 | 9.62 | 0.12 | 452 |

*Table #4: Parameters of scenarios optimized for very long pulses.*

### *6.4 Sustained highest toroidal β.*

It is desirable to operate a fusion system at the highest possible value of $\beta_T$, since the fusion power scales as $\beta_T^2 B^4$ [Stambaugh 1997]. The requirements for operating a tokamak or ST at high toroidal $\beta$ have been clearly articulated in previous research. The key step is to operate at high normalized current $I_N=I_P/aB_T$, since Troyon scaling [Troyon 1984, Strait 1994] implies $\beta_T=I_N\beta_N$. The normalized current cannot, however, be made arbitrarily large, as this would result in the edge safety factor becoming too low; a cylindrical safety factor $q^* = \dfrac{\varepsilon\pi a B_T\left(1+\kappa^2\right)}{\mu_0 I_P}$ less than ~1.8 has been shown to be a good boundary for the resulting external kink [Menard 2004]. Given that q* and $I_N$ are related as $q^* = \dfrac{\varepsilon\pi\left(1+\kappa^2\right)}{\mu_0 I_N}$, it is clear that increasing $I_N$ at fixed q* requires that either the elongation must be increased, or the aspect ratio decreased.

However, while these steps may facilitate the achievement of transient very high-$\beta_T$, the configuration may not be sustainable. As discussed above, an additional requirement is that the fully evolved current profile yield $q_{min}$>1 [Menard 2005, Menard 2006, Gerhardt 2011, Gerhardt 2012, Breslau 2011, Chapman 2010]. For the present device, this condition implies that the density of the centrally-peaked Ohmic current not become too large, and that the NBCD be configured to drive current off-axis. To this end, a study to optimize $\beta_T$ using a 0.55 T toroidal field has been completed. This value of toroidal field was chosen because it overlaps with the largest value ever routinely run in NSTX, albeit with flat-top durations of < 1 second. The TF flat-top duration at this field in NSTX-Upgrade is significantly longer than the longest conceivable plasma discharge given other facility limitation.

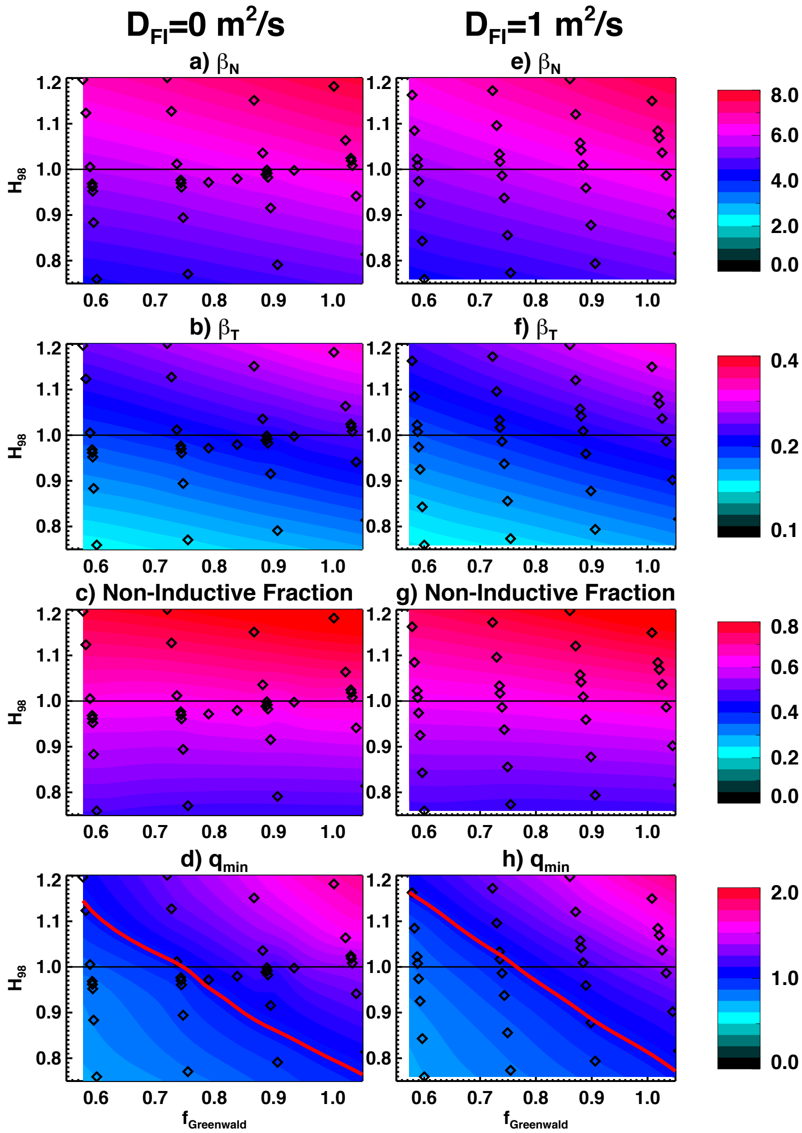


*Fig. 23: Contours of $\beta_N$, $\beta_T$, the non-inductive fraction, and $q_{min}$ vs. the confinement factor $H_{98}$ and Greenwald fraction. These configurations have $I_P$=1200 kA, $B_T$=0.55 T with $R_{tan}$=[50,60,120,130], 90 kV beams and a target boundary shape with A=1.81 and κ=2.95. The left column has $D_{FI}$=0 $m^2$/s, while the right column has $D_{FI}$=1$m^2$/s. The $q_{min}$=1 contour is illustrated in the bottom row.*

As will be seen below, these scenarios have some significant differences from the 100% non-inductive scenarios discussed above. For instance, the neutral beam current drive profile tends to become hollow, and the plasma elongation is quite high. As a consequence, 6.4a will revisit some issues of current profile optimization and MHD stability for these scenarios. Section 6.4b will then show the results of this optimization for the various profile and confinement assumptions.

### *6.4.a: Parameters the high-$\beta_T$ optimization*

Many parametric dependencies of the high-$\beta_T$ optimization were studied as part of the S3 scenario in section 5. This scenario has 1200 kA of plasma current and a toroidal field of 0.5 T, four sources with 90 kV injection energy, capable of injecting 2.1 MW per source for up to 3 seconds. We utilize the 20cm outer gap shape illustrated in Sect. 5, and the four beam sources are the $R_{tan}$=[50,60,120,130] sources; both of these choices elevate $q_{min}$ as much as possible, the latter by driving a hollow NB current drive profile. The results of Sect 5, also shows that this scenario was largely insensitive to choices of $D_{FI}$, the ion thermal confinement, and $Z_{eff}$, provided that a given confinement multiplier ($H_{98y}$=1, for instance) is maintained.

The left-hand column of Fig. 23 shows additional calculations of plasmas fitting this scenario, where various parameters are again plotted in the space of $H_{98}$ and $f_{GW}$. It is clear that this optimizations can produce quite high-values of $\beta_N$, with values of ~6 anticipated at the higher Greenwald fraction with $H_{98}$=1. These correspond to values of $\beta_T$ in the range of 25%. The non-inductive fraction is again largely independent of the density, and is in the range of ~50-60% for these cases. Most importantly, the minimum safety factor in frame 18d) tends to drop beneath 1 for densities below $f_{GW}$=0.8 (again, at $H_{98}$=1).

The right-hand column shows the same data, but for a fast ion diffusivity of 1 $m^2$/s. Recall that this value represents the maximum value compatible with measurements in MHD-quiescent discharges in NSTX [Gerhardt 2011a]. The non-inductive current fraction, βs, and $q_{min}$ are largely unchanged by this value of $D_{FI}$ over the full range of confinement and density.

The global stability parameters for these scenarios are shown in Fig. 24, for the same calculations as in Fig. 23; see discussion of Fig. 12 for a detailed description of the stability parameter. The left hand column corresponds to a case with purely classical beam physics, while the right column has an imposed $D_{FI}$=1 $m^2$/s. The pressure peaking in these scenarios is substantially lower than the six-source 1 MA, 1T scenario in Fig. 12, for two reasons: i) the thermal pressure, which has a broad profile in H-mode, is a larger fraction of the total pressure, and ii) the fast ion pressure in more broad than in Fig. 12, due to the dominantly off-axis injection. Furthermore, the total pressure peaking is not particularly impacted by the fast ion diffusion, for the same two reasons.

As a consequence, the stability maps are not significantly different between these two cases. As is shown in the no-wall δW calculation in the third row, a large fraction of confinement vs. density space is precluded by $q_{min}$ being close to or less than unity. All the other operating points are unstable without a wall. The inclusion of a wall in the lower row opens up a significant operating space at $H_{98}$=1, and it is this operating space that is of interest for scenario development.

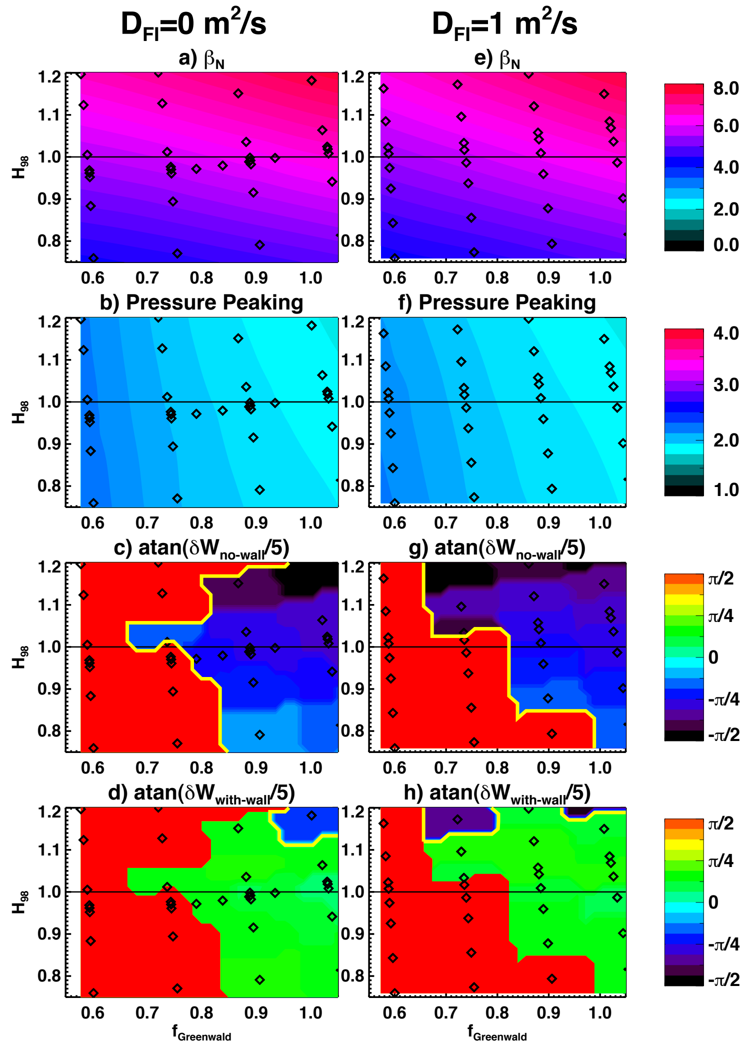


*Fig 24: Ideal stability parameters for configurations in Fig. 23. See text for further details.*

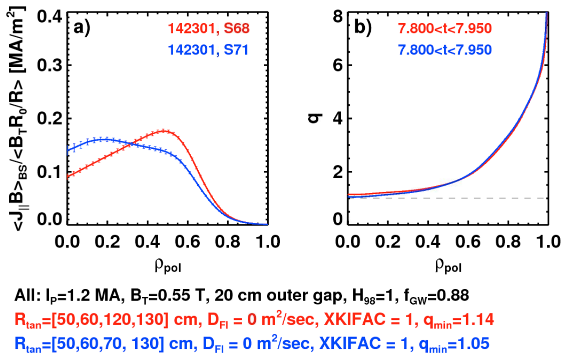


*Fig. 25: Test of two difference neutral beam source combinations for maintaining elevated $q_{min}$ in the high-$\beta_T$ scenario optimization*

The beam tangency radii of 50, 60, 120 & 130 cm in these cases were chosen to increase the provide substantial heating while eliminating the central current drive. One might think, however, that the $R_{tan}$=70 source might be a better choice than the $R_{tan}$=120 beam, given that the $R_{tan}$=120 cm does tend to have strong centralized current drive. That this is not true is shown in Fig. 25. Using the $R_{tan}$=70 sources tends to increase the central NBCD, lower the safety factor profile, and reduce the bootstrap current. The net result is to decrease the central safety factor by ~0.1 units, which would have a deleterious effect on the configuration.

*6.4.b: Scenarios that maximize $\beta_T$ with $q_{min}$>1.*

With these results in mind, we have determined the maximum levels of current that allow $q_{min}$>1 operation for the $R_{tan}$=[50,60,120,130] cm neutral beam configuration at $B_T$=0.55 T, knowing that this optimization will maximize $\beta_T$. This optimization was done for both 90 and 100 kV acceleration voltages, for different profile shapes and thermal confinement scalings. The Greenwald fraction was fixed at 0.7 for all cases. The results of this optimization are shown in Fig. 26, and additional parameters are given in Table #5.

For the 90 kV acceleration voltage cases (capable of producing up to 3 second long heating pulses), the $\beta_T$ values range from 18 to 22%, with corresponding plasma currents ranging between 900 and 1100 kA. The non-inductive fraction ranges between 65 and 75% for these scenarios. For the 100 kV acceleration voltage cases (capable of producing up to 1.5 second long heating pulses), the $\beta_T$ values range from 20 to 27%, with corresponding plasma currents ranging between 925 and 1200 kA. The non-inductive fraction in these cases ranges between 62 and 82%. None of these scenarios challenge the current limit on the OH coil for the allowed pulse duration.

There are a few other features to note about these scenarios. The central beam current drive is always higher with the peaked profiles, due to the higher central electron temperature and lower edge density; this is similar to the results with other optimizations. Unlike previous optimizations, the higher temperatures are projected using the ITER-98 confinement scaling expression. The strong $B_T$ dependence in the ST scaling expression results in a significant confinement enhancement at stronger toroidal field. These scenarios, with lower $B_T$ of 0.55 T, cannot take advantage of that dependence.

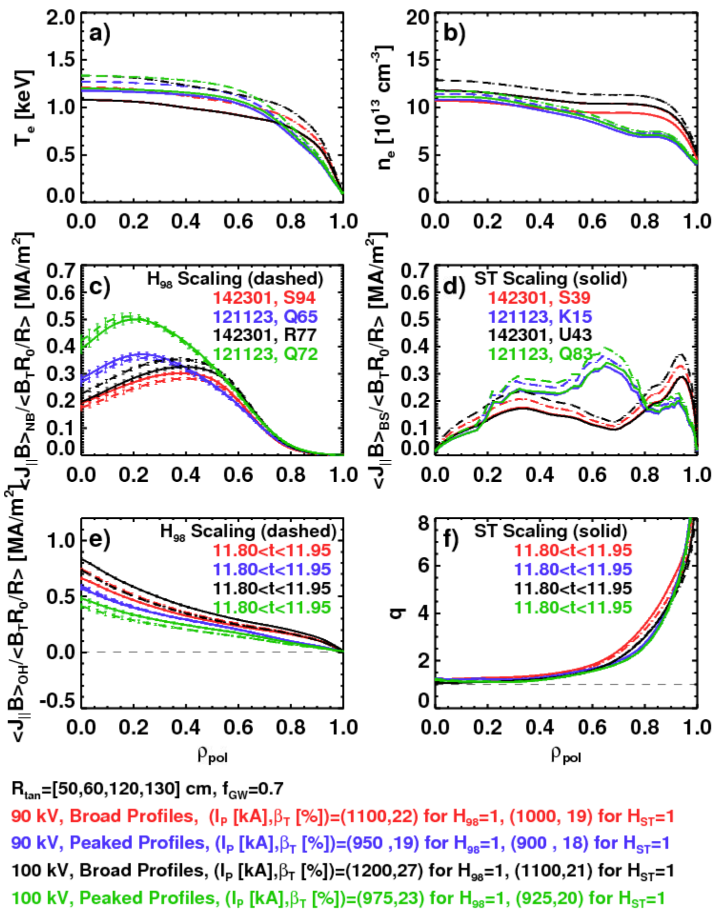


*Fig. 26: Profiles for a range of scenarios designed to maximize the sustainable $\beta_T$.*

Additional parameters of these scenarios are given in Table 5. The pulses are ~10 $\tau_{CR}$ in duration for 90 kV and ~6$\tau_{CR}$ for 100 kV cases. The current profile should thus be fully equilibrated. The values of $\beta_N$ are the highest discussed in this paper, as is fitting for scenarios designed to challenge MHD stability physics and control. This high value of $\beta_N$, combined with the large value of $I_P/B_T$, results in the large values of $\beta_T$.

| Voltage [kV] | Profiles | Scaling | $B_T$ [T] | $I_p$ [kA] | $f_{NICD}$ | $q_{95}$ | q* | $\tau_{CR}$ [s] | $\beta_N$ | $\beta_T$ | $\beta_P$ | $W_{tot}$ [kJ] | $W_{fast}/W_{tot}$ |
|---|---|---|---|---|---|---|---|---|---|---|---|---|---|
| 90 | Broad | H98=1 | 0.55 | 1100 | 0.66 | 6.99 | 3.36 | 0.32 | 5.65 | 0.22 | 1.51 | 438 | 0.14 |
| 90 | Broad | HST=1 | 0.55 | 1000 | 0.66 | 7.66 | 3.71 | 0.27 | 5.23 | 0.19 | 1.53 | 368 | 0.17 |
| 90 | Narrow | H98=1 | 0.55 | 950 | 0.75 | 7.96 | 4.15 | 0.29 | 5.91 | 0.20 | 1.86 | 397 | 0.21 |
| 90 | Narrow | HST=1 | 0.55 | 900 | 0.73 | 8.39 | 4.40 | 0.26 | 5.64 | 0.18 | 1.89 | 359 | 0.23 |
| 100 | Broad | $H_{98}$=1 | 0.55 | 1200 | 0.71 | 6.45 | 3.07 | 0.37 | 6.32 | 0.27 | 1.54 | 535 | 0.15 |
| 100 | Broad | $H_{ST}$=1 | 0.55 | 1075 | 0.64 | 6.96 | 3.43 | 0.27 | 5.43 | 0.21 | 1.46 | 409 | 0.18 |
| 100 | Narrow | $H_{98}$=1 | 0.55 | 975 | 0.83 | 7.90 | 3.95 | 0.31 | 6.57 | 0.23 | 1.99 | 452 | 0.23 |
| 100 | Narrow | $H_{ST}$=1 | 0.55 | 925 | 0.78 | 8.22 | 4.22 | 0.27 | 6.09 | 0.20 | 1.96 | 398 | 0.25 |

*Table #5: Parameters of very high $\beta_T$ discharges at $B_T$=0.55 T and elongation of ~2.9.*

## *6.5 Current profile control using different NB combinations.*

An underlying concept in the above sections has been the selection of shapes, densities, and beam configurations that achieve some given scenario goal with $q_{min}$>1. In this section, we evaluate the prospects for current profile control at fixed shape and plasma density, using varying combinations of neutral beam sources.

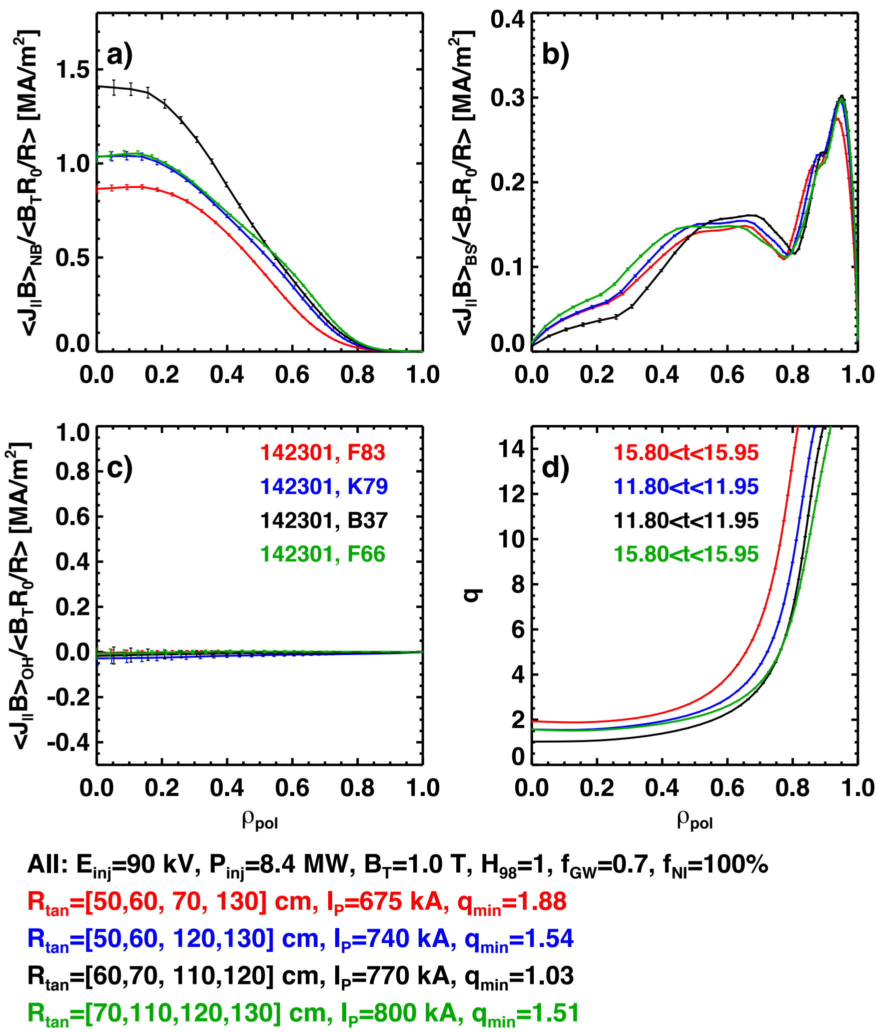


*Fig. 27: Variation of the safety factor profile with various beam tangency radii, for 100 % non-inductive scenarios at $B_T$=1.0 T. The plasma current is allowed to vary in order to maintain the non-inductive state.*

An important detail in this study is deciding what should be held fixed. The plasma current can be held fixed allowing the non-inductive current fraction to vary with different beam combinations. Alternatively, the loop voltage can be set to zero, allowing the plasma current to vary. Both contingencies are addressed below. Note that these studies will utilize the broad thermal profiles from 142301 and ITER-98 scaling on the thermal energy, in order to focus on the effects of the various beam configurations on the current profile.

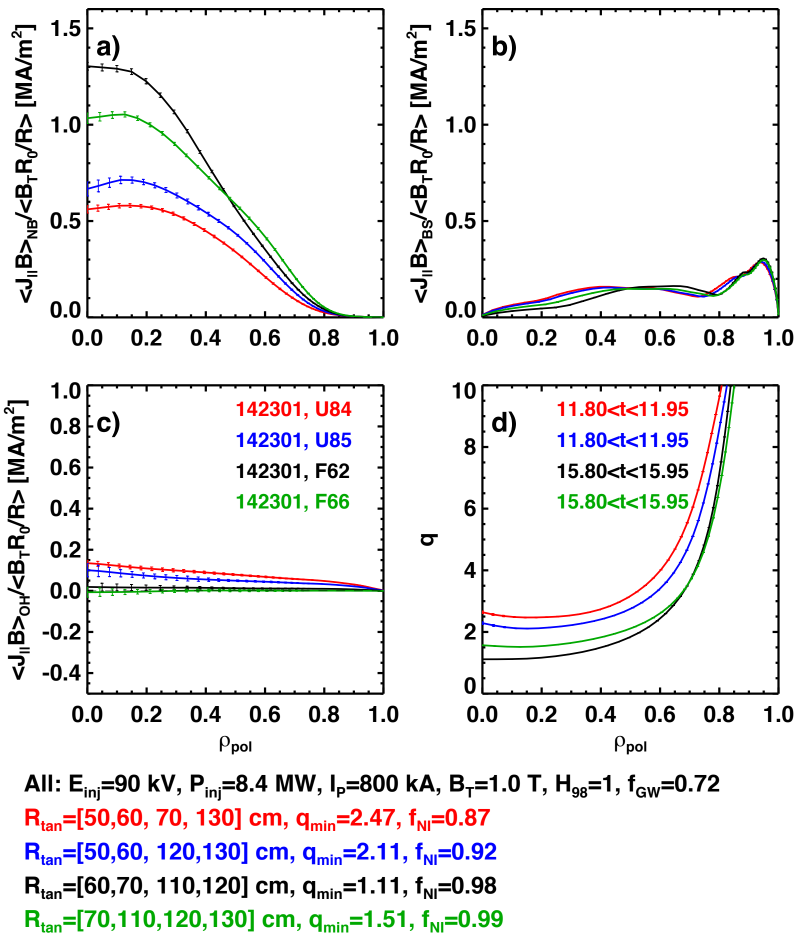


*Fig. 28: Variation of the safety factor profile with various beam tangency radii, for 800 kA scenarios at $B_T$=1.0 T. The non-inductive current fraction varies from 83% to 97%.*

Fig. 27 shows the results of such a study for $B_T$=1.0 T and $f_{NI}$=100%; the plasma current as allowed to vary. The central safety factor is largest, and the plasma current smallest, with tangency radii of [50,60,70,130]; this configuration has eliminated the $R_{tan}$=110 & 120 cm beams, which have the highest current drive efficiency but also tend to drive current on the magnetic axis. The highest non-inductive plasma currents come from the $R_{tan}$=[70,110,120,130] combination, which utilizes the four beams with the best current drive efficiency to produce $q_{min}$=1.57. The lowest values of $q_{min}$ are achieved with the $R_{tan}$=[60,70,110,120] configuration, with the minimum safety factor falling just under unity.

Fig. 28 shows the results of a similar scan, where the plasma current is held fixed at 800 kA. In this case, the $R_{tan}$=[70,110,120,130] is fully non-inductive with $q_{min}$=1.5. On the other hand, the $R_{tan}$=[50,60,70,130] scenario has a non-inductive fraction of only 87%, but a central safety factor of almost 2.5. The $R_{tan}$=[60,70,110,120] has the lowest minimum safety factor, with $q_{min}$=1.1 in a near non-inductive state. We note that the calculations in Figs. 27 & 28 were done with neoclassical fast ion physics only. The inclusion of some additional anomalous fast ion diffusivity would likely reduce the difference in $q_{min}$ between these scenarios.

The parameters of these scenarios, and similar scenarios at $B_T$=0.75 T, are shown in Table 6. Given the 3 second pulse duration for 90 kV beams, these scenarios are typically 8.5-10 $\tau_{CR}$ in duration. Hence, it is anticipated that the current profile will be able to fully respond in response to variations in the beam configuration during the shot, and feedback control of the $q_{min}$ in this way should be possible.

| $R_{tan}$ [cm] | Profiles | Scaling | $B_T$ [T] | $I_p$ [kA] | $f_{NICD}$ | $f_{NBCD}$ | $\tau_{CR}$ [s] | $\beta_N$ | $\beta_P$ | $q_{95}$ | $q_0$ | $q_{min}$ |
|---|---|---|---|---|---|---|---|---|---|---|---|---|
| [50,60,70,130] | Broad | H98=1 | 1 | 675 | 1.00 | 0.27 | 0.32 | 3.45 | 2.64 | 25.19 | 1.93 | 1.88 |
| [50,60,120,130] | Broad | HST=1 | 1 | 740 | 1.00 | 0.30 | 0.35 | 3.70 | 2.57 | 22.39 | 1.57 | 1.55 |
| [60,70,110,120] | Narrow | H98=1 | 1 | 770 | 1.00 | 0.31 | 0.36 | 3.81 | 2.53 | 21.10 | 1.00 | 1.00 |
| [70,110,120,130] | Narrow | HST=1 | 1 | 800 | 1.00 | 0.35 | 0.36 | 3.76 | 2.40 | 19.78 | 1.57 | 1.51 |
| [50,60,70,130] | Broad | $H_{98}$=1 | 1 | 800 | 0.87 | 0.24 | 0.35 | 3.46 | 2.23 | 19.87 | 2.64 | 2.47 |
| [50,60,120,130] | Broad | $H_{ST}$=1 | 1 | 800 | 0.92 | 0.28 | 0.35 | 3.56 | 2.28 | 19.75 | 2.29 | 2.11 |
| [60,70,110,120] | Narrow | $H_{98}$=1 | 1 | 800 | 0.98 | 0.29 | 0.37 | 3.78 | 2.41 | 19.86 | 1.11 | 1.11 |
| [70,110,120,130] | Narrow | $H_{ST}$=1 | 1 | 800 | 1.00 | 0.35 | 0.36 | 3.76 | 2.40 | 19.78 | 1.57 | 1.51 |
| [50,60,70,130] | Broad | $H_{98}$=1 | 0.75 | 650 | 1.00 | 0.26 | 0.29 | 4.46 | 2.65 | 19.62 | 1.27 | 1.23 |
| [50,60,120,130] | Broad | $H_{ST}$=1 | 0.75 | 725 | 1.00 | 0.30 | 0.32 | 4.68 | 2.48 | 16.74 | 1.12 | 1.10 |
| [60,70,110,120] | Narrow | $H_{98}$=1 | 0.75 | 765 | 1.00 | 0.30 | 0.34 | 4.85 | 2.42 | 15.49 | 0.68 | 0.68 |
| [70,110,120,130] | Narrow | $H_{ST}$=1 | 0.75 | 775 | 1.00 | 0.34 | 0.33 | 4.85 | 2.39 | 15.16 | 0.94 | 0.93 |
| [50,60,70,130] | Broad | $H_{98}$=1 | 0.75 | 800 | 0.85 | 0.23 | 0.33 | 4.44 | 2.14 | 14.55 | 1.93 | 1.77 |
| [50,60,120,130] | Broad | $H_{ST}$=1 | 0.75 | 800 | 0.89 | 0.27 | 0.33 | 4.57 | 2.19 | 14.52 | 1.56 | 1.46 |
| [60,70,110,120] | Narrow | $H_{98}$=1 | 0.75 | 800 | 0.93 | 0.28 | 0.34 | 4.75 | 2.26 | 14.44 | 0.79 | 0.79 |
| [70,110,120,130] | Narrow | $H_{ST}$=1 | 0.75 | 800 | 0.99 | 0.33 | 0.34 | 4.87 | 2.33 | 14.61 | 1.04 | 1.00 |

*Table #6: Parameters of discharges designed to vary the q-profile using different NB injection geometry.*

## 7: Comparison of scenarios to the existing NSTX database.

The scenarios discussed above represent a significant increase in device capabilities compared to the present NSTX. This increment is best illustrated by comparing the parameters of these scenarios to those already achieve in NSTX. This is facilitated by an already existing database of TRANSP analysis of high-performance discharges in NSTX, covering the 2008-2010 run campaign [Gerhardt 2011b]. The data from that database are shown in Fig. 29 to 33 as discreet points, with the cyan points corresponding to A>1.65 discharges designed to study higher aspect ratio plasmas [Gerhardt 2011b]. Note that while the thermal energy content was approximately constant during the time window when these experimental points were taken, the current profile was often slowly evolving to $q_{min}$<1 and eventual disruption.

The colored shapes in each of Fig. 27-29 correspond to a particular scenario for NSTX-Upgrade. The neutral beam configuration, Greenwald fraction, toroidal field, and target plasma boundary are the same for all points on a given shape, but the plasma current may vary. The four corners correspond to the two profiles shape assumptions and two confinement assumptions. Hence, each of these shapes shows the range of operating points possible for a given set of machine parameters and scenario optimizations.

The increased plasma current is a key capability of the upgrade. Hence, the parameters of 100% non-inductive scenarios in NSTX-Upgrade and existing NSTX data are plotted against $I_P$ in Fig. 29; these data are a subset of that in Table #1. The stored energy in NSTX is at most ~460 kJ [Gerhardt 2011]. The projected stored energies for fully non-inductive scenarios in NSTX-U range from 630-1100 kJ for the $B_T$=1 T cases with six sources at 100 kV each, to 260-400 kJ for $B_T$ =0.75 T with four sources at 80 kV. The highest non-inductive fractions yet achieved in NSTX are 65-70% [Menard 2006, Gates 2009, Gerhardt 2010, Gerhardt 2011], in 700-750 kA discharges. NSTX-Upgrade is projected to achieve non inductive currents in the range of 1000-1400 kA for $B_T$=1.0T and six 100 kV neutral beam sources, down to 675-865 kA for $B_T$=0.75T and six 80 kV neutral beam sources

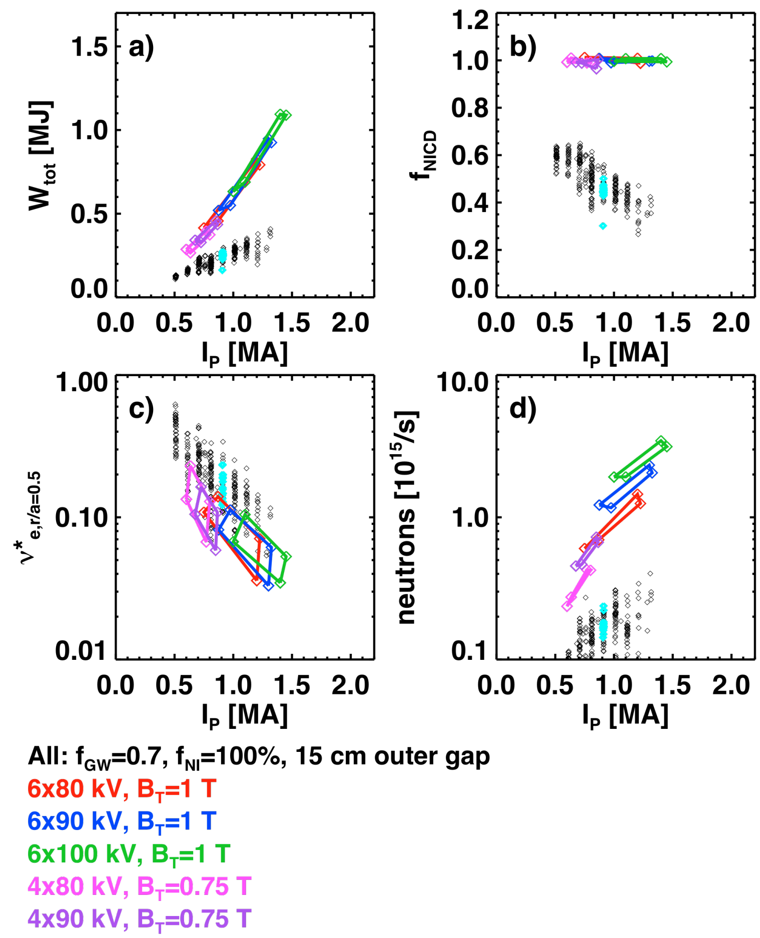


*Fig 29: Comparison between 100 % non-inductive scenarios for NSTX-Upgrade and achieved NSTX scenarios, as a function of plasma current. The a) stored energy, b) non-inductive current fraction, c) mid-radius collisionality, and d) neutron emission rate, as a function of the plasma current.*

The midradius collisionality and total neutron emission are shown in frames 29c) and 29d). We see that the collisionality of these fully non-inductive upgrade scenarios is comparable to the lowest ever achieved in NSTX. The neutron emission rate is up to a factor of 10 larger than the maximum value in the database of high-performance NSTX discharges.

Some stability related metrics for these 100% non-inductive scenarios are shown in Fig. 30. The most significant change related to global stability for NSTX-Upgrade is the increase in aspect ratio. As shown in frame 30a), the values of $\beta_N$ anticipated for these scenarios are not larger than has been achieved in many discharges in NSTX at lower aspect ratio. The larger aspect ratio points in cyan show $\beta_N$ ~4-4.5 without passing disruptive $\beta$ limits [Gerhardt 2011a], and no effort was made in that experiment to determine the maximum experimentally achievable $\beta_N$ at this higher aspect ratio. The toroidal $\beta$ values for these scenarios are less than previously achieved in NSTX, due to the comparatively large vales of $q_{95}$.

The increased aspect ratio of the Upgrade also results in a reduction of the "natural elongation" [Peng 1986, Riccardo 1992, Menard 1997] of the configuration. Natural elongation refers to the elongation that the plasma cross-section would achieve in a perfectly straight vertical field, and as the natural elongation is reduced, the n=0 passive stability margin is likely reduced as well. Fig 30c) shows, however, that the 100% non-inductive scenarios presented here are at lower elongation, and only somewhat higher aspect ratio, than have already been achieved in NSTX. Hence, we conclude that n=0 stability is unlikely to be a significant limiting factor in these scenarios.

Finally, the so-called volume-average $\beta_N$ for NSTX data and NSTX-U scenarios is plotted against the cylindrical safety factor q* in Fig. 30d). As described in section 6.4, q* has been previously identified as a good aspect ratio independent measure of the current limit [Menard 2004], with the no-wall $\beta_N$ limit dropping precipitously for q*< 1.8. Further, the volume average $\beta_N$, denoted $\langle\beta_N\rangle$, is defined as $\langle\beta_N\rangle = \langle\beta_T\rangle I_P a / B_{T0}$, with $\langle\beta_T\rangle = \langle p\rangle 2\mu_0 / \langle B^2\rangle$. Ref. [Menard 2004] shows that $\langle\beta_N\rangle$ is a good aspect-ratio independent indicator of the no-wall stability limit. The data in frame 26d) shows that these 100% non-inductive scenarios optimize to rather high q*, significantly above most of the NSTX data in the database and well away from the low-q limit. The values of $\langle\beta_N\rangle$ are comparable to, or, in the case with six 100 kV beams injecting 15.6 MW, only slightly higher than has been achieved in many occasions in NSTX.

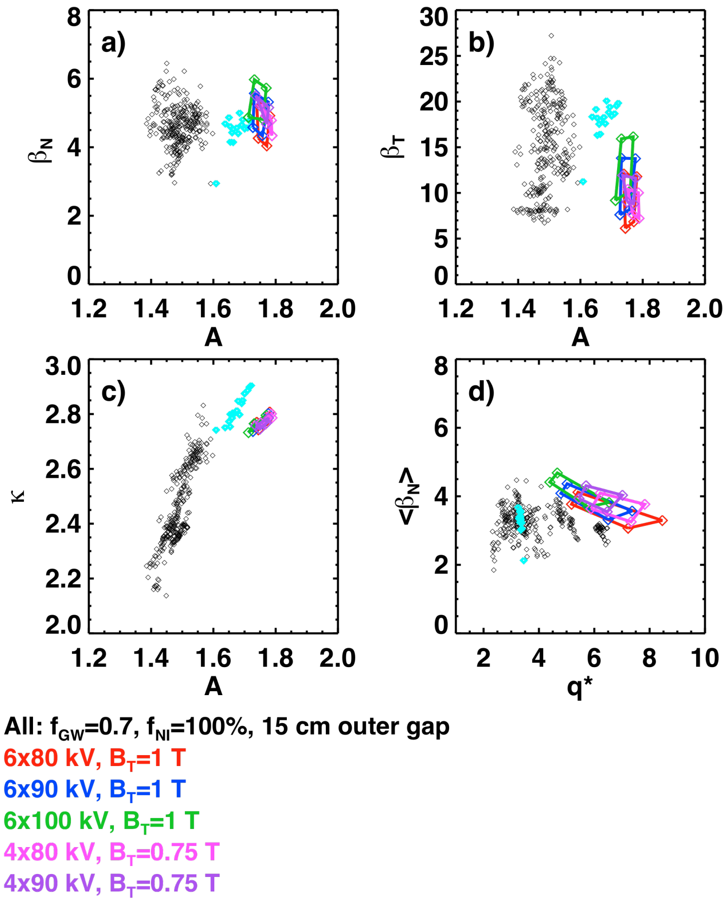


*Fig. 30: Comparison of stability-related parameters between 100 % non-inductive scenarios for NSTX-Upgrade to achieved NSTX scenarios.*

We next consider the high-current partial-inductive scenarios at $f_{GW}$=0.7, and $B_T$=1.0, 0.75, and 0.55. As described in Sections 6.2 and 6.4, these scenarios were designed to find the highest current possible for each toroidal field, heating scheme, Greenwald fraction, and confinement and profile assumption, consistent with $q_{min}$>1.1. The 0.55 T cases in Sect. 6.4 were also run with a large outer gap of 20 cm, in order to maximize the elongation and off-axis current drive.

Fig. 31 shows the parameters of these partial inductive cases as a function of plasma current. The stored energy of these scenarios is vastly higher than the present NSTX cases, exceeding 1.4 MJ for the most favorable cases with six 100 kV beams ($P_{inj}$=15.6 MW) at $I_P$= 1.975 MA and $B_T$=1 T. Interestingly, these Upgrade scenarios have substantially higher non-inductive fractions than the NSTX cases at the same plasma current, due to the increase in both the beam current drive and the toroidal field. The collisionality is shown on a log scale in frame 27c, and generally decreases along the trend of the existing NSTX data. Note that the higher Greenwald fractions in these scenarios, desired for keeping $q_{min}$ elevated, tend to increase the collisionality, and a scenario with very low collisionality will be discussed below. Finally, the neutron emission is 10-15 times larger than in the present NSTX scenarios.

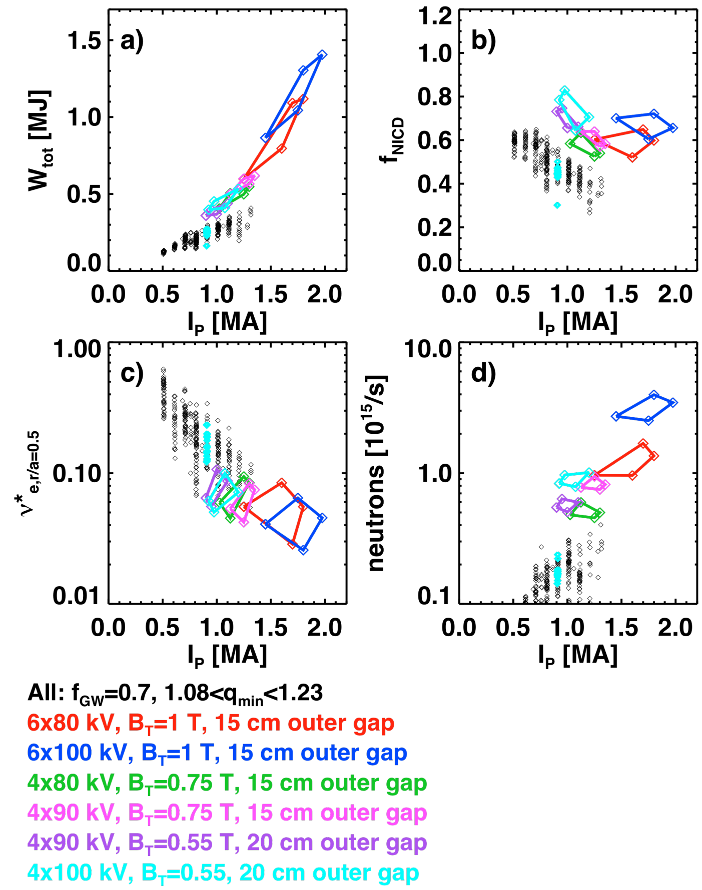


*Fig. 31: Comparison between partial -inductive scenarios at $f_{GW}$=0.7 for NSTX-Upgrade and achieved NSTX scenarios, as a function of plasma current. The quantities plotted are the same as in Fig. 29.*

The global stability metrics of these $f_{GW}$=0.7 partial inductive scenarios are shown in Fig. 32. Fig 32a) shows that the $B_T$=1 & 0.75 T scenarios generally have $\beta_N$ values comparable to those already achieved, while the 0.55 T case pushes to higher values. This contrast is made more clear in frame 28d) where the values of $<\beta_N>$ for the $B_T$=0.55 T, 100 kV cases are significantly in excess of previous achievements. The value of $\beta_T$ in Fig. 32c) are comparable to that achieved in NSTX. However, all the highest $\beta_T$ experimental points in that figure have $q_{min}$ evolving to less than unity, while the NSTX-Upgrade scenarios maintain $q_{min}$>1.1. The values of aspect ratio and elongation in Fig. 32 are not an extension beyond that already achieved, except for the $B_T$=0.55 scenarios at higher elongation of 2.8-3.0. It is clear that these scenarios will provide a severe test of n=0 and n=1 control.

Finally, the performance parameters for a number of additional partial inductive scenarios are considered as a function of the plasma current in Fig. 33. The first two cases are the $f_{GW}$=1.0, $E_{inj}$=80 kV scenarios at $B_T$=1.0 and 0.75 T, discussed in Sect 6.2. These are designed to achieve the longest possible pulses with 80 kV beams for high values of plasma current. For $B_T$=1.0, the device goal of 2 MA can be sustained with $q_{min}$>1 for 5 seconds with six 80 kV beams, provided that the confinement and profiles are sufficiently favorable. These scenarios have stored energies of ~1 MJ with 50-60% of the current generated non-inductively, but with comparatively high collisionality. For $B_T$=0.75 T, current levels of up to 1.425 MA can be sustained with four 80 kV beams for the 5-second pulse duration

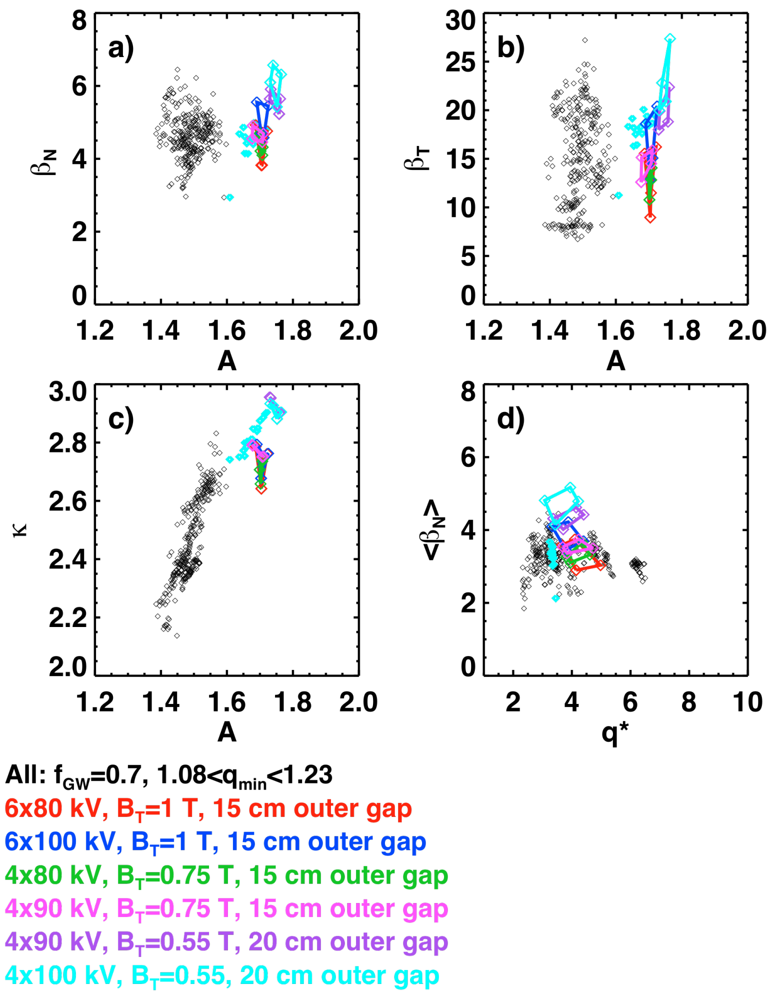


*Fig 32: Global stability metrics for the $f_{GW}$=0.7 partial inductive scenarios.*

We also show in this figure parameters for the very long-pulse configurations described in Sect. 6.3, designed to operate with pulse lengths of 8-10 seconds. Both the scenarios with six 65 kV beams or staggered triplets of 80 kV beams have stored energies comparable to or larger than the best previously achieved in NSTX, with non-inductive fractions significantly larger than in NSTX for the given values of the plasma current. The collisionality tends to be on the low end of that already achieved in NSTX, with neutron emission rates comparable to the largest typically achieved.

Finally, a key programmatic goal of NSTX-U is to achieve reduced collisionality for electron transport and MHD stability studies. It is clear that the achievement of low collisionality is facilitated by reducing the plasma density, increasing the neutral beam power, and operating at high field and current. We show here the parameters for an $I_P$=2MA, $B_T$=1 T, $f_{GW}$=0.55 scenario heated by six 100 kV beams. With the higher current and stronger central current drive, the central safety factor evolves to be less than 1. The mid-radius collisionality, however, is considerably reduced compared to either the present NSTX data or other NSTX-U scenarios, and thus provide a discharge target for the necessary studies at very low collisionality. These scenarios also have the highest neutron emission of any studies here. Note that the current penetration time is in the range $\tau_{CR}$=0.9-1.1 seconds for these scenarios, compared to heating pulse durations of 1.5 seconds. Hence, it should be possible to complete the necessary physics studies and terminate the discharge before $q_{min}$ crosses 1.

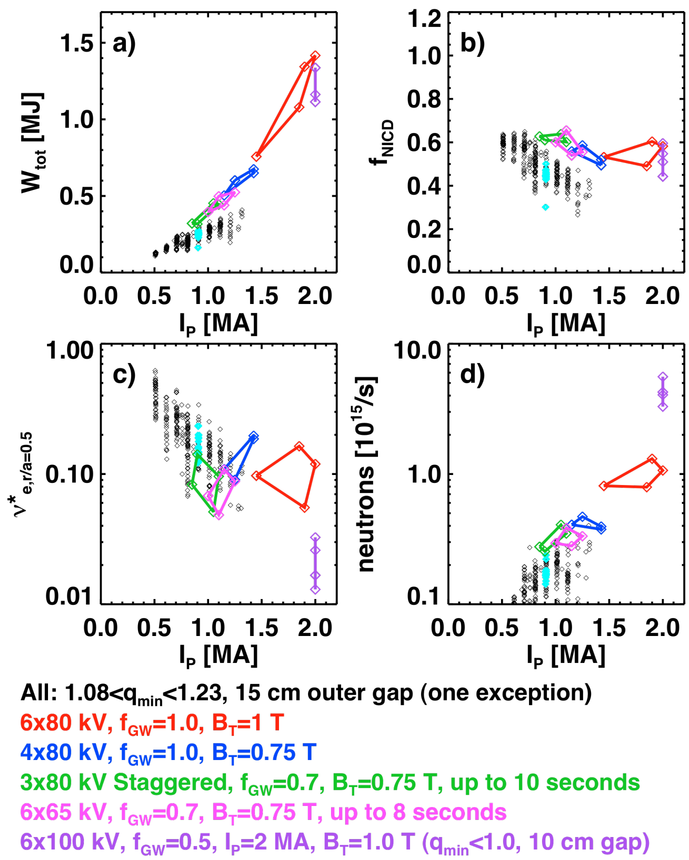


*Fig 33: Comparison between various partial-inductive scenarios for NSTX-Upgrade and achieved NSTX scenarios, as a function of plasma current. The quantities plotted are the same as in Fig. 29. See text for additional details.*

## 8: Summary and Discussion

This paper has documented many of the key elements in developing scenarios for NSTX-Upgrade. Key among them include:

- We generally find a comparatively large outer gap to be advantageous for the scenario; a value of 15 cm appears optimal in most circumstances for elevating

$q_{min}$ without producing unacceptable shine-though loss of the largest tangency-radius beam.

- The plasma density plays a key role in determining the central safety factor. For the scenarios discussed here, Greenwald fractions less that 0.65-0.75 generally result in $q_{min}$<1.
- Modest levels of anomalous fast ion diffusivity ($D_{FI}$<1 $m^2$/s) would not pose a significant problem for the scenarios discussed here. In cases where there is significant on-axis NBCD, small anomalous diffusivities values help to reduce this central current drive, raise $q_{min}$, and decrease the pressure peaking. This in turn assists the stability properties, though at the expense of somewhat reduced total beam current drive and non-inductive fraction.
- Under the assumption of fixed global confinement scaling and input power, increasing the ion thermal transport is beneficial for the scenario. This is because the electron temperature must be increased to maintain the fixed stored energy.

In addition, this paper has documented a large number of equilibrated plasma scenarios that can assist in physics explorations relevant to next-step STs. These include the following.

- There are a large number of scenarios with 100% of the plasma current driven non-inductively. For $B_T$=1.0T, we have identified such scenarios with currents ranging from 750 kA to 1450 kA, depending on the beam voltage, profile shapes, and confinement assumptions. For $B_T$=0.75 T scenarios, the equivalent range is 635 kA to 850 kA. These scenarios should allow the study of transport and stability with fully equilibrated 100% non-inductive current drive. See section 6.1 and Table 2.
- High-current partial inductive scenarios with $q_{min}$>1.1 were studied, in order to examine long-pulse high-current capabilities of the device. For $f_{GW}$=0.7 and $B_T$=1.0 T, configurations with currents in the range 1300<$I_P$<1800 kA can be sustained for 5 seconds, while 1500<$I_P$<2000 can be sustained for 1.5 seconds. As before, the ranges on the plasma current are due to the various assumptions regarding the profile shapes and global confinement. These scenarios will allow the study of stability, transport, divertor, and SOL physics and higher current and significantly reduced collisionality. See section 6.2 and Table 3.
- Scenarios exist with the potential for 8-10 second pulse duration, albeit at reduced plasma currents of 850-1250 kA. These scenarios use either six neutral beams with 60 kV acceleration voltage, or 80 kV beams modulated so that only three sources are on at any time. These scenarios should allow studies of particle transport and disruption avoidance for long pulse. See section 6.3 and Table 4.
- By further increasing the elongation compared to those in the previous cases, very high $\beta_T$ scenarios with $q_{min}$>1.1 can be achieved. Typical values are 18%<$\beta_T$ <20% with $I_P$=900-1200 at $B_T$=0.55 T. These scenarios will allow the study of MHD control at with strong shaping and high $\beta_N$. See section 6.4 and Table 5.
- The safety factor can be modified by varying the beam mix at fixed shape, density, and heating power. For instance, at $B_T$=1.0T, $q_{min}$ can be changed between 1.1 and 2.5 with $P_{inj}$=8.4 MW and $I_P$=800 kA by choosing various

combinations of four neutral beam sources. These scenarios will allow studies of the optimal current profile for MHD stability and transport, as will as provide a basis for q-profile control using the neutral beam as an actuator. See section 6.5 and Table 6.

When considered as a complete set, the large database of equilibria and stability calculations allows an assessment of the "typical" ideal MHD n=1 no-wall and with-wall $\beta_N$ limits for NSTX-Upgrade scenarios. An example of this calculation is shown in Fig. 34, where $\beta_N$ is plotted against the pressure peaking factor. Red points are indicative of unstable configurations, while green points indicate stability. These points come from a variety of scenarios, for instance, with $0.35<f_{NI}<1.2$ and $1.1<q_{min}<3.7$.

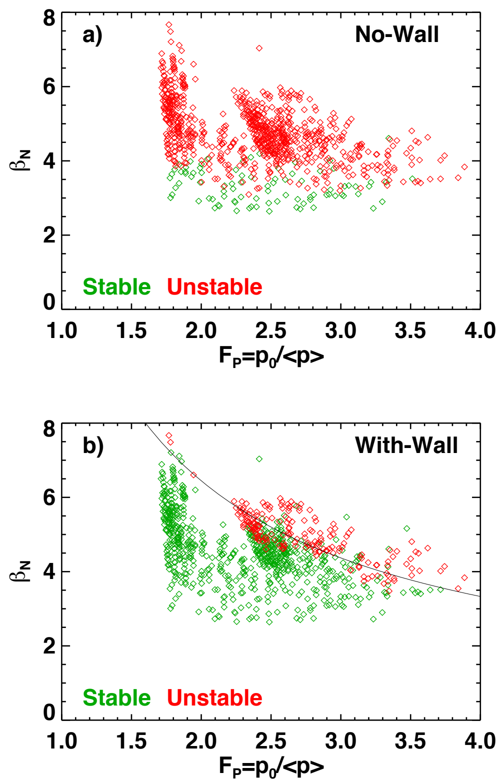


*Fig. 34: Plots of the normalized-β vs. pressure peaking factor. The colors are indicative of the n=1 ideal stability, without a wall in a) and with an ideally conducting wall at the location of the passive plates in b).*

Frame a) shows the results without any conducting walls in the vicinity of the plasma. The $\beta_N$ limit in this case is generally in the vicinity of 3.5, which is a substantial reduction compared to the more typical NSTX values of 4.0-4.5 [Menard 2006, Gerhardt 2011b] due to the increase in the aspect ratio [Menard 2003, Gerhardt 2011b]. More importantly, the vast majority of points fall in the unstable regime. Frame 34b) shows the same data, but with a conducting wall included in the stability analysis. The majority of points in these cases are now stable. There is also a clear dependence of the stability boundary on the pressure peaking, in this case parameterized as $0.2+12.5/F_P$. Stable configurations with $\beta_N$=7 have been found when the pressure peaking is sufficiently low. These two frames make it clear that RWM stability, either passively [Berkery 2010a, Berkery 2010b, Berkery 2011a, Berkery 2011b, Reimerdes 2011] or via feedback [Sabbagh 2006a, Menard 2010a, Sabbagh 2010] will be critical for high-performance operation.

As is clear from the discussion in Sects. 3 & 5, there are a number of ways that this modeling could be improved. The obvious potential improvement is to use a validated model for the electron thermal transport. This could result in substantial modifications to some results in this paper. For instance, the cases with reversed shear could lead to the formation of internal transport barriers. A validated electron transport model could also provide more reasonable expectations about the equilibrium trends with $Z_{eff}$. Work is presently underway to compare non-linear transport estimates from micro-turbulence to experimental fluxes [Guttenfelder 2011]. However, considerable work is required before a validated reduced transport model is available for scenario modeling purposes.

The stability modeling described in this paper is also insufficient to guarantee globally stable scenarios. Given that virtually all scenarios have $\beta_N$ greater than the no-wall limit, resistive wall mode stability is a factor. Calculation of RWM stability is an area of active research, and has not been attempted for these scenarios. Those calculations would require knowledge of the fast particle population (which is included in the context of the TRANSP runs), but also a prediction of the rotation profile. This in turn emphasizes the needs for proper reduced transport models. We also note that while this paper has focused on scenarios with $q_{min}$>1.1 for the avoidance of non-resonant core kinks, the actual required increment of $q_{min}$ above 1 will likely increase with aspect ratio [Chapman 2010], and depend on quantities like the rotation shear, magnetic shear, and possibly the energetic particle population.

This work has treated non-classical fast ion transport in a simplified way, with spatially and temporally constant fast ion diffusivity. As noted in Sect. 5, large TAE avalanches are documented to have a major effect on the current profile [Gerhardt 2011a], severely reducing the central NB current drive. Furthermore, these modes my modify the spectrum of low-frequency disruption MHD [Gude 1999, Gerhardt 2009, Okabayashi 2011, Berkery…Berkery, Reimerdes 2011] The onset conditions for these modes has  not been documented in a way that allows their existence in these scenarios to be predicted. However, the scenarios discussed here generally have small values of fast-ion $\beta$ and large values of the plasma density, which should make these modes more stable.

We finally note that these calculations have generally assumed that the divertor will tolerate the power fluxes for pulses of the given duration, without deleteriously impacting the core performance. Accomplishing these divertor solutions, and studying their compatibility with the high-performance plasma core, will be a major part of the research program. Candidate solutions under consideration include partial detachment [Soukhanovskii 2009a, Soukhanovskii 2009b] or snowflake divertors [Soukhanovskii 2011, Menard 2012].

## 9: Acknowledgments

The authors would like to thank the TRANSP team for their assistance in these simulations. They would also like to thank S. Kaye and W. Guttenfelder for helpful discussion. This research was funded by the United States Department of Energy.

Appendix

The tables in this paper utilize data from given runs of the TRANSP code. Each run of the code is indicated by the shot number and a "run-ID" given by a letter and two number, for instance 'A12' or 'Z52'. The TRANSP runs, and the times during each run run, are indicated in the tables below.

| Shot | ID | $t_{min}$ | $t_{max}$ | $I_p$ [kA] | $B_T$ [T] | $P_{inj}$ [MW] | $f_{GW}$ | $H_{98}$ | $H_{ST}$ | $q_{min}$ | $f_{NICD}$ | A | $\kappa$ |
|---|---|---|---|---|---|---|---|---|---|---|---|---|---|
| 142301 | H56 | 11.8 | 11.95 | 870 | 0.99 | 10.20 | 0.72 | 1.03 | 0.70 | 1.60 | 1.01 | 1.77 | 2.78 |
| 142301 | E77 | 11.8 | 11.95 | 1225 | 0.99 | 10.20 | 0.70 | 1.31 | 0.99 | 2.37 | 0.99 | 1.78 | 2.81 |
| 121123 | K34 | 11.8 | 11.95 | 750 | 1.00 | 10.20 | 0.72 | 1.00 | 0.63 | 1.41 | 1.01 | 1.74 | 2.74 |
| 121123 | N22 | 11.8 | 11.95 | 1200 | 1.00 | 10.20 | 0.70 | 1.40 | 1.02 | 2.48 | 1.01 | 1.74 | 2.77 |
| 142301 | B85 | 11.8 | 11.95 | 975 | 0.99 | 12.60 | 0.72 | 1.00 | 0.70 | 1.50 | 0.99 | 1.76 | 2.76 |
| 142301 | E72 | 11.8 | 11.95 | 1325 | 0.99 | 12.60 | 0.70 | 1.27 | 1.00 | 2.03 | 1.00 | 1.78 | 2.80 |
| 121123 | R42 | 11.8 | 11.95 | 875 | 1.00 | 12.60 | 0.73 | 1.01 | 0.66 | 1.39 | 1.01 | 1.73 | 2.74 |
| 121123 | Q62 | 11.8 | 11.95 | 1300 | 1.00 | 12.60 | 0.71 | 1.34 | 1.00 | 2.10 | 1.00 | 1.73 | 2.76 |
| 142301 | D46 | 15.8 | 15.95 | 1100 | 0.99 | 15.60 | 0.77 | 1.01 | 0.74 | 1.52 | 1.01 | 1.76 | 2.77 |
| 142301 | Y93 | 11.8 | 11.95 | 1450 | 1.00 | 15.60 | 0.71 | 1.24 | 1.00 | 1.76 | 0.99 | 1.77 | 2.80 |
| 121123 | J26 | 11.8 | 11.95 | 1000 | 1.00 | 15.60 | 0.74 | 0.98 | 0.67 | 1.31 | 1.00 | 1.71 | 2.73 |
| 121123 | K96 | 11.8 | 11.95 | 1400 | 1.01 | 15.60 | 0.71 | 1.30 | 1.00 | 1.82 | 1.01 | 1.73 | 2.76 |
| 142301 | V91 | 11.8 | 11.95 | 635 | 0.74 | 6.80 | 0.72 | 1.00 | 0.80 | 0.98 | 1.01 | 1.79 | 2.79 |
| 142301 | U76 | 11.8 | 11.95 | 800 | 0.74 | 6.80 | 0.71 | 1.17 | 1.00 | 1.53 | 0.99 | 1.79 | 2.80 |
| 121123 | Q03 | 11.8 | 11.95 | 600 | 0.74 | 6.80 | 0.71 | 1.00 | 0.77 | 0.81 | 0.99 | 1.77 | 2.76 |
| 121123 | Q52 | 11.8 | 11.95 | 770 | 0.75 | 6.80 | 0.70 | 1.22 | 0.99 | 1.72 | 0.99 | 1.75 | 2.77 |
| 142301 | E55 | 11.8 | 11.95 | 725 | 0.74 | 8.40 | 0.72 | 0.99 | 0.82 | 1.10 | 0.99 | 1.77 | 2.77 |
| 142301 | B58 | 11.8 | 11.95 | 865 | 0.74 | 8.40 | 0.71 | 1.14 | 1.00 | 1.36 | 1.00 | 1.78 | 2.79 |
| 121123 | B90 | 11.8 | 11.95 | 675 | 0.74 | 8.40 | 0.72 | 1.00 | 0.79 | 0.90 | 0.99 | 1.75 | 2.75 |
| 121123 | Q48 | 11.8 | 11.95 | 850 | 0.75 | 8.40 | 0.72 | 1.18 | 0.99 | 1.60 | 0.96 | 1.74 | 2.76 |

Table A1: TRANSP runs and basic parameters corresponding to the data in table #2

| Shot | ID | $t_{min}$ | $t_{max}$ | $I_p$ [kA] | $B_T$ [T] | $P_{inj}$ [MW] | $f_{GW}$ | $H_{98}$ | $H_{ST}$ | $q_{min}$ | $f_{NICD}$ | A | $\kappa$ |
|---|---|---|---|---|---|---|---|---|---|---|---|---|---|
| 142301 | E34 | 11.8 | 11.95 | 1600.4 | 1.01 | 10.20 | 0.74 | 1.00 | 0.78 | 1.14 | 0.52 | 1.71 | 2.74 |
| 142301 | H47 | 11.8 | 11.95 | 1800 | 1.01 | 10.20 | 0.73 | 1.22 | 1.00 | 1.16 | 0.60 | 1.72 | 2.76 |
| 121123 | B12 | 11.8 | 11.95 | 1250 | 1.01 | 10.20 | 0.73 | 1.00 | 0.68 | 1.19 | 0.60 | 1.70 | 2.64 |
| 121123 | K70 | 11.8 | 11.95 | 1700.2 | 1.01 | 10.20 | 0.74 | 1.28 | 1.00 | 1.10 | 0.65 | 1.69 | 2.79 |
| 142301 | J82 | 11.8 | 11.95 | 1700 | 1.01 | 12.60 | 0.74 | 1.01 | 0.81 | 1.09 | 0.56 | 1.71 | 2.73 |
| 142301 | J92 | 11.8 | 11.95 | 1900 | 1.01 | 12.60 | 0.73 | 1.19 | 1.01 | 1.10 | 0.62 | 1.72 | 2.76 |
| 121123 | N93 | 11.8 | 11.95 | 1350 | 1.01 | 12.60 | 0.73 | 1.01 | 0.72 | 1.17 | 0.65 | 1.70 | 2.66 |
| 121123 | N39 | 11.8 | 11.95 | 1750.3 | 1.01 | 12.60 | 0.74 | 1.24 | 0.99 | 1.12 | 0.68 | 1.69 | 2.79 |
| 142301 | J86 | 11.8 | 11.95 | 1750 | 1.01 | 15.60 | 0.74 | 0.99 | 0.81 | 1.11 | 0.60 | 1.71 | 2.75 |
| 142301 | M16 | 11.8 | 11.95 | 1975 | 1.01 | 15.60 | 0.73 | 1.16 | 1.00 | 1.12 | 0.66 | 1.73 | 2.76 |
| 121123 | J93 | 11.8 | 11.95 | 1450 | 1.01 | 15.60 | 0.73 | 1.01 | 0.75 | 1.16 | 0.70 | 1.70 | 2.68 |
| 121123 | K55 | 11.8 | 11.95 | 1800 | 1.01 | 15.60 | 0.74 | 1.20 | 0.98 | 1.13 | 0.72 | 1.69 | 2.79 |
| 142301 | W93 | 11.8 | 11.95 | 1250 | 0.76 | 6.80 | 0.74 | 1.00 | 0.92 | 1.12 | 0.53 | 1.71 | 2.74 |
| 142301 | W88 | 11.8 | 11.95 | 1300 | 0.76 | 6.80 | 0.74 | 1.05 | 0.98 | 1.10 | 0.54 | 1.71 | 2.74 |
| 121123 | D06 | 11.8 | 11.95 | 1025 | 0.76 | 6.80 | 0.73 | 1.01 | 0.83 | 1.10 | 0.58 | 1.70 | 2.66 |
| 121123 | R32 | 11.8 | 11.95 | 1125 | 0.76 | 6.80 | 0.73 | 1.14 | 0.98 | 1.15 | 0.63 | 1.70 | 2.71 |
| 142301 | W84 | 11.8 | 11.95 | 1300 | 0.76 | 8.40 | 0.74 | 1.00 | 0.94 | 1.14 | 0.57 | 1.71 | 2.75 |
| 142301 | C15 | 11.8 | 11.95 | 1350 | 0.76 | 8.40 | 0.74 | 1.05 | 1.01 | 1.11 | 0.58 | 1.71 | 2.75 |
| 121123 | Q42 | 11.8 | 11.95 | 1125 | 0.76 | 8.40 | 0.75 | 1.01 | 0.89 | 1.19 | 0.64 | 1.68 | 2.79 |
| 121123 | B96 | 11.8 | 11.95 | 1250 | 0.76 | 8.40 | 0.75 | 1.09 | 1.00 | 1.08 | 0.64 | 1.68 | 2.79 |
| 142301 | E59 | 3.8 | 3.95 | 1850 | 1.01 | 10.20 | 1.05 | 1.00 | 0.81 | 1.12 | 0.49 | 1.72 | 2.74 |
| 142301 | O46 | 3.8 | 3.95 | 2000 | 1.00 | 10.20 | 1.03 | 1.19 | 1.01 | 1.24 | 0.58 | 1.73 | 2.77 |
| 121123 | Q16 | 3.8 | 3.95 | 1450 | 1.01 | 10.20 | 1.03 | 0.99 | 0.70 | 1.14 | 0.53 | 1.71 | 2.64 |
| 121123 | C93 | 3.8 | 3.95 | 1900 | 1.01 | 10.20 | 1.04 | 1.24 | 0.99 | 1.06 | 0.60 | 1.70 | 2.74 |
| 142301 | E81 | 3.8 | 3.95 | 1425 | 0.76 | 6.80 | 1.05 | 0.99 | 0.95 | 1.13 | 0.49 | 1.72 | 2.75 |
| 142301 | E83 | 3.8 | 3.95 | 1425 | 0.76 | 6.80 | 1.05 | 1.03 | 1.00 | 1.18 | 0.52 | 1.72 | 2.76 |
| 121123 | Q39 | 3.8 | 3.95 | 1150 | 0.76 | 6.80 | 1.04 | 1.03 | 0.88 | 1.17 | 0.56 | 1.70 | 2.70 |
| 121123 | Q29 | 3.8 | 3.95 | 1250 | 0.76 | 6.80 | 1.04 | 1.11 | 0.99 | 1.15 | 0.59 | 1.70 | 2.72 |

Table A2: TRANSP runs and basic parameters corresponding to the data in table #3

| Shot | ID | $t_{min}$ | $t_{max}$ | $I_p$ [kA] | $B_T$ [T] | $P_{inj}$ [MW] | $f_{GW}$ | $H_{98}$ | $H_{ST}$ | $q_{min}$ | $f_{NICD}$ | A | $\kappa$ |
|---|---|---|---|---|---|---|---|---|---|---|---|---|---|
| 142301 | W29 | 11.8 | 11.95 | 1150 | 0.76 | 6.60 | 0.74 | 0.99 | 0.89 | 1.25 | 0.54 | 1.71 | 2.75 |
| 142301 | V21 | 11.8 | 11.95 | 1250 | 0.76 | 6.60 | 0.74 | 1.07 | 0.99 | 1.16 | 0.56 | 1.71 | 2.75 |
| 121123 | K51 | 11.8 | 11.95 | 1000 | 0.76 | 6.60 | 0.75 | 0.99 | 0.83 | 1.24 | 0.60 | 1.68 | 2.79 |
| 121123 | J38 | 11.8 | 11.95 | 1100 | 0.76 | 6.60 | 0.74 | 1.15 | 1.00 | 1.27 | 0.66 | 1.69 | 2.80 |
| 142301 | L89 | 13.8 | 14.8 | 900 | 0.75 | 5.10 | 0.74 | 1.00 | 0.83 | 1.58 | 0.61 | 1.72 | 2.75 |
| 142301 | L94 | 13.8 | 14.8 | 1100 | 0.75 | 5.10 | 0.73 | 1.14 | 1.01 | 1.37 | 0.60 | 1.72 | 2.76 |
| 121123 | N80 | 13.8 | 14.8 | 850 | 0.76 | 5.10 | 0.75 | 1.01 | 0.80 | 1.39 | 0.63 | 1.69 | 2.79 |
| 121123 | N75 | 13.8 | 14.8 | 1050 | 0.76 | 5.10 | 0.74 | 1.19 | 1.01 | 1.23 | 0.64 | 1.69 | 2.79 |

Table A3: TRANSP runs and basic parameters corresponding to the data in table #4

| Shot | ID | $t_{min}$ | $t_{max}$ | $I_p$ [kA] | $B_T$ [T] | $P_{inj}$ [MW] | $f_{GW}$ | $H_{98}$ | $H_{ST}$ | $q_{min}$ | $f_{NICD}$ | A | $\kappa$ |
|---|---|---|---|---|---|---|---|---|---|---|---|---|---|
| 142301 | S94 | 11.8 | 11.95 | 1100 | 0.55 | 8.40 | 0.74 | 0.98 | 1.15 | 1.15 | 0.66 | 1.76 | 2.90 |
| 142301 | S39 | 11.8 | 11.95 | 1000 | 0.55 | 8.40 | 0.74 | 0.91 | 1.03 | 1.24 | 0.66 | 1.76 | 2.90 |
| 121123 | Q65 | 11.8 | 11.95 | 950 | 0.56 | 8.40 | 0.74 | 1.00 | 1.09 | 1.20 | 0.75 | 1.73 | 2.95 |
| 121123 | K15 | 11.8 | 11.95 | 900 | 0.56 | 8.40 | 0.75 | 0.94 | 1.01 | 1.21 | 0.73 | 1.73 | 2.96 |
| 142301 | R77 | 11.8 | 11.95 | 1200 | 0.55 | 10.40 | 0.74 | 0.99 | 1.21 | 1.09 | 0.71 | 1.76 | 2.90 |
| 142301 | M08 | 11.8 | 11.95 | 1075 | 0.56 | 10.40 | 0.74 | 0.85 | 0.99 | 1.08 | 0.64 | 1.75 | 2.88 |
| 121123 | Q72 | 11.8 | 11.95 | 975 | 0.56 | 10.40 | 0.74 | 1.01 | 1.13 | 1.11 | 0.83 | 1.74 | 2.93 |
| 121123 | Q83 | 11.8 | 11.95 | 925 | 0.56 | 10.40 | 0.75 | 0.92 | 1.01 | 1.10 | 0.78 | 1.73 | 2.93 |

Table A4: TRANSP runs and basic parameters corresponding to the data in table #5

| Shot | ID | $t_{min}$ | $t_{max}$ | $I_p$ [kA] | $B_T$ [T] | $P_{inj}$ [MW] | $f_{GW}$ | $H_{98}$ | $H_{ST}$ | $q_{min}$ | $f_{NICD}$ | A | $\kappa$ |
|---|---|---|---|---|---|---|---|---|---|---|---|---|---|
| 142301 | F83 | 15.8 | 15.95 | 675 | 0.98 | 8.40 | 0.71 | 0.98 | 0.61 | 1.88 | 1.00 | 1.79 | 2.80 |
| 142301 | K79 | 11.8 | 11.95 | 740 | 0.99 | 8.40 | 0.72 | 1.00 | 0.64 | 1.55 | 1.02 | 1.78 | 2.78 |
| 142301 | K82 | 11.8 | 11.95 | 770 | 0.98 | 8.40 | 0.73 | 1.01 | 0.65 | 1.00 | 1.02 | 1.77 | 2.76 |
| 142301 | F66 | 15.8 | 15.95 | 800 | 0.99 | 8.40 | 0.73 | 0.99 | 0.64 | 1.51 | 1.00 | 1.76 | 2.76 |
| 142301 | U84 | 11.8 | 11.95 | 800 | 0.99 | 8.40 | 0.71 | 1.00 | 0.65 | 2.47 | 0.87 | 1.77 | 2.78 |
| 142301 | U85 | 11.8 | 11.95 | 800 | 0.99 | 8.40 | 0.72 | 0.99 | 0.64 | 2.11 | 0.92 | 1.76 | 2.77 |
| 142301 | F62 | 15.8 | 15.95 | 800 | 0.99 | 8.40 | 0.73 | 1.01 | 0.66 | 1.11 | 0.98 | 1.77 | 2.76 |
| 142301 | F66 | 15.8 | 15.95 | 800 | 0.99 | 8.40 | 0.73 | 0.99 | 0.64 | 1.51 | 1.00 | 1.76 | 2.76 |
| 142301 | Q91 | 11.8 | 11.95 | 650 | 0.74 | 8.40 | 0.71 | 0.99 | 0.80 | 1.23 | 1.01 | 1.79 | 2.80 |
| 142301 | E55 | 11.8 | 11.95 | 725 | 0.74 | 8.40 | 0.72 | 0.99 | 0.82 | 1.10 | 0.99 | 1.77 | 2.77 |
| 142301 | M21 | 11.8 | 11.95 | 765 | 0.74 | 8.40 | 0.73 | 1.00 | 0.84 | 0.68 | 0.99 | 1.76 | 2.75 |
| 142301 | C50 | 15.8 | 15.95 | 775 | 0.74 | 8.40 | 0.73 | 0.99 | 0.82 | 0.93 | 1.00 | 1.75 | 2.75 |
| 142301 | M32 | 11.8 | 11.95 | 800 | 0.75 | 8.40 | 0.72 | 1.00 | 0.84 | 1.77 | 0.85 | 1.76 | 2.78 |
| 142301 | M42 | 11.8 | 11.95 | 800 | 0.75 | 8.40 | 0.72 | 1.00 | 0.84 | 1.46 | 0.89 | 1.76 | 2.77 |
| 142301 | M26 | 11.8 | 11.95 | 800 | 0.74 | 8.40 | 0.73 | 1.00 | 0.84 | 0.79 | 0.93 | 1.75 | 2.75 |
| 142301 | G89 | 11.8 | 11.95 | 800 | 0.74 | 8.40 | 0.73 | 1.00 | 0.84 | 1.00 | 0.99 | 1.75 | 2.75 |

Table A5: TRANSP runs and basic parameters corresponding to the data in table #6

References

[Abdou 1996] M. Abdou, Fusion Eng. And Design **27**, 111 (1995).

[Akers 2000] R.J. Akers, et al., Nuclear Fusion **40**, 1223 (2000).

[Bell 2010] M. Bell, et al., Plasma Phys. Control. Fusion **51**, 124054 (2009)

[Berkery 2010a] J.W. Berkery et al., Phys. Plasmas **17**, 082504 (2010).

[Berkery 2010b] J.W. Berkery, et al., Phys. Rev. Lett. **104**, 035003 (2010).

[Berkery 2011a] J.W. Berkery, et al, Phys. Plasmas **18**, 072501 (2011).

[Berkery 2011b] J.W. Berkery, et al., Phys. Rev. Lett **106**, 075004 (2011).

[Bickerton 1971] Bickerton R.J., Connor J.W. and Taylor J.B. 1971 Nature Phys. Sci. 229 110.

[Bondeson 1994] A. Bondeson and D.J. Ward, Phys. Rev. Lett. **72**, 2709 (1994).

[Boyle 2011] D.P. Boyle, et al., Plasma Phys. Control. Fusion **53**, 105011 (2011).

[Breslau 2010] J. Breslau, et al., Nuclear Fusion **51**, 063027 (2011).

[Chang 1982] C.S. Chang and F.J. Hinton, Phys. Plasmas **25**, 1493 (1982).

[Chapman 2010] I.T. Chapman, et al., Nuclear Fusion **50**, 045007.

[Diallo 2011] A. Diallo, et al, Nuclear Fusion **51**, 103031 (2011).

[Ferron 2005] J.R. Ferron, et al., Phys. Plasmas **12**, 056126 (2005).

[Ferron 2010] J.R. Ferron, et al., Nuclear Fusion **51**, 063026 (2011).

[Fisch 1987] N.J. Fisch, Rev. Mod. Phys. **59**, 175 (1987).

[Fredrickson 2004] E.D. Fredrickson, et al., Phys. Plasmas **11**, 3563 (2004).

[Fredrickson 2006a] E.D. Fredrickson, et al, Nuclear Fusion **46**, S926 (2006).

[Fredrickson 2006b] E.D. Fredrickson, et al, Phys. Plasmas **13**, 056109 (2006).

[Fredrickson 2009] E. D. Fredrickson, et al., Phys. Plasmas **16**, 122505 (2009).

[Galeev 1971] A. A. Galeev, Sov. Phys. JETP **32**, 752 (1971).

[Gates 2003] D. A. Gates, et al., Nuclear Fusion **10**, 1659 (2003).

[Gates 2004] D.A. Gates, J.E. Menard, and R.J. Marsala, Rev. Sci. Instrum. **75**, 5090 (2004).

[Gates 2006a] D. A. Gates, et al, Phys. Plasmas **13**, 056122 (2006).

[Gates 2006b] D.A. Gates, et al., Nuclear Fusion **46**, S22 (2006)

[Gates 2007] D. A. Gates, et al., Nuclear Fusion **47**, 1376 (2007).

[Gates 2009] D. A. Gates, et al., Nuclear Fusion **49**, 104016 (2009).

[Gerhardt 2009] S.P. Gerhardt, et al, Nuclear Fusion **49**, 032003 (2009).

[Gerhardt 2010] S.P. Gerhardt, et al., Plasma Phys. Control. Fusion **52**, 104003 (2010).

[Gerhardt 2011a] S.P. Gerhardt, et al., Nuclear Fusion **51**, 012001 (2011).

[Gerhardt 2011b] S.P. Gerhardt, et al., Nuclear Fusion **51**, 073031 (2011)

[Gerhardt 2012] S.P. Gerhardt, et al., Fusion Science and Technology

[Glasser 1997] A. H. Glasser and M.C. Chance, 1997 *Bull. Am. Phys. Soc.* **42** 1848.

[Goldston 2008] R.J. Goldston, et al., *An Experiment to Tame the Plasma Material Interface*, IAEA Fusion Energy Conference, Paper FT/P3-12, Geneva (2008).

[Gorelenkov 2004] N.N. Gorelenkov et al., Phys. Plasmas **11**, 2586 (2004).

[Gude 1999] A. Gude, S. Guenter, S. Sesnic, and the ASDEX Upgrade Team, Nuclear Fusion **39**, 127 (1999).

[Greenwald 2002] M. Greenwald, Plasma Phys. Control Fusion **44**, R27 (2002).

[Grey 2010] T. Gray, et al., *Dependences of the divertor and midplane heat flux widths in NSTX,* IAEA Fusion Energy Conference, Paper EXD/P3-13, Chengdu (2008).

[Grisham 1987] L. Grisham et al. Nuclear Instruments and Methods in Physics Research B **24/25**, 741 (1987)

[Grisham 1994] L.R. Grisham for the TFTR group, Plasma Devices and Operations **3**, 187 (1994).

[Grisham 1995] L. Grisham et al. Nuclear Instruments and Methods in Physics Research B **99**, 353 (1995)

[Gryaznevich 1998] M. Gryaznevich, et al., Phys. Rev. Lett. **80**, 3972 (1998)

[Gunter 2007] S. Gunter et al., Nuclear Fusion **47**, 920 (2007).

[Guttenfelder 2011] W. Guttenfelder, et al., Phys. Rev. Lett. **106**, 155004 (2011).

[Hauff 2009] T. Hauff, et al., Phys. Rev. Lett. **102**, 075004 (2009).

[Hawryluk 1980] R. J. Hawryluk, et al., "An Empirical Approach to Tokamak Transport", in Physics of Plasmas Close to Thermonuclear Conditions, ed. by B. Coppi, et al., (CEC, Brussels, 1980), Vol. 1, pp. 19-46.

[Heidbrink 2009a] W.W. Heidbrink, et al., Phys. Rev. Lett. **103**, 175001 (2009).

[Heidbrink 2009b] W.W. Heidbrink, et al, Plasma Phys. Control. Fusion **51**, 125001 (2009)

[Holcomb 2009] C.T. Holcomb, et al., Phys. Plasmas **16**, 056116 (2009)

[Howl 1992] W. Howl, et al., Phys. Fluids B **4**, 1724 (1992)

[ITER 1998] ITER Physics Experts Groups, Nuclear Fusion **39** (1999) 2175.

[Kaye 2006] S.M. Kaye, et al., Nuclear Fusion **46**, 848 (2006).

[Kaye 2007a] S.M. Kaye, et al., Phys. Rev. Lett. **98**, 175002 (2007).

[Kaye 2007b] S.M. Kaye, et al., Nuclear Fusion **47**, 499 (2007).

[Kessel 1994] C.E. Kessel, Nuclear Fusion **34**, 1221 (1994).

[Kinsey 2008] J.E. Kinsey, G. M. Staebler, and R.E. Waltz, Phys. Plasmas **15**, 055908 (2008).

[Kinsey 2011] J.E. Kinsey, et al., Nuclear Fusion **51**, 083001 (2011).

[Kugel 2008] H. Kugel, et al., Phys. Plasmas 15, 056118 (2008)

[Lazarus 1991] E. Lazarus, et al., Phys. Plasmas B **3** 2220, (1991).

[Lazarus 1996] E. Lazarus, et al., Phys. Rev. Lett **77**, 2714 (1996).

[Levinton 2007] F. M. Levinton, et al., Phys. Plasmas **14**, 056119 (2007).

[Lin-Liu 1997] Y.R. Lin-Liu, F.L. Hinton, Phys. Plasmas 4 (1997) 417

[Luce 2011] T.C. Luce, Phys Plasmas **18**, 030501 (2011).

[Lutjens 1996] H. Lutjens, et al., Comp. Phys. Comm. **97**, 219 (1996).

[Maingi 2009] R. Maingi, et al., Phys. Rev. Lett. **103**, 075001 (2009).

[Menard 1997] J. E. Menard, et al., Nuclear Fusion **37**, 595 (1997).

[Menard 2003] J.E. Menard, et al., Nuclear Fusion **43**, 330(2003).

[Menard 2004] J.E. Menard, et al., Phys. Plasmas **11**, 639 (2004).

[Menard 2005] J.E. Menard, et al., Nuclear Fusion **45**, 539 (2005).

[Menard 2006] J.E. Menard, et al., Phys. Rev. Lett **97**, 095002 (2006).

[Menard 2007] J.E. Menard, et al., Nuclear Fusion **47**, S645 (2007).

[Menard 2010a] J.E. Menard, et al., Nuclear Fusion **50**, 045008 (2010).

[Menard 2011] J.E. Menard, et al, Nuclear Fusion **51**, 103014 (2011).

[Menard 2012] J. E. Menard, et al., *Overview of the physics and engineering design of NSTX Upgrade*, submitted to Nuclear Fusion.

[Miller 1997] R.L. Miller, et al., Nuclear Fusion **4**, 1062 (1997).

[Murakami 2005] M. Murakami, et al., Nuclear Fusion **45**, 1419 (2005).

[Najmabadi 2003] F. Najmabadi and the ARIES Team, Fusion Eng. And Design **65**, 143 (2003).

[Ohkawa 1970] T. Ohkawa, Nuclear Fusion **10**, 185 (1970).

[Okabayashi 2011] M. Okabayashi, et al., Phys. Plasmas **18**, 056112 (2011).

[Ono 2000] M. Ono, et al., Nuclear Fusion **40**, 557 (2000).

[Pankin 2004] A. Pankin et al, Comput. Phys. Commun. **159**, 157 (2004).

[Peeters 2000] A.G. Peeters, Plasma Phys. Control. Fusion **42**, B231 (2000).

[Peng 1986] Y.K.M. Peng and D.J. Strickler, Nuclear Fusion **26**, 769 (1986).

[Peng 2005] Y-K M Peng, et al., Plasma Phys. Control. Fusion **47**, B263 (2005).

[Peng 2008] Y-K M Peng, et al., *Effects of Physics Conservatism and Aspect Ratio on Remote Handling for Compact Component Test Facilities (CTFs)*, Paper FT/P3-14, Geneva (2008).

[Peng 2009] Y-K M Peng, et al, Fusion Science and Technology **56**, 957 (2009)

[Podesta 2009] M. Podesta, et al., Phys Plasmas **16**, 056104 (2009).

[Politzer 2005] P.A. Politzer, et al., Nuclear Fusion **45**, 417 (2005).

[Reimerdes 2006] H. Reimerdes, et al., Nuclear Fusion **13**, 056107 (2006).

[Reimerdes 2011] H. Reimerdes, et al., Phys. Rev. Lett. **106**, 21502 (2011).

[Ren 2011] Y. Ren, et al., Phys. Rev. Lett. **106**, 165005 (2011).

[Roberto 1992] M. Roberto, Nuclear Fusion **32**, 1666 (1992).

[Sabbagh 1996] S. A. Sabbagh et al., Proceedings of the 16th International Conference on Fusion Energy, Montreal, CA, 7-11 1996 (1996) AP2-17.

[Sabbagh 2002] S.A. Sabbagh, et al., Phys. Plasmas 9, 2085 (2002).

[Sabbagh 2004] S.A. Sabbagh, et al., Nuclear Fusion 44, 560 (2004)

[Sabbagh 2006a] S.A. Sabbagh, et al., Phys. Rev. Lett. 97, 045004 (2006).

[Sabbagh 2006b] S.A. Sabbagh, et al., Nuclear Fusion **46**, 635 (2006).

[Sabbagh 2010a] S.A Sabbagh, et al., Nuclear Fusion **50** (2010) 025020.

[Sabbagh 2010b] S.A. Sabbagh, et al., *Resistive Wall Mode Stabilization and Plasma Rotation Damping Considerations for Maintaining High Beta Plasma Discharges in NSTX*, Paper EXS/5-5, Daejeon (2010).

[Sauter 1999] O. Sauter, C. Angioni, and Y.R. Lin-Liu, Phys. Plasmas **6**, 2834 (1999).

[Sips 2005] A.C.C Sips, et al., Plasma Phys. Control. Fusion **47**, A19 (2005).

[Smith 2009a] D.R. Smith, et al., Phys. Rev. Lett. **102**, 225005 (2009).

[Smith 2009b] D.R. Smith, et al, Phys. Plasmas **16**, 112507 (2009).

[Snyder 2009] P. Snyder, et al, Phys Plasmas **16**, 056118 (2009).

[Sontag 2005] A.C. Sontag, et al., Phys. Plasmas **12**, 056112 (2005).

[Sontag 2007] A.C. Sontag, et al., Nuclear Fusion **47**, 1005 (2007).

[Sontag 2010] A.C. Sontag, et al, Pedestal Characterization and Stability of Small-ELM Regimes in NSTX, paper EXD/P3-31, IAEA Fusion Energy Conference, Daejeon, Korea (2010).

[Soukhanovskii 2009a] V.A. Soukhanovskii, et al., Phys. Plasmas **16**, 022501 (2009).

[Soukhanovskii 2009b] V.A. Soukhanovskii, et al., Nuclear Fusion **49**, 092025 (2009)

[Soukhanovskii 2011] V.A. Soukhanovskii, et al., Nuclear Fusion **51**, 012001 (2011)

[Stambaugh 1997] R.D. Stambaugh, et al, Fusion Technology **33**, 1 (1998).

[Stambaugh 2010] R.D. Stambaugh, et al., *Candidates for a Fusion Nuclear Science Facility (FDF and ST-CTF),* Paper P2.110, 37th EPS Conference on Plasma Physics, Dublin, Ireland (2010).

[Strait 1994] E.J. Strait, Phys. Plasmas **1**, 1415 (1994).

[Strait 1995] E.J. Strait, et al., Phys. Plasmas **74**, 2483 (1995).

[Stevenson 2002] T. Stevenson, et al., A neutral beam injector upgrade for NSTX, PPPL Report 3651 (2002).

[Stutman 2006] D. Stutman, et al., Phys. Plasmas **13**, 092511 (2006).

[Stutman 2009] D. Stutman, et al., Phys. Rev. Lett. **102**, 115002 (2009).

[Sykes 2001] A. Sykes et al., Nuclear Fusion **41**, 11 (2001).

[Turnbull 1999] A.D. Turnbull, et al., Phys. Plasmas **6**, 1925 (1999).

[Troyon 1984] F. Troyon, et al., Plasma Phys. Control. Fusion **26**, 209 (1984).

[Valovic 2009] M. Valovic, et al., Nuclear Fusion **49**, 075016 (2009).

[Voitsekhovitch 2009] I. Voitsekhovitch, et al., Nuclear Fusion **49**, 055026 (2009).

[Voss 2008] G.M. Voss, et al., Fusion Eng. and Design **83**, 1648 (2008).

[Waltz 1997] R. E. Waltz, G. M. Staebler, W. Dorland, G. W. Hammett, M. Kotschenreuther, and J. A. Konings, Phys. Plasmas **4**, 2482 (3230).

[Wesson] J. Wesson, *Tokamaks*, Clarendon Press, Oxford, England, 1997.

[Wilson 2004a] H.R. Wilson, et al., Nuclear Fusion **44** (2004) 917.

[Wilson 2004b] H.R Wilson, et al., *A Steady State Spherical Tokamak for Components Testing*, IAEA Fusion Energy Conference, Paper FT/3-1Ra, Villamoura, Portugal (2004).

[Wong 2007] K. L. Wong, et al., Phys. Rev. Lett. **99**, 135003 (2007)

[Wong 2008] K. L. Wong, et al., Phys. Plasmas **15**, 056108 (2008)

[Yuh 2009] H. Y. Yuh, et al., Phys. Plasmas **16**, 056120 (2009).

[Zarnstorff 1984] M.C. Zarnstorff and S.C. Prager, Phys. Rev. Lett. **53**, 454 (1984).

[Zarnstorff 1990] M.C. Zarnstorff, et al, Phys. Fluids B **2**, 1852 (1990).

[Zhang 2008] W. Zhang, et al., Phys. Rev. Lett **101**, 095001 (2008).